WORKHOLDING OPTIMIZATION FOR TURNING OF RING SHAPED PARTS

A Thesis

Presented to

The Academic Faculty

by

Martin S. Kurnadi

In Partial Fulfillment

of the Requirements for the Degree

Master of Science in Mechanical Engineering

Georgia Institute of Technology

Atlanta, Georgia

August 2005

WORKHOLDING OPTIMIZATION FOR TURNING OF RING SHAPED PARTS

Approved:

Dr. Shreyes Melkote, Chair
School of Mechanical Engineering
Georgia Institute of Technology

Dr. Steven Liang
School of Mechanical Engineering
Georgia Institute of Technology

Dr. Thomas Kurfess
School of Mechanical Engineering
Georgia Institute of Technology

Date Approved: May 18, 2005

DEDICATION

To my parents,

Mr. Ichwan Kurnadi &

Mrs. Milawati Hardiwidjaja.

And my brother and sister,

Heru Prabowo Kurnadi &

Yoana Aryani Kurnadi.

ACKNOWLEDGMENTS

I would like to thank my thesis advisor, Dr. Shreyes Melkote for his invaluable support and encouragement towards the completion of this thesis. I would also like to thank the other members in my thesis committee, Dr. Steven Liang and Dr. Thomas Kurfess for their valuable suggestions and advice.

This thesis would not have been possible without the funding by the National Institute of Standards and Technology's Advanced Technology Program under contract #70NANBOH3045. I would also like to thank Mr. Dan Soroka at the Hardinge Company for his kindness loaning us a grip force meter.

I would particularly like to thank Steven Sheffield and Carl Laniak for the wealth of knowledge and experience they contributed toward the experimental aspects of the project. In addition, I would like to thank my fellow laboratory students Sathyan Subbiah, Sangil Han, Ian Harisson, Xavier Brun and Ramesh Singh for the help and cooperation with this project. Most of all, I would like to thank my family members for their constant support and encouragement throughout my life.

TABLE OF CONTENTS

LIST OF TABLES

LIST OF FIGURES

NOMENCLATURE

A	Ring cross sectional area.
$(C_{cl})_i$	Radial clamping force at contact i.
$(C_{net})_i$	Net radial clamping force at contact i.
C_{min}	Minimum clamping force.
δ_d	Desired roundness error.
$\delta_{total}(\gamma)$	Total ring deflection due to cutting and unclamping effect at location γ.
δ_{lower}	Lower bound of the allowable range of total ring deflection.
δ_{upper}	Upper bound of the allowable range of total ring deflection.
Δ_n	Overall peak-to-valley roundness error for n number of jaws.
$d_{eff}(\gamma)$	Effective depth of cut at location γ.
d_{nom}	Nominal depth of cut.
E	Elastic Modulus of ring material.
F_r	Radial cutting force.
F_t	Tangential cutting force.
γ	Angular location of cutting tool.
G	Shear Modulus of ring material.
H_i	Redundant force at contact i.
I_z	Moment of inertia about the z-axis.

M_0	Bending moment in the cross section at angular cross section datum.
M_θ	Bending moment in cross section at location ϕ.
n	Number of point contacts.
N_0	Normal force in the cross section at angular cross section datum.
N_θ	Normal force in cross section at location ϕ.
ϕ_i	Angle of contact point i.
P	Generic force.
P_i	Applied radial force at contact i.
Q_0	Shear force in the cross section at angular cross section datum.
Q_θ	Shear force in the cross section at angular cross section datum.
$Q(\ )$	Function that predicts the maximum stress in the workpiece.
r	Average ring radius.
r_{in}	Ring inner radius.
$r_{in}^{fin}(\gamma)$	Finished inner radius of the ring at location γ.
$r_{in}^{fin}(\gamma)$	Initial inner radius of the ring at location γ.
r_{out}	Ring outer radius.
$(R_{cut})_i$	Radial reaction force due to cutting force at contact i.
$(\sigma_{\theta\theta})_{max}$	Maximum circumferential stress.
SF	Design safety factor.
Sy	Yield strength of ring material.
θ	Angle of division measured from ring datum.

t	Thickness of rectangular ring cross section.
$(T_{cl})_i$	Tangential reaction force due to clamping at contact i.
$(T_{cut})_i$	Tangential reaction force due to cutting force at contact i.
$(T_{cut+cl})_i$	Tangential reaction force due to clamping and cutting force at contact i.
T_i	Tangential force applied at contact i.
μ	Constant associated with Biezeno and Grammel's equations.
μ_s	Coefficient of static friction.
U	Strain Energy in curved beam.
w	Width of rectangular ring cross section.
y	Radial displacement.
$y_{cl}(\theta)$	Radial deflection due to clamping at location θ.
$y_{cut}(\gamma)$	Radial deflection due to cutting at location γ.
ν	Constant associated with Biezeno and Grammel's equations.

SUMMARY

Workholding parameters such as the number of jaws and chucking force are known to influence the roundness tolerance of ring shaped parts commonly used in bearing applications. Experimental trial and error methods are often used in practice to optimize the workholding parameters to achieve the desired part quality. This thesis develops a systematic mathematical approach for optimizing these parameters using a theoretical finished cut roundness prediction model and a model for determining the reaction force between the chuck jaws and the ring.

In this thesis, the energy method is chosen for the determination of the internal forces, for prediction of deflection of the ring, and for the prediction of the reaction forces.

To verify the roundness prediction model, experiments were conducted for different cutting conditions and compared to the model predictions. Model prediction of the finished cut profile incorporating the chucking and cutting forces in turning of a ring yielded an average error of 19.9 % at the extreme points of the deformed ring. In addition, the mean absolute percentage error over all conditions was 8.5%. Those predictions were made by assuming the average of the inner diameters of the uncut and cut ring as the inner diameter in the theoretical model. For comparison, the theoretical model prediction

using the inner diameter of the cut ring as the inner diameter yielded a mean absolute percentage error of 22.1% over all conditions.

The optimization approach takes as input the required roundness tolerance, geometry and mechanical properties of the ring, cutting forces, and the coefficient of friction between the jaws and the ring. The output consists of the minimum number of jaws and the range of acceptable chucking forces that satisfy the required tolerance while preventing slip of the ring. An example case shows that the roundness capability of a conventional three jaw chuck is limited to 71.9 μm for the assumed ring material, geometry, and cutting conditions.

In addition, based on the optimization model, the thesis proposes two novel concepts of dynamic chucking force control that promise to yield part roundness that is superior to that obtained in conventional chucking. The first concept assumes equal chucking force at each jaw but the magnitude is allowed to vary with respect to the angular location of the cutting tool. The peak-to-valley roundness error of the cut ring produced by this model is 55.4 μm for the same conditions considered in the constant chucking force example.

The second concept consists of varying the individual jaw forces independently in such a way as to obtain the desired roundness error in the cut ring. This last model shows a significant improvement in peak-to-valley roundness error of the cut ring compared to the other two models. For the example case considered in the study, this last model yields a 5 μm peak-to-valley roundness error of the cut ring.

The models developed in this thesis make a contribution to the goal of developing a reliable workholding optimization procedure for ring shaped parts in turning operations.

CHAPTER 1

INTRODUCTION

1.1 Background

In turning, a single point cutting tool removes material from the external or internal surface of a workpiece rotating about its longitudinal axis. The workpiece is gripped at one end by a chuck mounted on the end of the main spindle of the machine. However, one of the limitations of the turning process is its ability to machine thin-walled ring shaped parts to small roundness tolerances comparable to grinding process. Typical roundness tolerances for high precision bearing applications can be as small as 5 μm.

An important but often overlooked component that affects the roundness tolerance of the ring in turning is the workholding or fixturing system. The purpose of the fixture in the turning process is to grip and rotate the workpiece during machining so that the cutting tool can penetrate and remove material from the workpiece. Figure 1.1 shows two types of fixtures that are commonly used for the turning process.

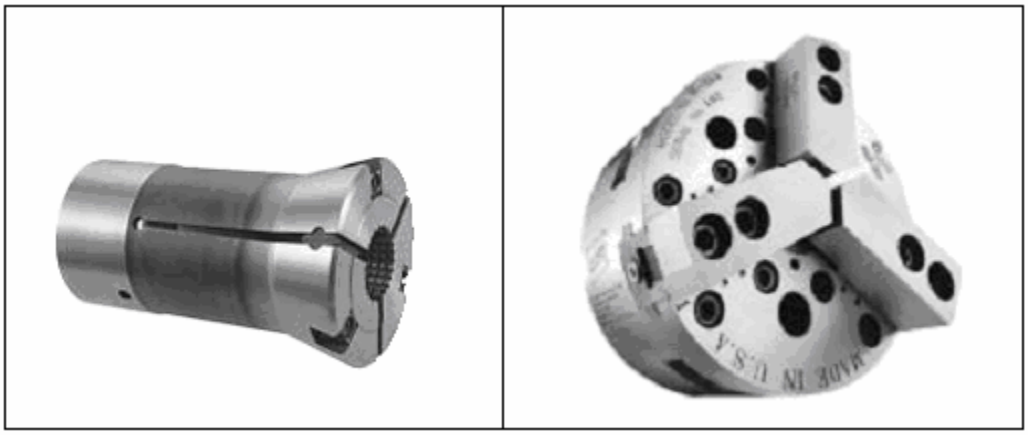

(a) Collet chuck **(b) Three jaw chuck**

Figure 1.1 Two typical workholding devices used in turning process [Hardinge Inc., 2002]

The collet and jaw chucks shown in Figure 1.1 are two commonly used devices for holding the workpiece in turning operations. When using the collet chuck, the diameter of the workpiece needs to match the hole size of the collet chuck to ensure that the workpiece is properly held. As a result, this leads to additional expense associated with the need to purchase and store various sizes of chucks and also increases changeover time. Therefore, a method to clamp the workpiece using the jaw chuck, is more favorable in terms of cost and time savings because it is capable of clamping different sizes of rings.

An important parameter that influences the roundness tolerance of the workpiece is the clamping force. However, there is a trade-off between the optimal chucking force and part stability in the chuck. A small chucking force cannot adequately restrain the workpiece during machining whereas a large chucking force results in excessive elastic

deformation of the ring leading to large roundness errors. Figure 1.2 serves to illustrate the development of roundness errors in the ring turning process.

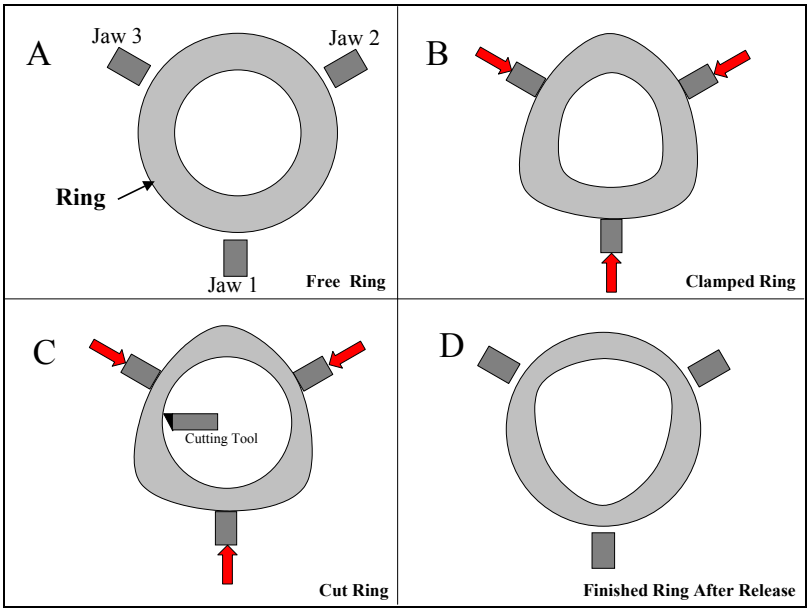

Figure 1.2 The influence of workholding forces on ring roundness profile [Malluck, 2003].

Figure 1.2a shows an undeformed ring inserted into a chuck before clamping forces are applied. In Figure 1.2b, when an initially round workpiece is clamped in the chuck with a given amount of clamping force, the workpiece is elastically deformed. Subsequently, as the inner diameter of the workpiece is cut in Figure 1.2c, the resulting cut surface is almost a true circle. In fact, cutting forces have an effect on the finished cut profile of the ring but these effects are excluded from this discussion because these effects are typically small in finish machining. Upon releasing the clamping force, the workpiece, due to its elastic nature, will tend to spring back to its initial shape.

Consequently, permanent roundness error will remain on the inner diameter of the workpiece, as shown in Figure 1.2d. This fact has been reported earlier by investigators [Reason, 1966].

In addition to the clamping force, operators typically use a chuck with a large number of jaws to achieve the required roundness tolerance. However, the cost and complexity of the chuck increases with the number of jaws. Therefore, this requires determination of the optimal number of jaws and the clamping force at each jaw location that keeps the part from slipping while at the same time producing distortion that is within the allowable limit.

In order to determine the optimal combination of the number of jaws and clamping force, an analytical model to predict the finished cut profile of the ring is required. Previous work performed in this area has presented an analytical model to predict in-plane deformation of ring shaped parts. However, the model only considered the chucking forces and ignored the effect of cutting forces on the profile of the cut ring. Previous work also lacks discussion of efforts to predict reaction forces between the workpiece and jaws. Therefore, this thesis seeks to develop a theoretical model for prediction of the finished cut profile of the ring that includes the effect of the cutting forces and a predictive model for the reaction forces at the interface between the workpiece and jaws. Subsequently, the finished cut profile prediction model is verified through experiments. Finally, based on the finished cut profile and the reaction force prediction models, this thesis presents a systematic mathematical approach for

determining the minimum number of jaws and the range of acceptable chucking forces that ensure the required ring roundness tolerance while preventing slip of the ring.

The primary objective of this thesis is the development of a systematic and model-based methodology for determining the optimum chucking conditions for turning of ring-shaped parts. The specific objectives are:

1) To develop a flexible analytical model that predicts finished cut profile of a cut ring held in a chuck with any number of jaws.
2) To develop an analytical model that predicts reaction forces between the jaws and workpiece held in a chuck with any number of jaws.
3) To experimentally verify finished cut prediction model extensively.
4) To develop optimization models based on the finished cut profile and reaction force prediction models.

1.2 Thesis Outline

This thesis is organized as follows. Prior relevant work on modeling and analysis of workholding in turning process are reviewed in Chapter II.

Chapter III discusses the development of theoretical models, which consist of two parts: i) a model that predicts finished cut profile of a ring held in a chuck and, ii) a model that predicts the reaction forces at the interface between the workpiece and the jaw surfaces. In addition, a finite element model of ring deformation is also developed to determine the finished cut profile and reaction forces between the workpiece and the jaw surface. The finite element model results are compared with the analytical model.

In Chapter IV, a detailed experimental validation of the finished cut profile is presented. This chapter discusses in detail the apparatus and procedures used to machine the ring-shaped workpiece, to measure the clamping force, and to inspect the cut profile of the ring after machining. In this chapter, the application of the analytical model is demonstrated by predicting the finished cut profile after cutting.

A chucking optimization model is presented in Chapter V. The methodology and the steps involved in the optimization process are illustrated through an example problem. The simulation example illustrates the use of the proposed workholding optimization approach for a turning application. In addition, based on the optimization model, the paper proposes a novel concept of dynamic chucking force control that promises to yield part roundness that is superior to conventional chucking.

Finally, the conclusions and recommendations of this thesis are presented in Chapter VI.

CHAPTER 2

LITERATURE SURVEY

Although fixture design methodology has been well investigated, little fixture design work has been directed towards the chucking of thin-walled ring shaped parts machined by the turning process. In this chapter, a review of prior relevant research is presented. The review of literature is divided into three categories. First, the relevant theoretical principles are reviewed to describe the theoretical fundamentals governing rings and their response to fixture-like loading conditions. Second, work discussing the application of the theoretical fundamentals to the turning process is reviewed in regard to predicting workpiece deformation and reaction forces. This is followed by an overview of published research in the area of clamping force optimization.

2.1 Theoretical Fundamentals

Similar to a straight beam, the theoretical model development of a loaded ring starts with identification of the internal hoop force N_θ, transverse force Q_θ, and bending moment, M_θ, at any cross section. The first step is to establish the in-plane forces that act

through a cut-section of the ring at θ equal to zero (N_0, Q_0, and M_0). Figure 2.1 shows the free body diagram of the ring subjected to an external radial force P_i and an external tangential force T_i applied at angular location Φ_i.

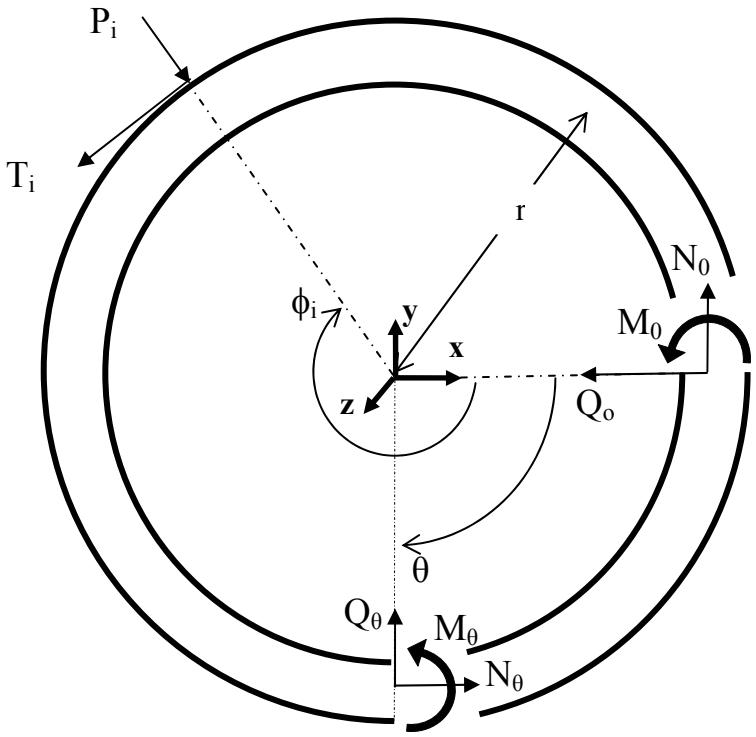

Figure 2.1 Free Body Diagram of the ring

The magnitude of the internal forces acting through a cut-section of the ring at $\theta = 0$ is statically indeterminate and may be found by the Castigliano theorem. In their extensive work on the mechanics of complete rings, Biezeno and Grammel have applied the Castigliano theorem to obtain the internal forces, N_0, Q_0, and M_0 [Biezeno and Grammel, 1956].

After the internal forces are determined, one of the most common techniques for predicting the in-plane deflection of a curved beam is using the governing differential equation.

$$\frac{\partial^2 y}{\partial \theta^2} + y = -\frac{M_\theta r^2}{EI_z} \tag{2.1}$$

This equation is derived using the bending theory of the curved beam. This expression relates the bending moment present in the cross section of the curved beam, M_θ, to the radial displacement, y.

The second approach uses the energy method. The deflection of the ring, y, due to an external load, P, may be obtained by differentiating the expression for the strain energy of the deformed ring, U, with respect to the corresponding external load. The theorem is expressed in Eq. (2.2).

$$y = \frac{\partial U}{\partial P} \tag{2.2}$$

The expression for the strain energy of the ring is given by Eq. (2.3) which contains the internal hoop force, transverse force, and internal bending moment expressions [Timoshenko, 1955].

$$U = \frac{1}{2}\left(\int_0^{2\pi} \frac{{N_\theta}^2 r}{EA} d\theta + k \int_0^{2\pi} \frac{{Q_\theta}^2 r}{GA} d\theta + \int_0^{2\pi} \frac{{M_\theta}^2 r}{EI_z} d\theta \right) \tag{2.3}$$

where E and G are the Young's modulus and Shear modulus of the ring, respectively. In addition, I_z is the area moment of inertia about the z axis (equal to $wt^3/12$ for a rectangular cross section of width w and thickness t) and A is the cross sectional area of

the ring. However, according to Timoshenko, in the case of a thin curved beam, the internal hoop force and transverse force may be neglected, and Eq. (2.3) reduces to:

$$U = \int_0^{2\pi} \frac{M_\theta{}^2 r}{EI} d\theta \tag{2.4}$$

Not only that a closed ring is internally statically indeterminate, when there are more than three reaction forces exerted on the ring, the problem becomes externally statically indeterminate as well. To effect a solution to such problems, a rigid body idealization of the ring is no longer adequate, and it is necessary to take ring deflection into account. Therefore, Castigliano's theorem is used again to obtain additional equations needed to determine the additional unknowns (the redundant reactions) in the statically indeterminate problem. This theorem states that:

$$\frac{\partial U}{\partial (H)_j} = 0 \tag{2.5}$$

where the denominator $(H)_j$ refers to the redundant force whose index $j = 4, \ldots, n$ and U refers to the strain energy of the deformed ring due to external loads. The same expression for the strain energy of the ring given in Eq. (2.4), which contains internal bending moment expression, may be used.

For the sake of consistency, the energy method is chosen throughout the entire analysis in Chapter 3 for the determination of the internal forces, for the prediction of deflection of the ring, and for the prediction of the reaction forces.

2.2 Application of Deformation Prediction Model in Turning Process

Davis and Kahg [Davis, 1976] used curved beam theory to derive a theoretical model to describe elastic deformations of a ring shaped part held in two, three, and four jaw chucks. However, the theoretical and experimental results displayed significant differences over the entire range of wall thicknesses examined. The major reason for the differences may be due to the effect of cutting forces that was neglected in their theoretical model.

Ito and Rahman [Ito, 1979] experimentally investigated factors that cause out-of-roundness and parallelism errors when turning the outer diameter of a solid cylindrical workpiece held in a three jaw chuck. They found that the machining accuracy is greatly influenced by the position of the jaw with respect to the radial component of the cutting force, the stiffness of the workpiece and the chucking and cutting conditions. Matin and Rahman [Matin, 1988] presented a theoretical analysis of the cutting dynamics of a solid cylindrical rotating workpiece clamped in a three jaw chuck. Their theoretical model was able to compute the effective depth of cut as a function of the location of the jaw with respect to the radial component of the cutting force. However, the source of out-of-roundness of thin-walled ring shaped parts is different from that of a solid cylindrical workpiece. In ring shaped parts, the main cause of out-of-roundness is the springback phenomenon [Malluck, 2003].

Stahl and Walter [Stahl, 1992] have addressed the issue of predicting the deformation of a ring shaped workpiece. Though no experimental results were presented to validate their ring deformation model, they compared the results predicted by their

model with those obtained from Roark and Young's equations and with those obtained from a finite element model. The influence of the cutting force was shown to be small compared to the deformations induced by the clamping forces.

Similarly, Malluck and Melkote [Malluck, 2003] presented a theoretical model for predicting the static deformations and finished cut profile of ring-type workpieces due to in-plane chucking forces only applied in a boring process. When the author tried to include the effect of cutting forces in the finished cut prediction model, the prediction error was over 100%, which was unacceptable. The method that the author used to combine the effect of cutting clamping was incorrect and is corrected in this thesis. In addition, Malluck also ignored the fact that the gripping force changes during cutting, which is caused by the radial reaction force induced at the jaw. Malluck's work also lacks of effort to optimize the workholding parameters in order to minimize distortion.

Mudiam and Nymekye have conducted a study of the magnitude of the radial clamping force during turning [Mudiam, 1992]. They conducted an experiment where they measured the net clamping force during machining and showed that the net clamping force changes periodically and its cycles in unit time equal the revolutions per unit time.

2.3 Workholding Parameter Optimization

Workholding parameter optimization is an important component of fixture design work. For example, the clamping forces are an essential parameter for restraining the workpiece in the fixture during machining. However, excessive clamping forces result in

large part distortion while too low clamping forces results in an unrestrained workpiece. There is considerable work in the area of clamping force optimization, particularly for the milling application.

Fuh and Nee [Fuh, 1994] used rigid body analysis of fixture-workpiece systems to find the minimum clamping forces required for kinematic restraint of a prismatic workpiece. However, the rigid body methods cannot predict workpiece elastic deformation and cannot predict the reaction force accurately. In addition, when more than three reaction forces to be found, the reaction forces cannot be easily obtained because the equilibrium conditions lead to only three equations. Such systems are statically indeterminate.

Hurtado and Melkote [Hurtado, 1998] presented a model for the prediction of normal and frictional reaction forces between rigid fixture elements and an elastic workpiece due to clamping and machining forces. Their proposed method was based on the application of a minimum energy principle and employs closed-form contact compliance solutions to fundamental contact mechanics problems. The model developed in their paper was specific to a 3-2-1 fixture configuration using planar tipped locators and clamps. However, the contact elasticity models assume that the fixture and workpiece are compliant only in the contact region and rigid elsewhere. Therefore, they cannot predict the deformation at the machining points.

In order to predict the deformation at the machining points accurately using the same 3-2-1 fixture configuration, Sathyanarayana and Melkote [Sathyanarayana, 2004] constructed a finite element model of the workpiece and fixture elements to take into

account compliances of the workpiece and the fixture in predicting deformation and reaction forces. An experimental study was conducted and the results were compared with predictions from a finite element model. Sathyanarayana and Melkote also compared the experimental reaction force results with those from contact elasticity method. The finite element method predicts the reaction forces better than the contact elasticity method.

Sathyanarayana and Melkote [Sathyanarayana, 2002] also developed an optimization process using the response surface method. This optimization model uses finite element models to predict the deformation of the workpiece at the machining point accurately. However, contact elasticity model was chosen to determine the feasible space for the design variables for the clamping force optimization problem. This is because the time taken by the contact elasticity algorithm to conclude non-existence of a feasible solution is considerably less than the time taken by the finite element software. However, in case of finding optimum clamping force in turning the inner diameter of a race bearing, contact elasticity algorithm might not be adequate because the compliance of the workpiece is very low (the thickness of the ring is a lot smaller than the diameter of the ring).

One of the few research works that discusses clamping force optimization in turning application is by Walter and Stahl [Stahl, 1994]. Walter and Stahl investigated the minimum necessary clamping force for turning a ring shaped workpiece held in a hand operated three jaw scroll chuck. Two different analytical models were developed based on two extreme cases: (i) the workpiece stiffness is greater than the stiffness of the jaws,

and (ii) the workpiece stiffness is less than the jaw stiffness. The workpiece assumed in the second analytical model matches a thin ring. However, the limitation of this analytical model was that it assumed that the cutting forces only affect the two nearest jaws.

2.4 Summary

Among all analytical models that predict the deflection of a thin ring discussed in the previous section, the analytical method developed by Melkote and Malluck [Malluck, 2003] is found to be the most flexible because it considers the varied location and magnitude of the clamping forces. In addition, it was shown to be in good agreement with the experiment. However, the experiments were conducted for only a single cutting condition.

In their work, the effect of cutting force on the finished cut profile was not fully understood. When the author tried to include the cutting forces in the finished cut prediction model, the prediction error was over 100%. The method that the author used to combine the effect of cutting and clamping was incorrect and is corrected in this thesis. In addition, the author also ignored the fact that the gripping force change during cutting, which is caused by the radial reaction force induced at the jaw. Malluck's work also lacks an effort to optimize the workholding parameters in order to satisfy the roundness tolerance.

Therefore, this thesis is focused on: (1) the creation of a finished cut prediction model that includes the effect of clamping and cutting forces. The fact that the magnitude of the clamping forces change during cutting is also considered, (2) the creation of a

reaction force prediction model induced at the jaw in the radial and tangential directions, (3) the experimental validation of the finished cut prediction model for various cutting conditions, and (4) the creation of a systematic mathematical approach for optimizing the workholding parameters using the theoretical model of ring deformation and a model for predicting the reaction force.

CHAPTER 3

MODEL DEVELOPMENT

In an effort to develop an optimization model that determines the optimal combination of the number of jaws and clamping force, a theoretical and a finite element model are developed in this chapter. The development of the theoretical model consists of two parts: i) a model that predicts the finished cut profile of a thin-walled ring held in a chuck with any number of jaws, and ii) a model that predicts reaction forces at the interface between the workpiece and jaw surfaces. Similarly, a finite element model is also developed to determine the finished cut profile and reaction forces between the workpiece and the jaws. The reaction forces obtained from the theoretical model can be compared with those obtained from the finite element model

3.1 Development of Theoretical Model

The theoretical model addresses the forces and deflections that occur in the plane of the ring ('in plane') because a majority of thin rings have a depth, *w*, that is several times larger than their thickness, *t*. As a result, the moment of inertia and bending rigidity

about the *z* axis is much smaller than in the other two axes that lie in the plane of the ring. In addition, the forces in the *z* direction, such as the axial cutting force are typically less than those applied radially. Other assumptions made in the development of the ring deflection model are as follows:

i) The ring material obeys the laws of linear elasticity while the jaws are assumed to be rigid.

ii) Strain hardening and residual stress effects in the ring are neglected.

iii) Out of plane forces are neglected.

iv) Cutting forces in the radial and tangential directions are constant.

v) All loads are assumed to be point loads.

vi) In the calculation of strain energy, the inner and outer radii of the ring are considered to be equivalent. A radius *r*, which is the average of the inner and outer radii, is assumed.

vii) The local contact deformations due to clamping and cutting forces acting on the ring are negligible.

3.1.1 Ring Deflection Model

Since the resulting finished cut profile of the ring and the reaction force are derived from the ring deflection calculation, it is necessary to model the deflection of the ring due to external loads. The general conventions for external load applied at a single point on the ring are shown in Figure 3.1.

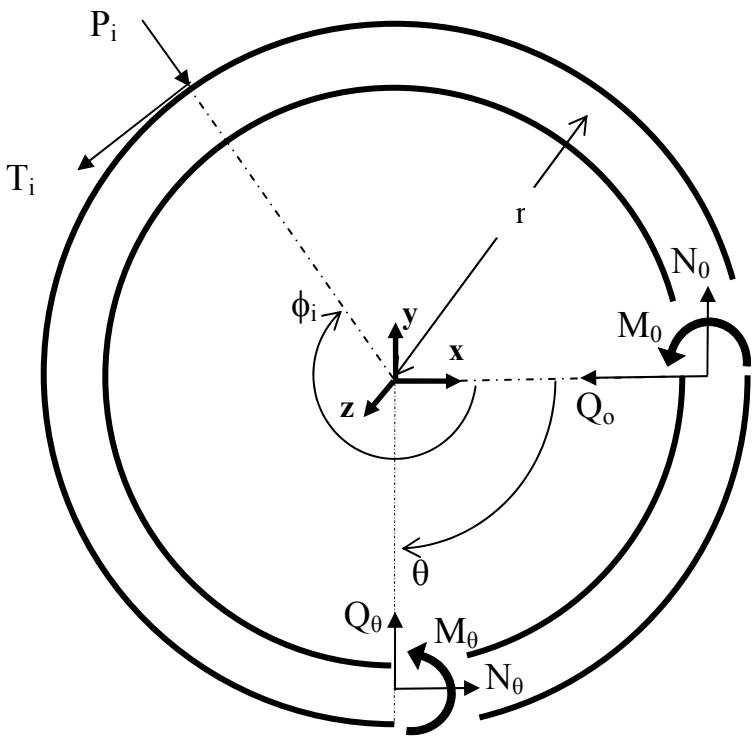

Figure 3.1 Ring with force conventions for internal and external loads

An external radial force P_i and an external tangential force T_i are applied at angular location Φ_i. The index, i, refers to the i^{th} contact on the ring. The model can handle any number, n, of these point contacts.

The theoretical model development starts with identification of an in-plane hoop force N_0, transverse force Q_0, and bending moment M_0, shown in Figure 3.1 that act through a cut-section of the ring at θ equal to zero. Biezeno and Grammel have applied the Castigiliano theorem to obtain the following expressions for the aforementioned quantities [Biezeno, 1956]:

$$N_0 = \sum_{i=1}^{n} \frac{\phi_i}{2\pi} P_i \sin\phi_i + \sum_{i=1}^{n} \frac{\phi_i}{2\pi} T_i \cos\phi_i - \sum_{i=1}^{n} \frac{\mu}{2\pi} T_i \sin\phi_i \tag{3.1}$$

$$Q_0 = \sum_{i=1}^{n} \frac{\phi_i}{2\pi} P_i \cos\phi_i - \sum_{i=1}^{n} \frac{\phi_i}{2\pi} T_i \sin\phi_i - \sum_{i=1}^{n} \frac{\mu}{2\pi} T_i \cos\phi_i \tag{3.2}$$

$$M_0 = -rN_0 - \sum_{i=1}^{n} \frac{P_i r}{2\pi} + \sum_{i=1}^{n} \frac{\phi_i}{2\pi} T_i r \tag{3.3}$$

In these expressions, μ and ν are constants defined as:

$$\mu = \frac{-\frac{1}{EA} + k\frac{1}{GA} + \frac{1}{EI_z} r^2}{\frac{1}{EA} + k\frac{1}{GA} + \frac{1}{EI_z} r^2} \tag{3.4}$$

$$\nu = \frac{\frac{1}{EI_z} r^2}{\frac{1}{EA} + k\frac{1}{GA} + \frac{1}{EI_z} r^2} \tag{3.5}$$

where E and G are the Young's modulus and Shear modulus of the ring respectively; k is a numerical factor depending on the ring cross section. In addition, I_z is the area moment of inertia about axis z (equal to $wt^3/12$ for rectangular cross section of width w and thickness t) and A is the cross sectional area of the ring.

Using the above expressions, the internal hoop force N_θ, transverse force Q_θ, and bending moment, M_θ, at any cross section θ can be expressed in terms of N_0, Q_0, M_0 and the contributions of the external loadings, $\overline{N}_\theta, \overline{Q}_\theta, \overline{M}_\theta$ as follows:

$$N_\theta = N_0 \cos\theta - Q_0 \sin\theta + \overline{N}_\theta \tag{3.6}$$

$$Q_\theta = N_0 \sin\theta + Q_0 \cos\theta + \overline{Q}_\theta \tag{3.7}$$

$$M_\theta = N_0 r(1-\cos\theta) + Q_0 r \sin\theta + M_0 + \overline{M}_\theta \tag{3.8}$$

The clamping force, net radial force and net tangential reaction force P_i, and T_i applied at Φ_i contribute the quantity $\overline{N}_\theta^{\phi_i}, \overline{Q}_\theta^{\phi_i}, \overline{M}_\theta^{\phi_i}$ to $\overline{N}_\theta, \overline{Q}_\theta, \overline{M}_\theta$ so that for $0 \le \theta \le \Phi_i$

$$\overline{N}_\theta^{\phi_i} = 0 \tag{3.9}$$

$$\overline{Q}_\theta^{\phi_i} = 0 \tag{3.10}$$

$$\overline{M}_\theta^{\phi_i} = 0 \tag{3.11}$$

whilst $\Phi_i \le \theta \le 360°$

$$\overline{N}_\theta^{\phi_i} = -P_i \sin(\theta - \phi_i) + T_i \cos(\theta - \phi_i) \tag{3.12}$$

$$\overline{Q}_\theta^{\phi_i} = P_i \cos(\theta - \phi_i) + T_i \sin(\theta - \phi_i) \tag{3.13}$$

$$\overline{M}_\theta^{\phi_i} = P_i r \sin(\theta - \phi_i) + T_i r[1 - \cos(\theta - \phi_i)] \tag{3.14}$$

According to Castigliano's theorem, the deflection of the ring, *y*, due to an external load, *P*, may be obtained by differentiating the expression for the strain energy of the deformed ring, *U*, with respect to the corresponding external load. The theorem is expressed in Eq. (3.15). The expression for the strain energy of the ring is given by Eq. (3.16) which contains the internal hoop force, transverse force, and internal bending moment expressions [Timoshenko, 1955].

$$y = \frac{\partial U}{\partial P} \tag{3.15}$$

$$U = \frac{1}{2}\left(\int_0^{2\pi} \frac{N_\theta{}^2 r}{EA} d\theta + k \int_0^{2\pi} \frac{Q_\theta{}^2 r}{GA} d\theta + \int_0^{2\pi} \frac{M_\theta{}^2 r}{EI} d\theta \right) \tag{3.16}$$

However, according to Timoshenko, in the case of a thin curved beam, the internal hoop force and transverse force may be neglected, and Eq. (3.16) reduces to :

$$U = \int_0^{2\pi} \frac{M_\theta{}^2 r}{EI} d\theta \tag{3.17}$$

To find the deflection of the ring at a point away from the applied load, a fictitious force may be applied at the location and in the direction of the deflection of interest. Subsequently, the strain energy expression can be differentiated with respect to the fictitious force. However, since the fictitious force does not act on the ring structure, the value of the fictitious force needs to be set to zero and subsequently, the deflection can be solved. To obtain the deformation throughout the ring, the fictitious force needs to be moved and reapplied at angular location θ ranging from 0 to 360°.

3.1.2 Effect of Clamping Force

In a conventional chuck, the ring is restrained by displacing the jaws toward the center of the chuck, and as a result of the interference between the ring and the jaws a radial clamping force is exerted on the ring. In the absence of the cutting forces and when each equally spaced jaws are displaced by the same amount, an equal initial radial clamping force $(C_{cl})_i$, is exerted on the ring. Thus, because of equilibrium, no tangential

reaction force $(T_{cl})_i$ is induced at the jaw. However, due to geometrical errors in the chuck, the resulting radial clamping force at each jaw, $(C_{cl})_i$ will be different and consequently a tangential reaction force, $(T_{cl})_i$ is typically induced at the jaw in order to maintain equilibrium.

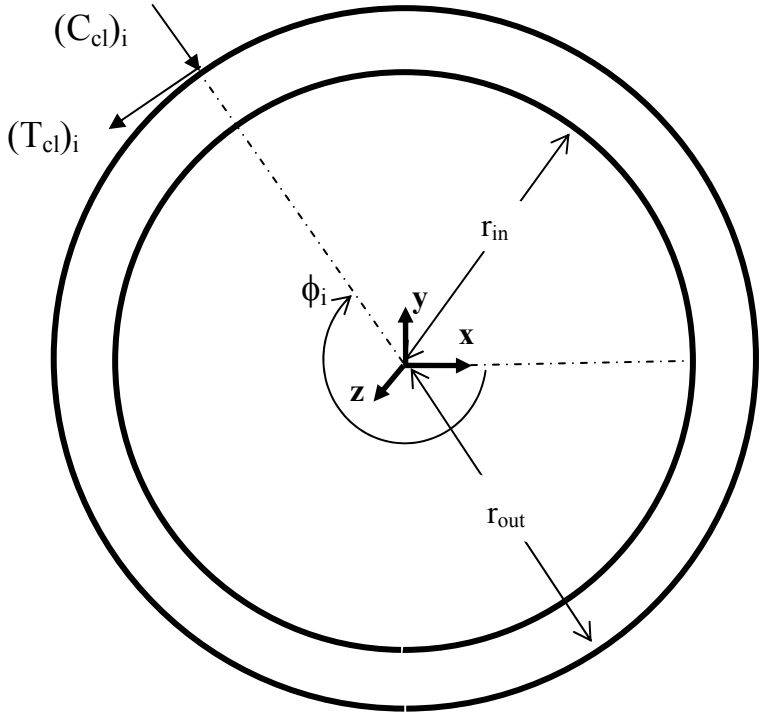

Figure 3.2 Jaw forces due to clamping

When the number of jaws equals to two or three, the tangential reaction force can be easily obtained using equilibrium conditions.

$$\sum F_x = \sum_{i=1}^{n} (C_{cl})_i \sin\phi_i + \sum_{i=1}^{n} (T_{cl})_i \cos\phi_i = 0 \tag{3.18}$$

$$\sum F_y = \sum_{i=1}^{n} (C_{cl})_i \cos\phi_i - \sum_{i=1}^{n} (T_{cl})_i \sin\phi_i = 0 \tag{3.19}$$

$$\sum M_z = \sum_{i=1}^{n} (T_{cl})_i r_{out} = 0 \tag{3.20}$$

However, when the number of jaws, *n*, is larger than three, the tangential reaction forces cannot be easily obtained because the equilibrium conditions lead to only three equations while there are more than three reactions to be found. Such systems are statically indeterminate. Regarding $(C_{cl})_1, \ldots, (C_{cl})_n$ as prescribed forces, consideration of equilibrium alone allows an infinite number of combinations of values for $(T_{cl})_1, \ldots, (T_{cl})_n$. In particular, $(n-3)$ of the tangential reaction forces are said to be redundant since if they were removed, equilibrium could still be maintained. From a purely static point of view it is immaterial which of $(T_{cl})_1, \ldots, (T_{cl})_n$ are regarded as the redundant reactions. However, in this discussion, $(T_{cl})_4, \ldots, (T_{cl})_n$ are regarded as the redundant reactions.

To effect a solution to such problems, a rigid body idealization of the ring is no longer adequate, and it is necessary to take ring deflection into account. Therefore, Castigliano's theorem for deflections is used to obtain additional equations needed to determine the additional unknowns (the redundant reactions) in the statically indeterminate problem. This theorem states that:

$$\frac{\partial U}{\partial (T_{cl})_j} = 0 \tag{3.21}$$

where the denominator $(T_{cl})_j$ refers to the redundant force whose index $j = 4, \ldots, n$ and U refers to the strain energy of the deformed ring due to external loads $(C_{cl})_i$ and $(T_{cl})_i$. The

same expression for the strain energy of the ring given in Eq. (3.17), which contains internal bending moment expression, may be used.

After the tangential reaction force $(T_{cl})_i$ is obtained, the deflection of the ring due to external loads $(C_{cl})_i$ and $(T_{cl})_i$ at angular location θ can be obtained using the steps discussed in Section 3.1.1 and may be represented as $y_{cl}(\theta)$

.

3.1.3 Effect of Cutting Force

During cutting, radial and tangential cutting forces, F_r and F_t, respectively are applied at the instantaneous angular location of the cutting tool γ. The axial cutting force is ignored in this analysis, since the model only considers the influence of in-plane forces. As a result of the applied cutting forces, a radial reaction force $(R_{cut})_i$, and a tangential reaction force $(T_{cut})_i$, are induced at the i^{th} jaw at an angular location Φ_i. All loads and angles are counted positive in the directions and sense indicated in Figure 3.3.

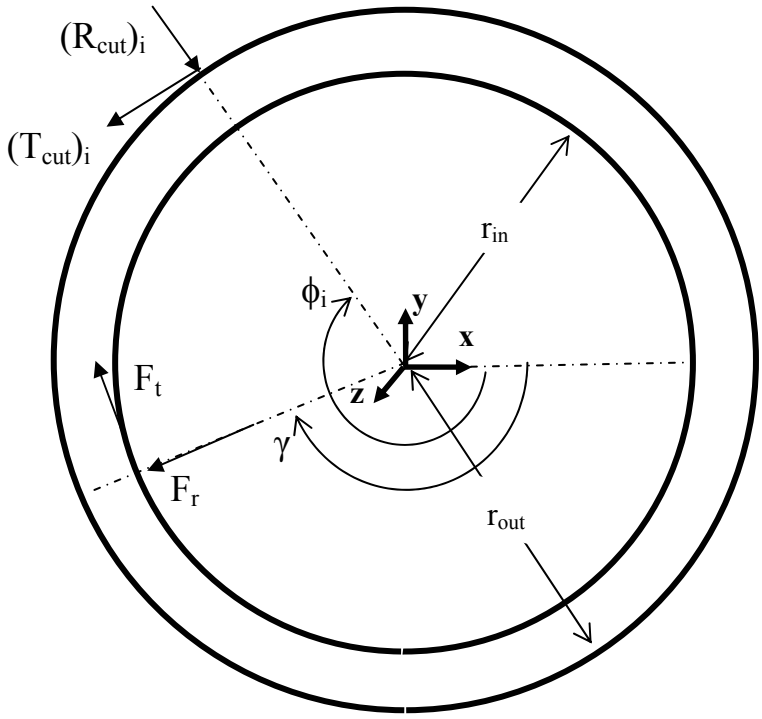

Figure 3.3 Forces present due to cutting force

Mudiam and Nymekye have conducted a study of the magnitude of the radial clamping force during cutting [Mudiam, 1992]. They conducted an experiment where they measured the net clamping force during machining and showed that the net clamping force changes periodically and its cycles in unit time equal the revolutions per unit time. The gripping force change is caused by the radial reaction force induced at the jaw. According to Mudiam and Nymekye, this sudden gripping force change may be detrimental if precision workpieces are machined. With this in mind, the radial reaction force, $(R_{cut})_i$, at every angular location of the cutting tool needs to be calculated so that the corresponding net clamping force may be obtained.

First, to maintain equilibrium, two force and one moment equilibrium equations may be expressed in terms of the in-plane cutting forces and reaction forces, as follows:

$$\sum F_x = \sum_{i=1}^{n} (R_{cut})_i \sin\phi_i + \sum_{i=1}^{n} (T_{cut})_i \cos\phi_i - F_r \sin\gamma - F_t \cos\gamma = 0 \tag{3.22}$$

$$\sum F_y = \sum_{i=1}^{n} (R_{cut})_i \cos\phi_i - \sum_{i=1}^{n} (T_{cut})_i \sin\phi_i - F_r \cos\gamma + F_t \sin\gamma = 0 \tag{3.23}$$

$$\sum M_z = -F_t r_{in} + \sum_{i=1}^{n} (T_{cut})_i r_{out} = 0 \tag{3.24}$$

However, the reaction forces cannot be easily obtained because the equilibrium conditions lead to only three equations while there are more than three reactions to be found. An approach similar to that discussed in Section 3.1.2 to solve the statically indeterminate problem may be used here. Although it is immaterial which reaction forces are regarded as the redundant reactions, in this discussion $(T_{cut})_4, \ldots, (T_{cut})_n$ and $(R_{cut})_1, \ldots, (R_{cut})_n$ are regarded as the redundant reactions. Next, Castigliano's theorem for deflections can be used to obtain additional equations needed to determine the unknown redundant reactions in this statically indeterminate problem. This theorem states that:

$$\frac{\partial U}{\partial (T_{cut})_j} = 0 \tag{3.25}$$

$$\frac{\partial U}{\partial (R_{cut})_k} = 0 \tag{3.26}$$

where the denominator $(T_{cut})_j$ refers to the redundant force whose index $j = 4 \ldots n$, $(R_{cut})_k$ refers to redundant force whose index $k = 1 \ldots n$, and U refers to the strain energy of the

elastically deformed ring due to loads $(R_{cut})_i$ and $(T_{cut})_i$. The same expression for the strain energy for a ring given in Eq. (3.17) is used.

After the reaction forces $(R_{cut})_i$ and $(T_{cut})_i$ are obtained, the deflection of the ring due to external loads F_r, F_t, $(R_{cut})_i$, and $(T_{cut})_i$ can be obtained using the steps discussed in Section 3.1.1. However, only the deflection at the tool tip is important for predicting the final roundness profile of the ring because this defines the position of the material as the tool encounters it. Since the tool tip is at an angle γ, the theoretical model can be generalized to find the deflection at the tool tip by changing the general location θ in the deflection expression to γ. Thus, the deformation at the tool tip $y_{cut}(\gamma)$ can be computed for γ between 0° and 360°.

During cutting, when the tool tip is at an angle γ, tangential reactions $(T_{cut})_i$ are produced between each jaw and the ring. To ensure that the ring does not slip in the chuck during cutting, the following constraint derived from the Coulomb friction law is applied:

$$|(T_{cut})_i| \leq \mu_s (C_{net})_i \tag{3.27}$$

$$(C_{net})_i = (C_{cl})_i + (R_{cut})_i \tag{3.28}$$

where, μ_s is the coefficient of static friction for the jaw and ring material pair; $(C_{net})_i$ is the net radial clamping force exerted on the ring at angular location of the jaw Φ_i . The index i refers to the i^{th} jaw of the chuck. When the cutting tool is located at angular positions ranging from 0° to 360°, the tangential reaction forces at all jaws are monitored to ensure that they do not violate Coulomb's law of friction.

3.1.4 Derivation of Finished Cut Profile

As described in Figure 1.2, the roundness error of the cut ring is influenced mainly by unclamping the ring after machining, assuming that the inner surface of the machined ring is closed to a true circle. However, this assumption is not necessarily true due to the deflection caused by the cutting force acting on the ring during cutting.

The cutting forces generated in ID turning cause the inner surface of the ring to deflect away from the ring center in the radial direction. Consequently, the effective depth of cut, d_{eff} is less than the nominal depth of cut, d_{nom} :

$$d_{eff}(\gamma) = d_{nom} - y_{cut}(\gamma) \tag{3.29}$$

The difference between the actual and nominal depths of cut at various angular location of the cutting tool also contributes to the roundness error of the finished profile of the ring.

It can be shown that the radius of the finished inner surface of the ring, $r_{in}^{fin}(\gamma)$, as a function of the tool tip location γ after clamping, cutting and unclamping is given by the following:

$$r_{in}^{fin}(\gamma) = \left[r_{in}^{init} + d_{eff}\right] - y_{cl}(\gamma) \tag{3.30}$$

Substitute Eq. (3.29) into Eq. (3.30):

$$r_{in}^{fin}(\gamma) = r_{in}^{init} + d_{nom} + \delta_{total}(\gamma)$$

$$\delta_{total}(\gamma) = -y_{cut}(\gamma) - y_{cl}(\gamma) \tag{3.31}$$

where, r_{in}^{init} is the initial (unclamped) inner radius of the ring, $y_{cl}(\gamma)$ is the ring deflection due to clamping forces and is positive in the direction of increasing radius, d_{nom} is the nominal depth of cut is assumed to be measured from the initial inner radius, and $y_{cut}(\gamma)$ *is* the ring deflection due to cutting forces and has the same sign convention as $y_{cl}(\gamma)$. In addition, $\delta_{total}(\gamma)$ is the total ring deflection due to cutting and unclamping effect.

In Eq. (3.31), the first term represent the effects of cutting, while the last term represents the effect of unclamping the ring after the cut is made. Note that after machining the material recovers elastically to its free state causing the machined profile to move radially away from the center. The roundness profile of the cut ring after unclamping, $\delta_{total}(\gamma)_{LS}$ may now be obtained by computing the least squares deviation of the overall deflection finished ring inner profile (given by Eq. (3.31) for $0 \leq \gamma \leq 360°$).

Subsequently, the overall peak-to-valley roundness error of the ring may be obtained as follows:

$$\Delta_n = \delta_{total}(\gamma)_{\max} - \delta_{total}(\gamma)_{\min} \tag{3.32}$$

The subscript n is used because the form of the analytical equation for Δ changes with n, the number of jaws. In the most general case, Δ_n is a function of variables such as the chucking force, ring material properties, geometry, and cutting forces.

3.1.5 Typical Results

An example is presented to demonstrate the typical result obtained from the theoretical model. The ring is modeled with an outer diameter of 71 mm, an inner diameter of 58 mm and a depth of 18.5 mm with three initial radial clamping forces C_{cl} of 2281 N each, located at 0°, 120° and 240°. A Young's modulus, E, of 202 GPa and a shear modulus of 79.2 GPa were used for the ring material properties. The MATLAB mathematical software was used to solve the theoretical model (given by Eq.(3.30)).

3.1.5.1 Typical Results of Reaction Forces

Because equal initial radial clamping force $(C_{cl})_i$, are applied on the ring, from equilibrium considerations no tangential reaction force $(T_{cl})_i$ is induced at the jaws. However, when the cutting forces (115 N tangential force and 215 N radial force) are applied to the inner diameter of the ring, a radial reaction force $(R_{cut})_i$ and a tangential reaction force $(T_{cut})_i$ are induced at the jaws. It is assumed that the ring is stationary while the cutting tool rotates. The resulting radial forces (R_{cut}) are shown in Figure 3.4.

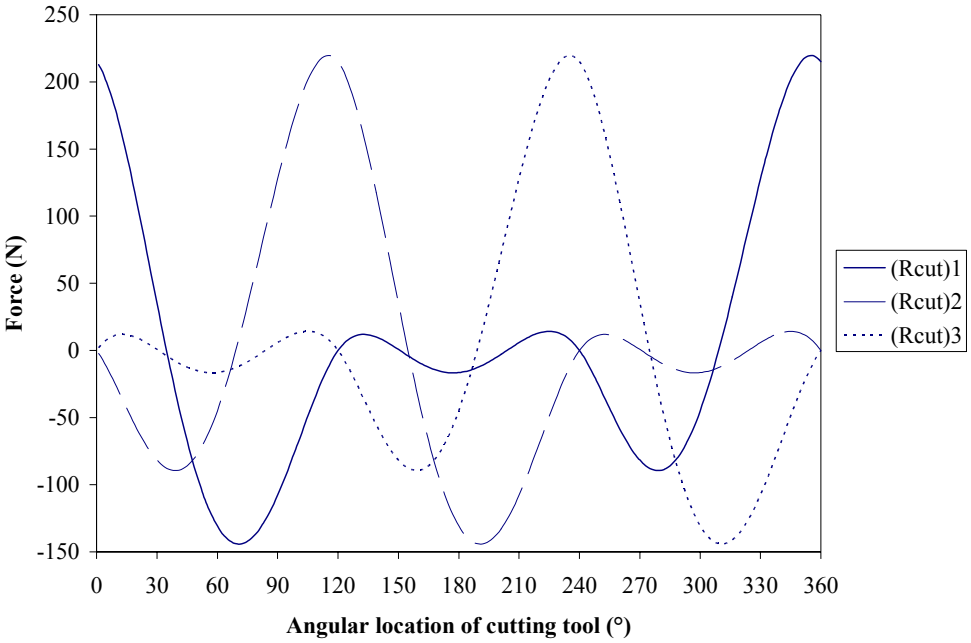

Figure 3.4 Resulting radial reaction force

The resulting tangential reaction force $(T_{cut})_i$ at each jaw for cutting force applied at angular location $\gamma = 0°$ to $360°$ is shown in Figure 3.5.

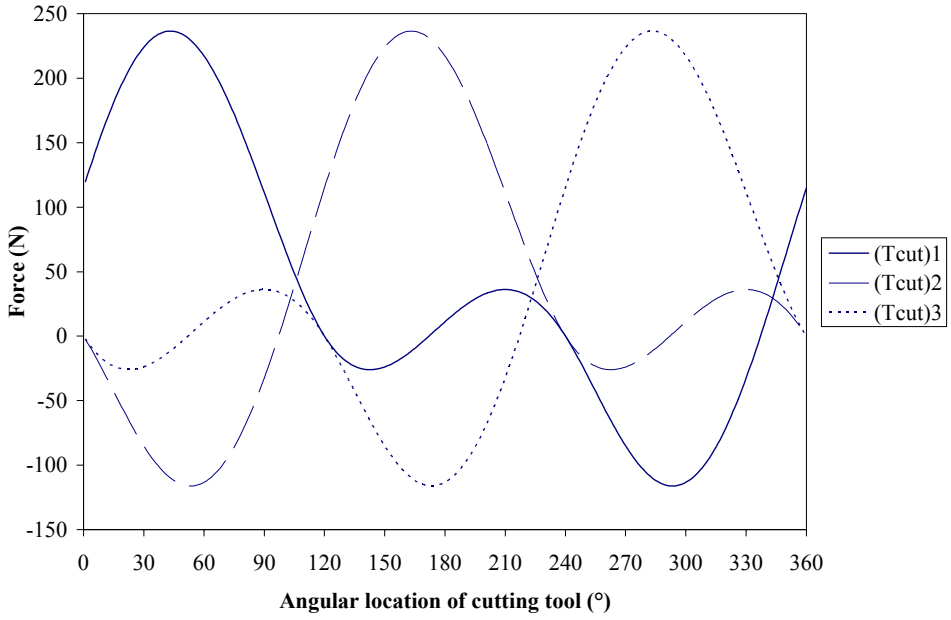

Figure 3.5 Resulting tangential reaction force

In Figure 3.4 and Figure 3.5, it may be observed that the reaction forces at jaw 1, jaw 2 and jaw 3 are periodic and identical but they are offset by 120°. To verify the effect of radial cutting forces alone on the reaction force, first the radial reaction force at jaw 1 due cutting force applied in the radial direction alone (215 N) are shown in Figure 3.6.

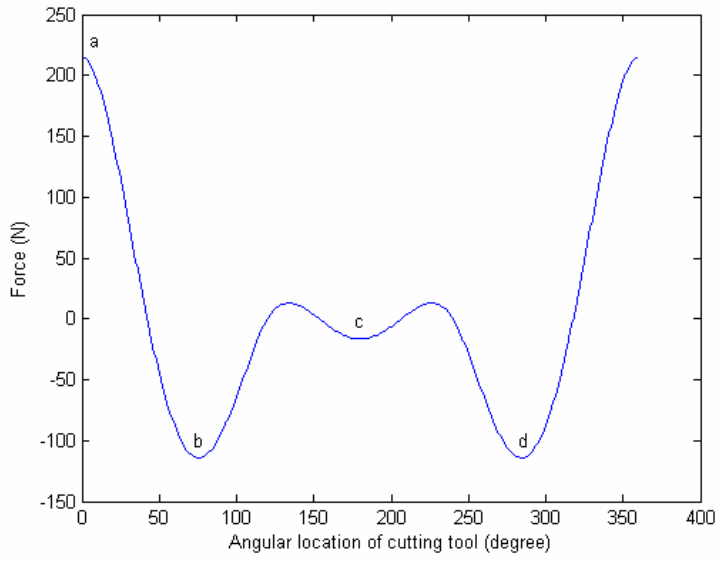

Figure 3.6 Radial reaction force at jaw 1 due to radial cutting force of 215 N

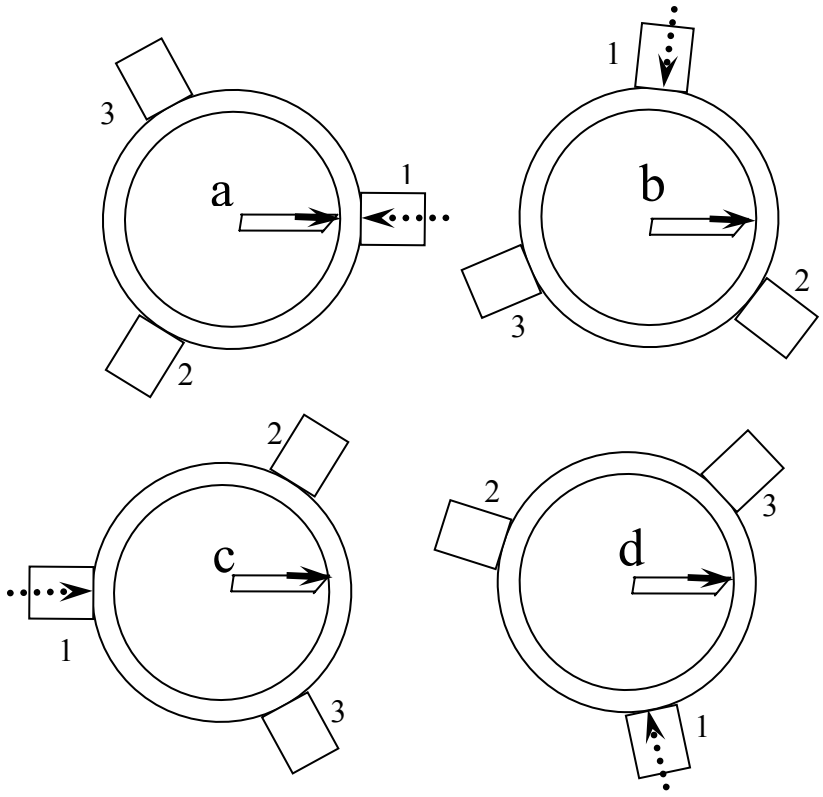

Figure 3.7 Positions of the jaw with respect to the radial component of cutting force

Figure 3.7 shows various positions of the jaw with respect to the radial component of the cutting force. From Figure 3.7a - Figure 3.7d, the jaws rotate in a counter clockwise direction. Radial reaction forces are represented by dotted arrows. The radial reaction force at jaw 1 reaches its maximum when the radial component of the cutting force pushes the workpiece against jaw 1, which is at an angular location of 0° (Figure 3.7a). When the direction of the radial cutting force is nearly perpendicular to the radial reaction force at jaw 1 (angular location of 75° and 285°) in Figure 3.7b and Figure 3.7d, the radial reaction force at jaw 1 reaches its minimum. Here, the radial component of the cutting force pulls the workpiece away from jaw 1. The reason that the radial reaction force at jaw 1 does not reach its minimum at angular location of 90° and 270° is because reaction forces are also induced at jaws 120° apart from jaw 1. In Figure 3.7c, when the cutting tool is placed between jaws 2 and 3, the radial cutting force is less influential on the radial reaction force induced at jaw 1.

A similar analysis can be made to verify the effect of radial cutting forces (215 N) on the tangential reaction forces induced at jaw 1. The resulting reaction forces with respect to the angular location of the cutting tool are plotted in Figure 3.8.

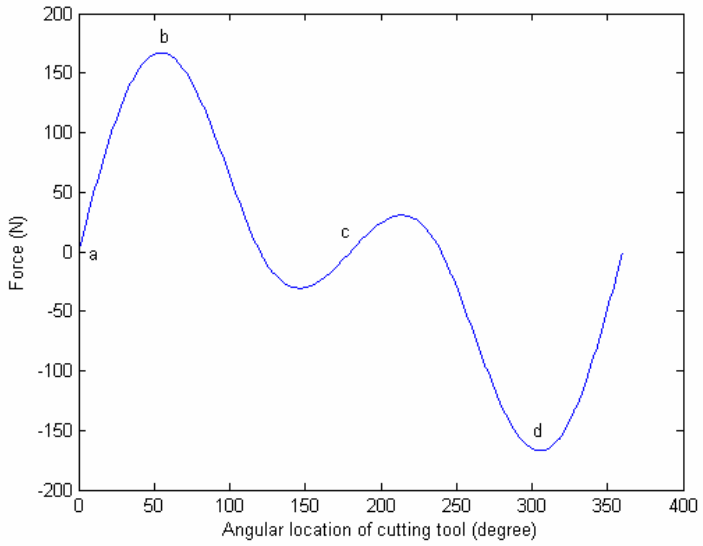

Figure 3.8 Tangential reaction force at jaw 1 due to radial cutting force of 215 N

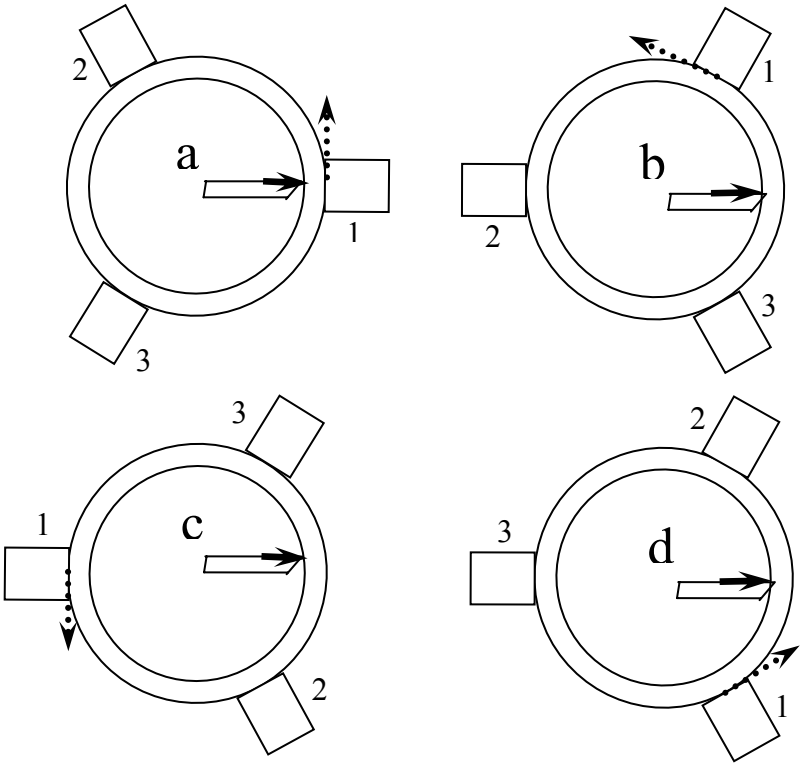

Figure 3.9 Positions of the jaw with respect to the radial component of cutting force

Figure 3.9 shows various positions of the jaw with respect to the radial component of the cutting force. The tangential reaction force induced at jaw 1 is represented by dotted arrows. According to Figure 3.8 and Figure 3.9, when the radial component of cutting force is perpendicular to the tangential reaction force, the magnitude of the tangential reaction force is equal to zero (Figure 3.9a and Figure 3.9c). The tangential reaction force at jaw 1 reaches its maximum when the tangential component of the cutting force is nearly parallel and in the opposite direction of the tangential reaction force at jaw 1 (Figure 3.9b). On the other hand, when the tangential component of the cutting force is nearly parallel but in the same direction as the tangential reaction force at jaw 1, its magnitude is minimum. In Figure 3.8, it can also be observed that when the cutting tool is placed between jaws 2 and 3, the effect of the tangential cutting force is less influential on the tangential reaction force induced at jaw 1.

Similar analysis may be performed to verify the effect of tangential component of the cutting force. Figure 3.10 and Figure 3.11 depict the effect of tangential component of cutting force alone (115 N) on the radial reaction force. Figure 3.12 and Figure 3.13 depict the effect of the tangential component cutting force alone (115 N) on the tangential reaction force.

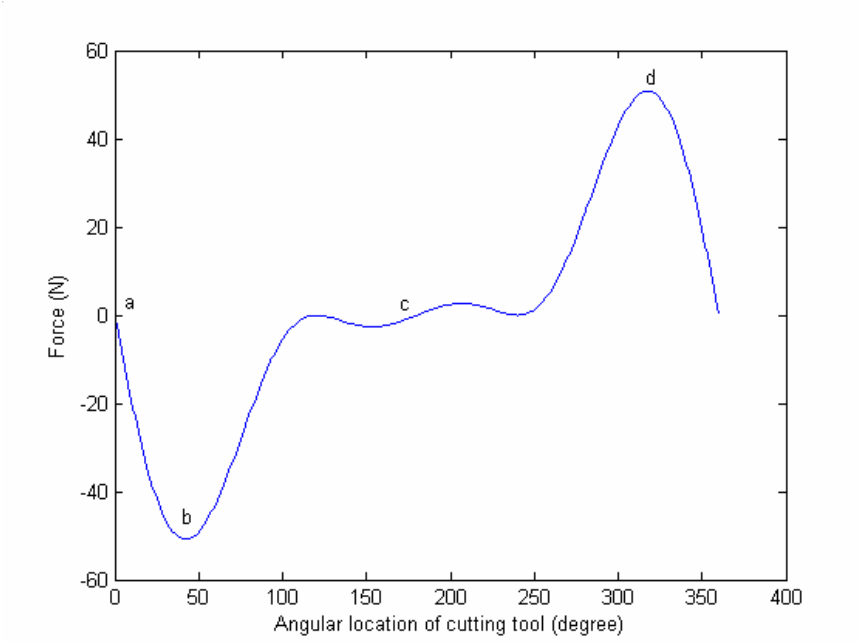

Figure 3.10 Radial reaction force at jaw 1 due to tangential cutting force of 115 N

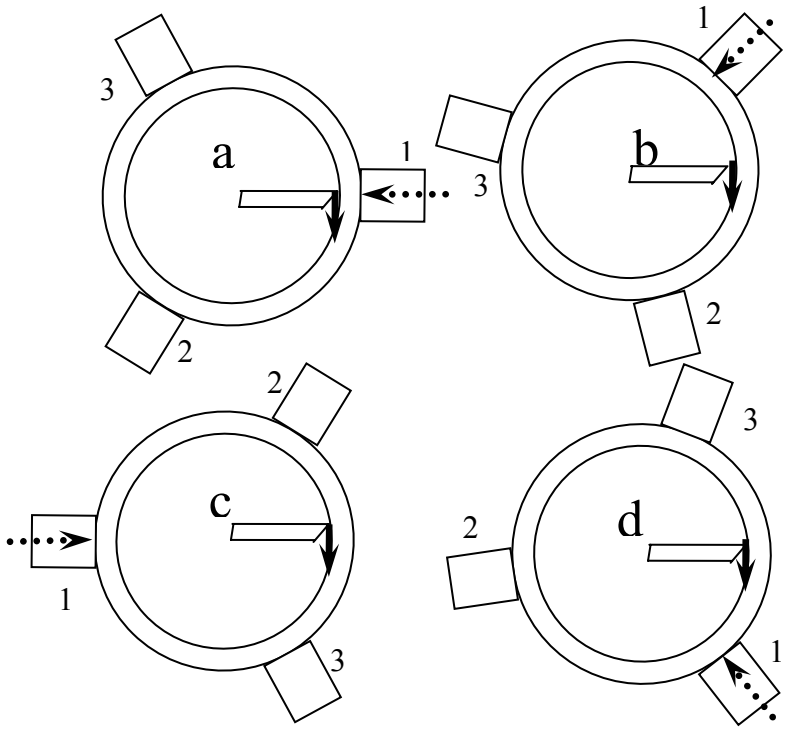

Figure 3.11 Positions of the jaw with respect to the tangential cutting

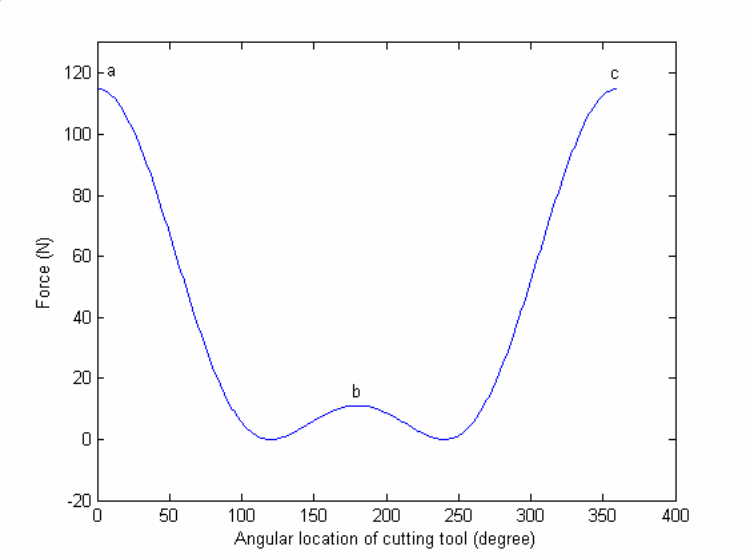

Figure 3.12 Tangential reaction force at jaw 1 due to tangential cutting of 115 N

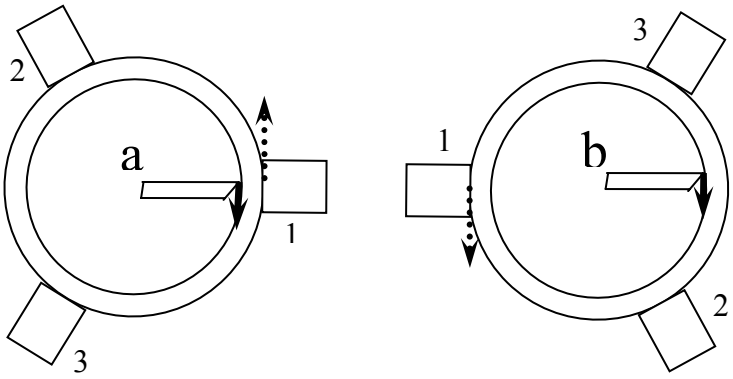

Figure 3.13 Positions of the jaw with respect to the tangential cutting

From the above analysis, it is obvious that the reaction forces induced at the jaws are greatly influenced by the direction of the cutting forces and the position of the jaws with respect to the cutting force.

3.1.5.2 Typical Results of Radial Deflection

The predicted radial deflection due to the initial radial clamping force, $y_{cl}(\theta)$ is shown in Figure 3.14 by a solid line. Figure 3.14 also shows the predicted radial deflection of the ring due to the cutting force, $y_{cut}(\gamma)$, by a dashed line. The radial force and tangential reaction force in Figure 3.4 and Figure 3.5 are used as inputs to the theoretical model that predicts the deflection of the ring due to both clamping and cutting forces.

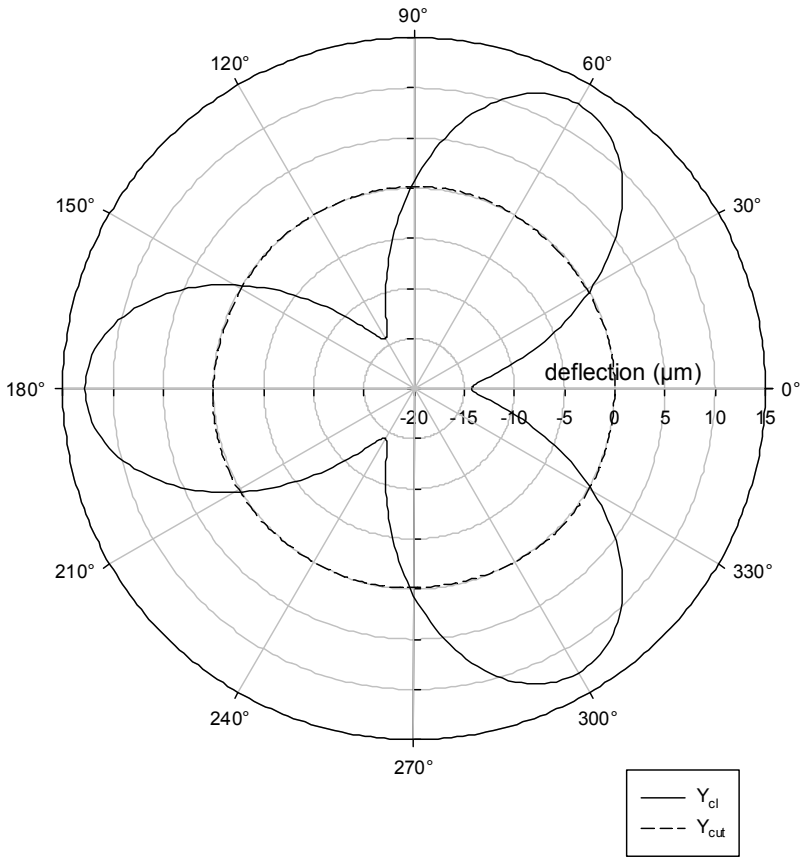

Figure 3.14 Typical radial deflection of ring at different angular locations

As shown in Figure 3.14, the model predicts that the ring will have a three-lobe shape when the three radial clamping forces are applied to the ring. Note that the ring

bows radially inward $y_{cl}(\theta)$ at angles of 0, 120 and 240 degrees where the radial clamping forces are applied.

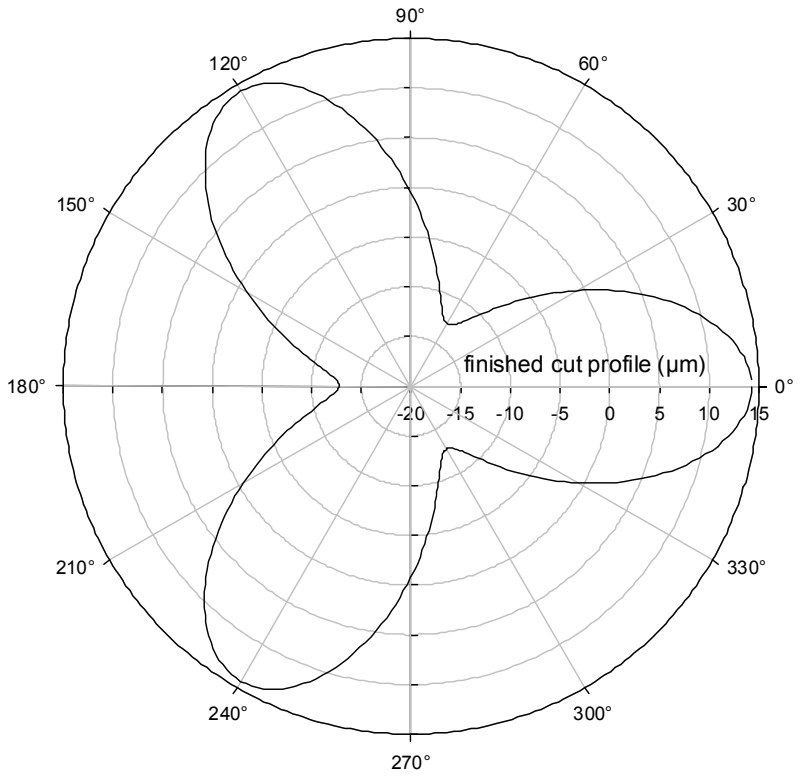

Figure 3.15 Predicted finished cut profile of ring inner surface

Using both predicted quantities, $y_{cl}(\theta)$ and $y_{cut}(\gamma)$, the calculation of the roundness of the cut ring, explained in Section 3.1.4, may be performed. The solid line in Figure 3.15 is the predicted roundness profile of the cut ring. The overall peak-to-valley roundness error of the ring in this example is 27.4 μm.

3.2 Development of Finite Element Model

Resulting finished cut profile and reaction forces obtained from the theoretical model are compared with those obtained from the finite element model.

3.2.1 Modeling in ANSYS

A 3D finite element model of the ring and jaws was created and solved using the APDL programming language of ANSYS®. The APDL code allow easy modifications of dimension, mesh size, and boundary conditions in the finite element model. In order to assess the preliminary capability of the model, first, the thin ring was modeled with an outer diameter of 71 mm, an inner diameter of 58 mm and a depth of 18.5 mm. However, the thin ring was created using three 119° large sections and three 1° short sections in between the large sections. This subdivision minimizes the computational time when surface-to-surface contact elements are used between the jaw and ring surfaces. The geometry of the jaws was modeled with a height of 25 mm, a width of 20 mm and a depth of 18.5 mm. The ring and jaw materials were assumed to be high carbon steel with a Young's Modulus of 201.33 GPa and a Poisson's ratio of 0.299. Similar to the geometry of the ring, each jaw was created using two large sections and a 1 mm short section in between the large sections. Figure 3.16a shows the unmeshed geometry of the ring and three jaws.

The ring and jaws were meshed using Solid45 elements. Solid45 elements were chosen because they have a brick shape geometry that allows uniform and mapped meshing and also they provide three degrees of freedom at each of the eight corner nodes.

The sizes of the mesh were determined by subdividing the line lengths of the rings and jaws. When meshing the ring, finer meshes were applied to the ring segments that are in contact with the jaws. These finer meshes allow a better contact pressure distribution on the contact surface. Figure 3.16b displays the meshed geometry of the finite element model.

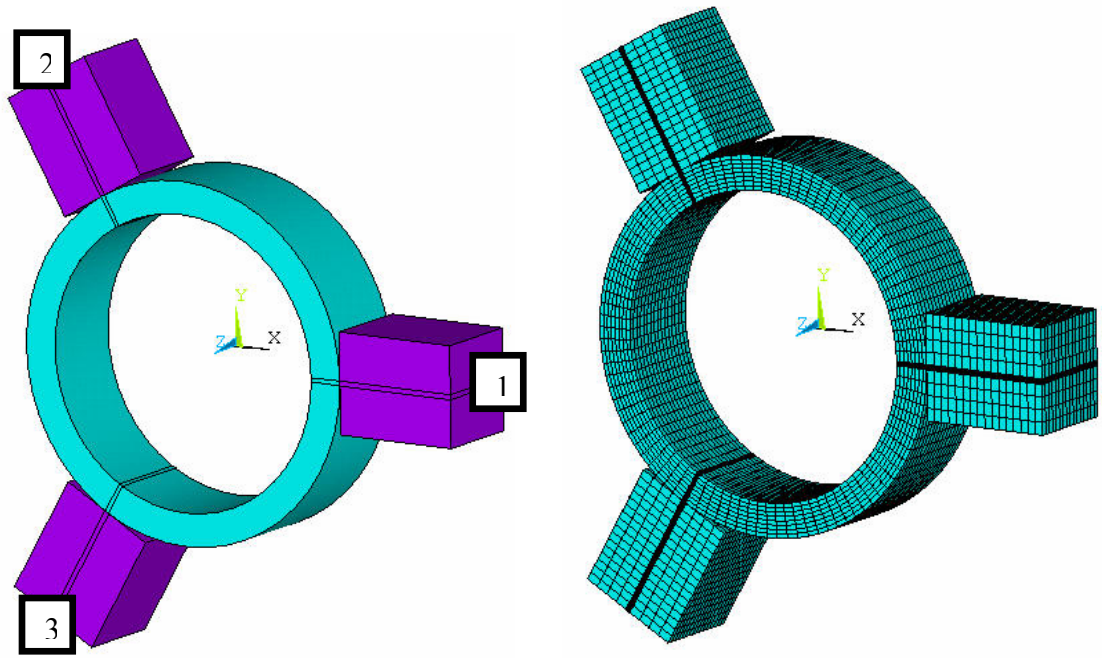

Figure 3.16 Geometry of finite element model

To simulate friction between the ring and jaws, contact elements were established between the surface of the jaw and the target surface, which is the surface of each ring segment that is in contact with the jaw. This was performed using the contact wizard in ANSYS®. For this preliminary assessment, a coefficient of friction 0.2 was used for the contacts.

Subsequently, the boundary conditions were applied to the model. The nodes on the bottom surfaces of all jaws (the rear surfaces in Figure 3.16) were constrained in the direction of the ring's axis and in the direction tangent to the ring. The direction of the ring's axis is shown as the z direction in Figure 3.16. Since, the direction tangent to the ring is unique for each jaw, the coordinate systems of the nodes on the bottom surfaces of all jaws were rotated so that the tangential directions could be constrained. These nodes were constrained in those two directions due to their close approximation to a real three jaw chuck. In addition, the nodes were displaced in the radial direction to simulate the pushing movement of the jaws onto the ring. As a result, clamping forces are exerted onto the ring by the jaws. For preliminary assessment, the amount of displacement was adjusted so that the amount of clamping force exerted on the ring by each jaw is approximately 2281 N. Finally, the components of the cutting force obtained in machining of hardened AISI 52100 steel taken from a previous experiment, 115 N tangential force and 215 N radial force, were applied to the inner diameter of the ring.

3.2.2 Convergence Analysis

In finite element analysis the structure is discretized into a certain number of elements. Through this approximation of the real structure an error is induced to the model. For a valid model, this error should reduce as the mesh is refined and the deflection and reaction force results should exhibit convergence towards a final value.
In an area where two bodies are potentially in contact, a high mesh density is preferable. Since the actual area of contact between the bodies is usually very small, a coarse mesh

accurately may not reflect in the actual contact pressure distribution between the workpiece and jaw, which may contribute to inaccurate reaction force results. In the study of contact zone mesh density, a reasonable overall mesh density (mesh density for the entire model apart from the contact zone) is assumed and held constant. The contact zone mesh density in the ring and jaw was controlled by defining the number of subdivision of lines in the geometry of short sections of the ring and jaw. This was accomplished by setting variables, R_CONT_PERIM and J_WIDTH_CONT, in the APDL code. These variables are listed in the Table 3-1 for each mesh. In addition, the unconverged and converged contact pressure contour plots are shown in Figure 3.17 and Figure 3.18, respectively. Figure 3.19 shows the contact pressure profile located in the middle of the ring as a function of the mesh size.

Table 3-1 Mesh Sizes for the Contact Pressure Distribution Convergence Analysis

Mesh		1	2	3	4	5
APDL parameters	R_PERIM	32	32	32	32	32
	R_CONT_PERIM	2	4	8	12	16
	R_DEPTH	16	16	16	16	16
	R_THICK	8	8	8	8	8
	J_WIDTH_CONT	2	4	8	12	16
	J_WIDTH_SIDES	4	4	4	4	4
	J_DEPTH	16	16	16	16	16
	J_HEIGHT	16	16	16	16	16
Number of solid elements		21186	23040	25344	27648	32256
Number of contact elements		192	384	576	768	1152
Total elements		21378	23424	25920	28416	33408
Element size at contact (mm)		0.5	0.25	0.125	0.083	0.063

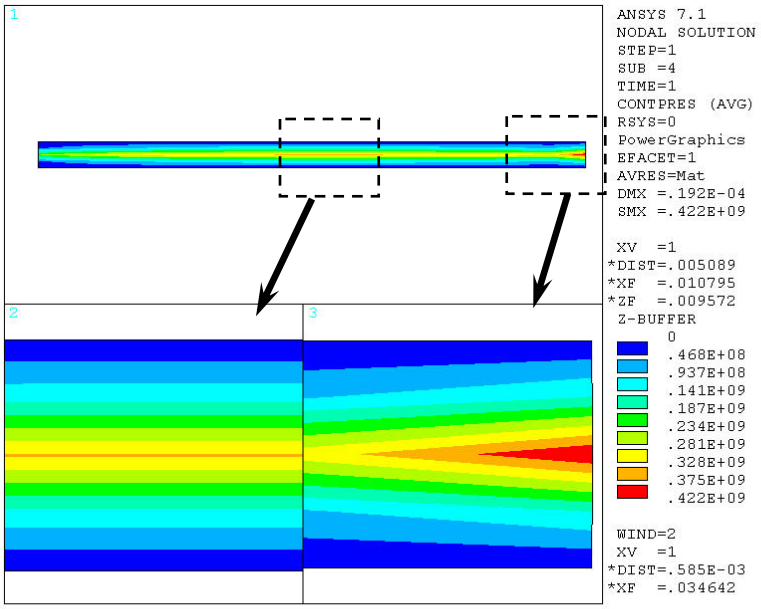

Figure 3.17 Unconverged contact pressure contour plot obtained with Mesh 1

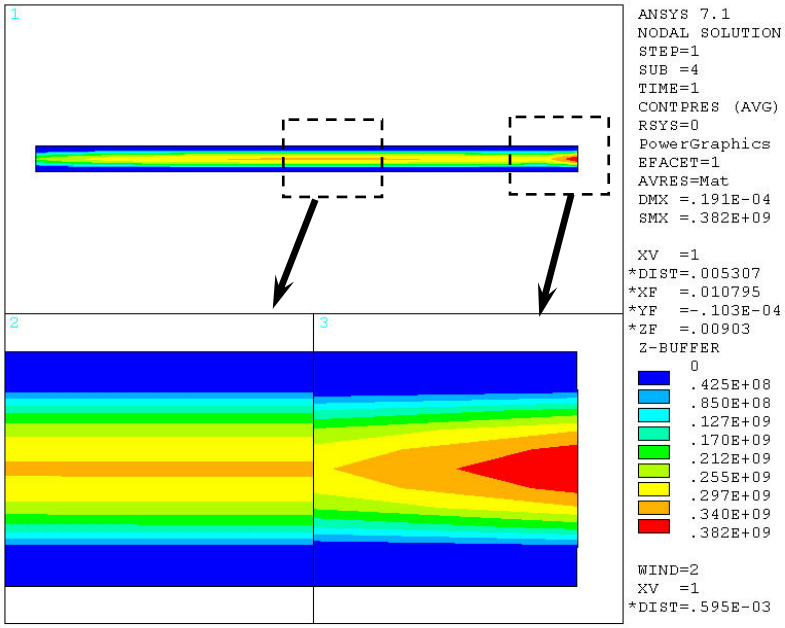

Figure 3.18 Converged contact pressure contour plot obtained with Mesh 3

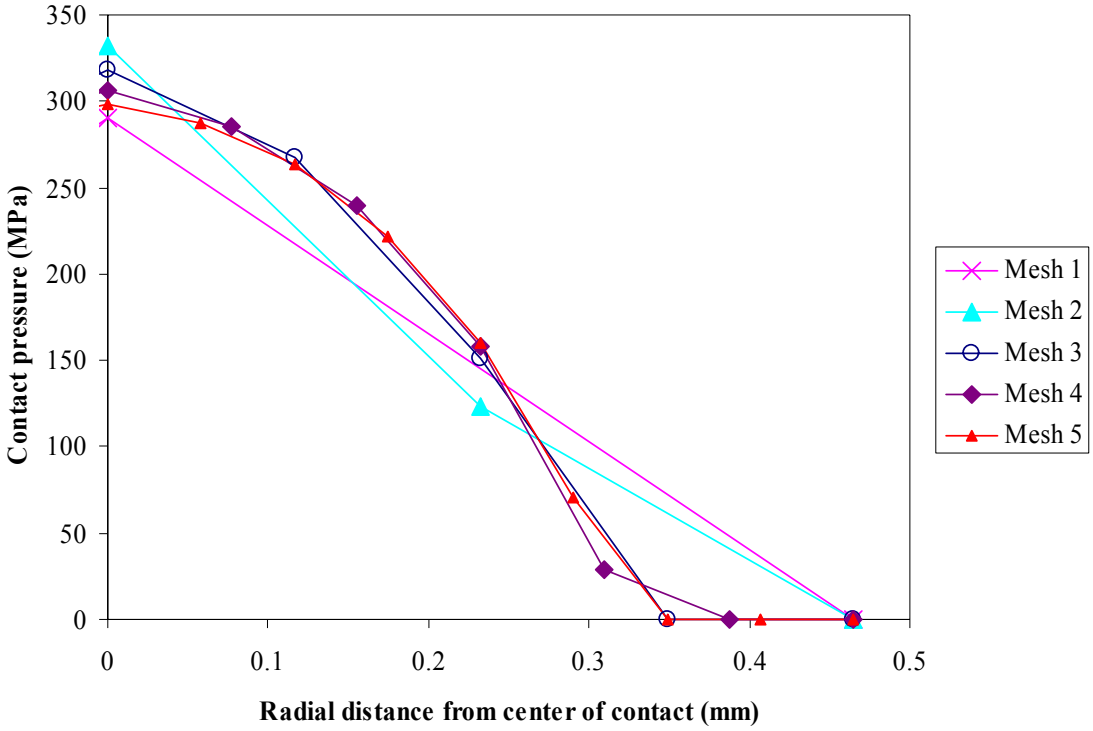

Figure 3.19 Contact pressure profile at jaw 1 from FEM as a function of mesh size

The previous figures show that a fine mesh can simulate the pressure distribution profile better than a coarse mesh. However, in order to capture the variation of contact pressure over the entire contact region, the average contact pressure is proposed as the convergence criteria. Other parameters that need to be checked for their convergence are the contact deformation and deflection of the ring.

To obtain the deflection of the ring, the position of the nodes along the inner diameter was examined. A path of nodes running circumferentially at the mid section of the ring's depth was selected as a suitable means to sample the ring deflection. The radial distance of these nodes from the original undeformed ring center was obtained

along with the angular position about the *z* axis. The center of the original undeformed ring is the origin of the coordinate frame shown in Figure 3.16. The positive rotational angle is defined to be clockwise from the *x* positive axis shown in Figure 3.16. The contact deformation of the ring is obtained in a similar way; however the positional node to observe is located at the center of the contact between the ring and the first jaw. Both ring deflections and contact deformation are defined negative toward the ring center.

The following table lists the value of the deflection of the ring at 0, 30, 60, 90 degrees, and the corresponding contact deformation.

Table 3-2 Ring deflection and contact deformation

Mesh		1	2	3	4	5
Average contact pressure (MPa)		96.64	115.7	128.4	133.1	135.5
Ring deflection (μm)	0°	-16.5	-16.3	-16.3	-16.3	-16.3
	15°	-10.7	-10.6	-10.6	-10.6	-10.6
	30°	-0.4	-0.4	-0.4	-0.4	-0.4
	45°	8.3	8.2	8.2	8.2	8.2
	60°	11.7	11.6	11.6	11.6	11.6
Contact deformation (μm)		-17.6	-17.4	-17.3	-17.3	-17.3

It is seen in Table 3-2 that the ring deflections and contact deformation results converged at a coarse mesh density (Mesh 1) when compared to the average contact pressure results (Mesh 4). Therefore, convergence of the ring deflections and contact deformation does not ensure convergence of the average contact pressure. As a compromise between adequate time for the solution and sufficient accuracy of the result, mesh 4 (element size = 0.083 mm in the contact zone) was chosen for the further analysis of the given problem.

The overall mesh density was refined by changing the APDL parameters (R_PERIM, R_DEPTH, R_THICK, J_WIDTH_SIDES, J_DEPTH, J_HEIGHT) while the contact

zone mesh density was held constant (element size = 0.083 mm in the contact zone). The variation in the value of average contact pressure, ring deflection, and contact deformation was found to be within 3% for finer overall mesh densities.

3.2.3 Typical Output

After running the finite element model using Mesh 4, the converged ring deflections and reaction forces were obtained and evaluated. The results obtained are for a ring with a 58 mm inner diameter, a 71 mm outer diameter, and a 18.5 mm width subjected to clamping forces as a result of displacing the three jaws located at 0°, 120° and 240°. As a result of the displacement of 20 μm towards the center of the ring, clamping forces of approximately 2280 N are exerted on the ring by each jaw.

3.2.3.1 Typical Results of Radial Deflection

The solid line in Figure 3.20 shows the ring deflection subjected to clamping forces only. During the actual turning process the cutting force revolves around the inner diameter. Therefore, the displacement at the cutting force location is of interest since only this displacement causes geometry errors after the machining operation. Unlike, the theoretical model, it is impossible to find the displacement of the ring due to cutting alone without the clamping force acting on the ring. In addition to deflecting the ring, the clamping forces also restrain the ring during the application of the cutting force as long as

the Coulomb's Law of Friction is satisfied. Therefore, an expression to find the deflection of the ring due to cutting is given by:

$$y_{cut}(\gamma) = y_{cl+cut}(\gamma) - y_{cl}(\gamma) \tag{3.33}$$

where $y_{cl}(\gamma)$ is the ring deflection due to clamping forces, $y_{cl+cut}(\gamma)$ *is* the ring deflection due to clamping and cutting forces and $y_{cut}(\gamma)$ *is* the ring deflection due to cutting forces. All three are positive in the direction of increasing radius.

Ring deflection due to clamping forces and cutting forces is represented by dotted lines in Figure 3.20. In addition, the ring deflection due to the cutting force is shown by a dashed line with triangular markers. The angular location of the cutting force is increased approximately every 10°.

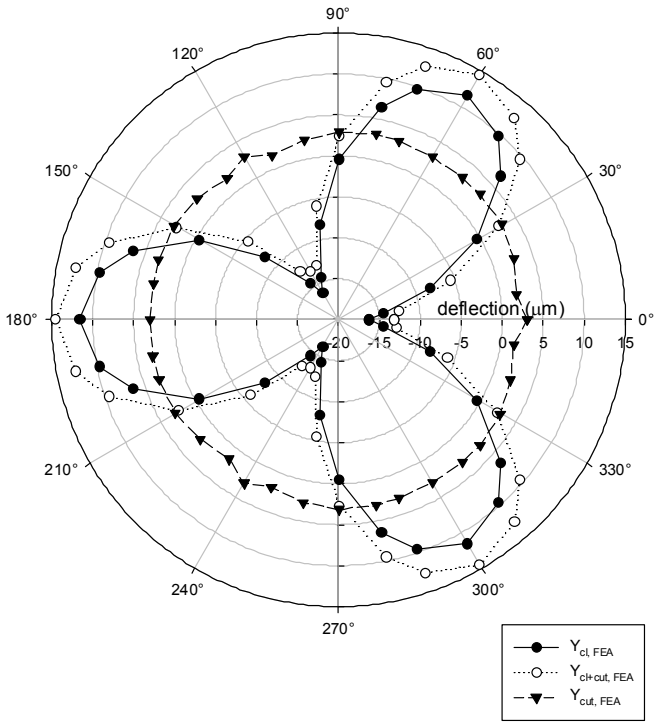

Figure 3.20 Radial deflections obtained from Finite Element Analysis

After obtaining the ring displacement due to clamping and cutting forces, a finished cut profile of the ring may be predicted using the method discussed in Section 3.1.4. The finished cut profile of the ring is shown in Figure 3.21. The predicted overall peak-to-valley roundness error for the finish cut profile of the ring is 27.7 μm. This predicted value is consistent with the overall peak-to-valley roundness error predicted by the theoretical model, which is 27.4 μm.

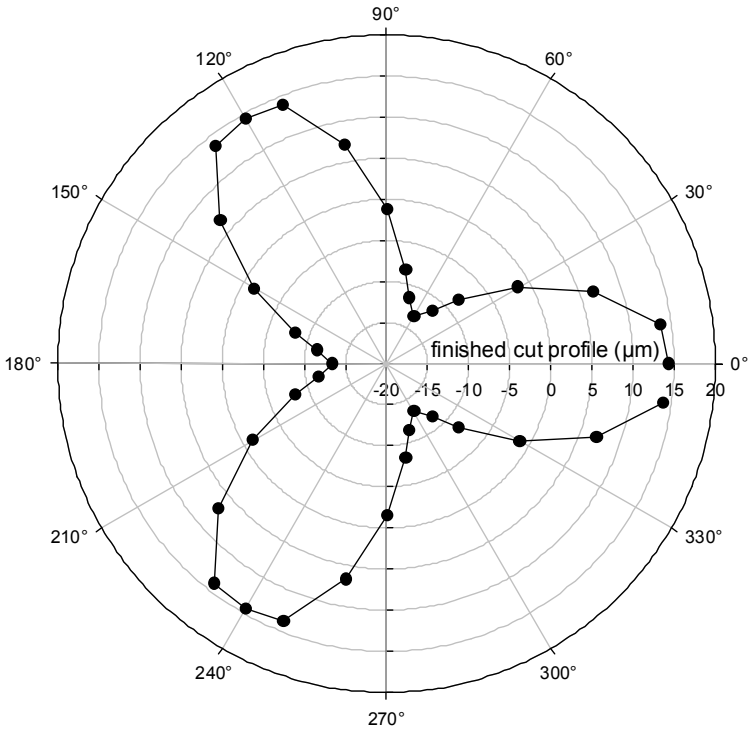

Figure 3.21 Finished cut profile obtained from Finite Element Analysis

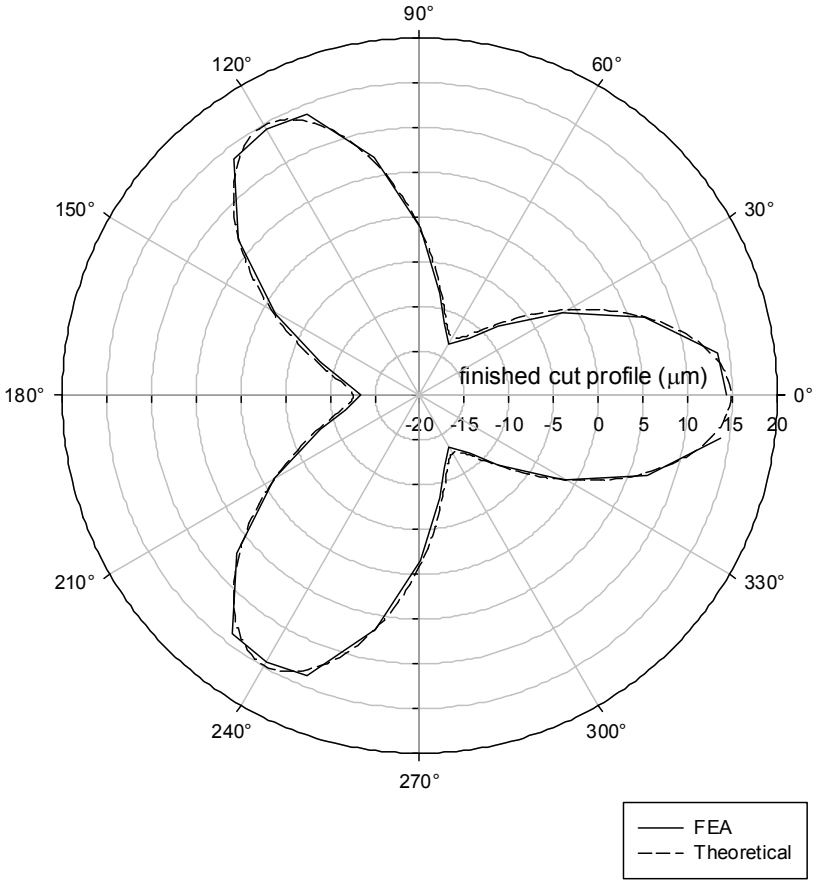

Figure 3.22 Comparison of finished cut profile between FEA and theoretical model

Figure 3.22 shows comparison of the finished cut profile obtained using finite element analysis and theoretical model. The theoretical model seems to agree very well with the finite element model. Another important result that can be obtained from the finite element model is the reaction force between the workpiece and the jaws.

3.2.3.2 Typical Reaction Force Results

To obtain the radial and tangential reaction forces at the interface between the workpiece and jaws, the net radial force and the net tangential reaction force at the nodes over the contact area were collected and summed. Figure 3.23 shows the net radial reaction force induced at jaws 1, 2, and 3 as a function of the angular location of the cutting tool. Figure 3.24 shows the net tangential reaction force at jaws 1, 2, and 3 as a function of the angular location of the cutting tool.

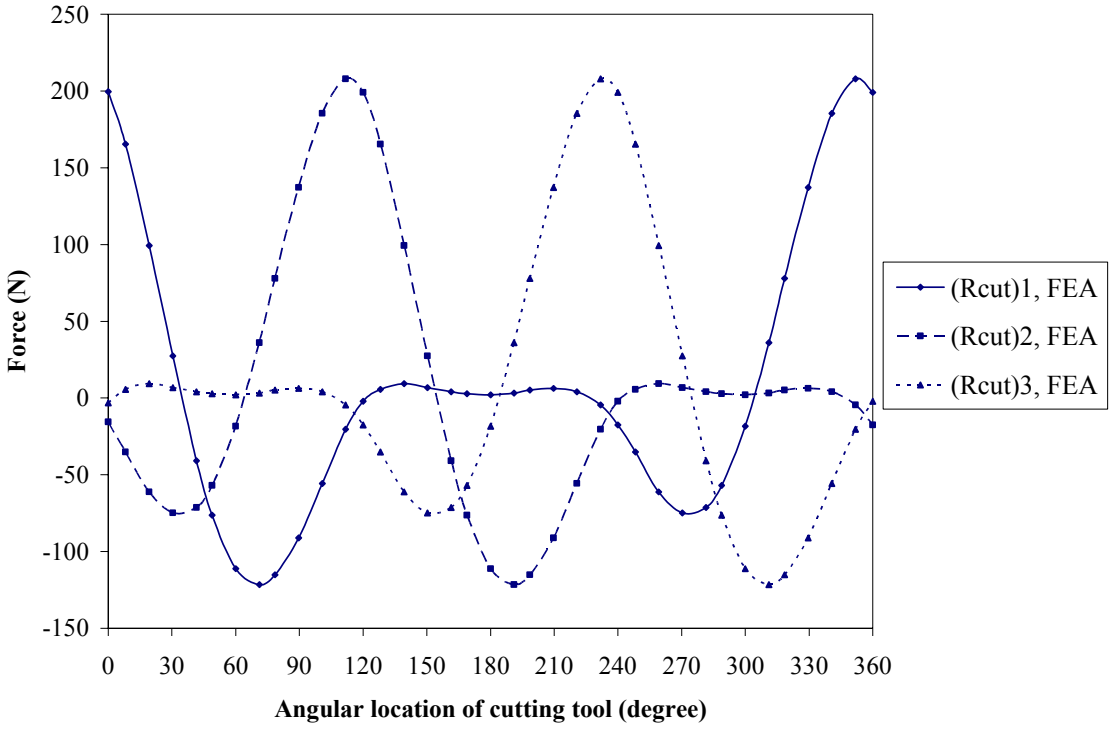

Figure 3.23 Resulting radial reaction force from Finite Element Analysis

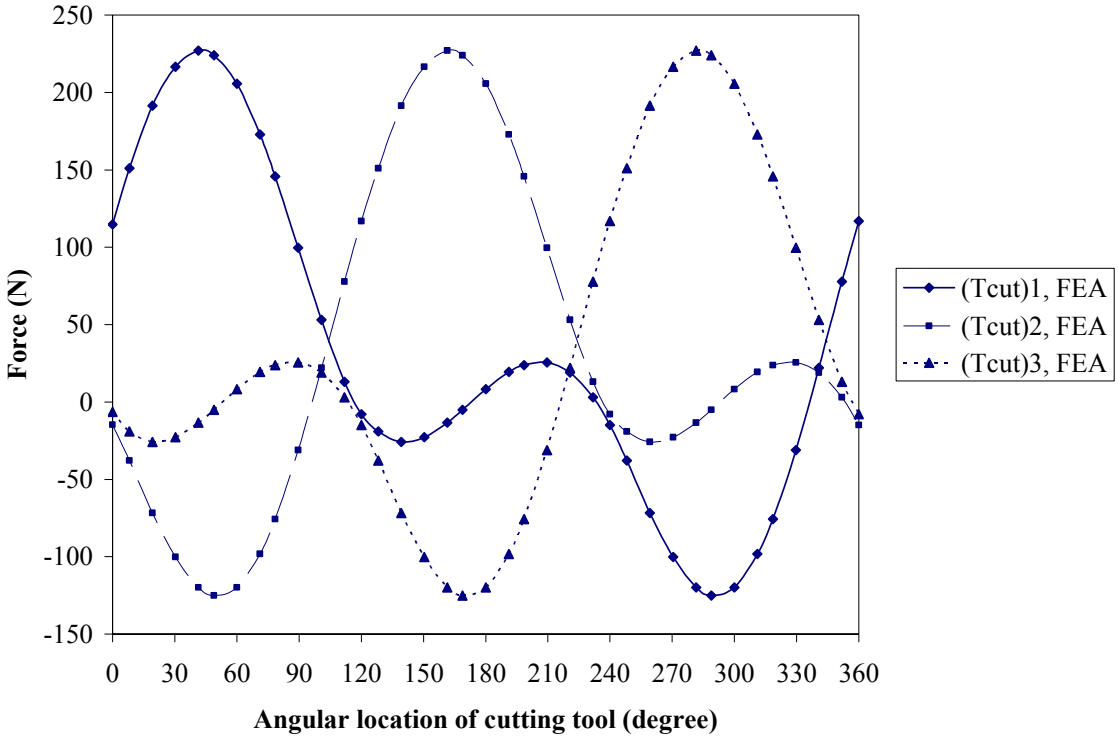

Figure 3.24 Resulting tangential reaction force from Finite Element Analysis

Figure 3.25 and Figure 3.26 show predictive abilities of the theoretical and finite element models. In general, the models appear to predict the reaction forces reasonably closely. The shape of the reaction force plots predicted by the finite element model is similar to the results predicted by the theoretical model. One of the factors that may contribute to the discrepancies between the two models is the inability of the theoretical model to include the compliance of the jaws. In addition, the theoretical model also ignores the compliance of the workpiece and the jaws around the contact area.

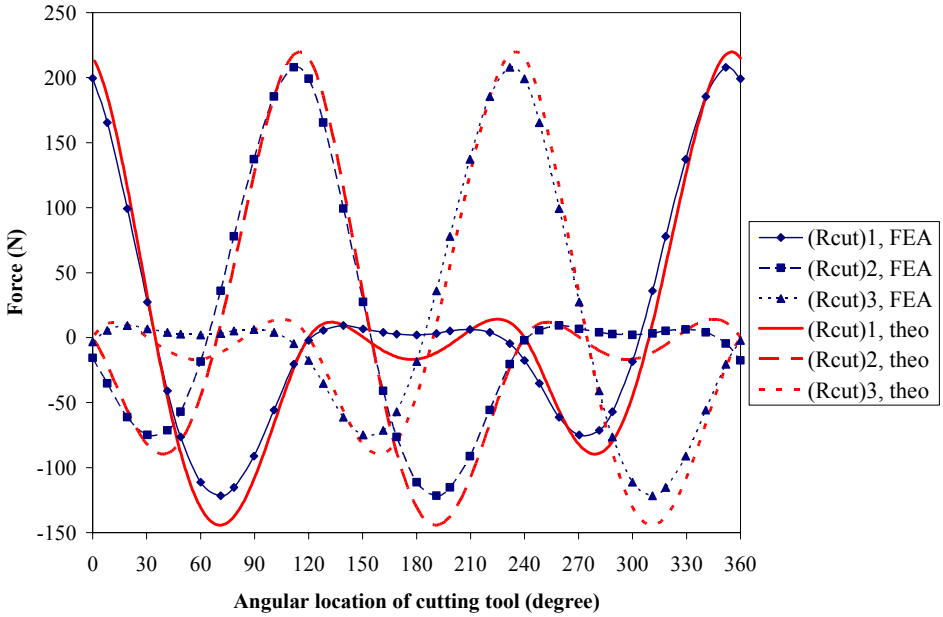

Figure 3.25 Radial reaction forces obtained from the FEA and theoretical model

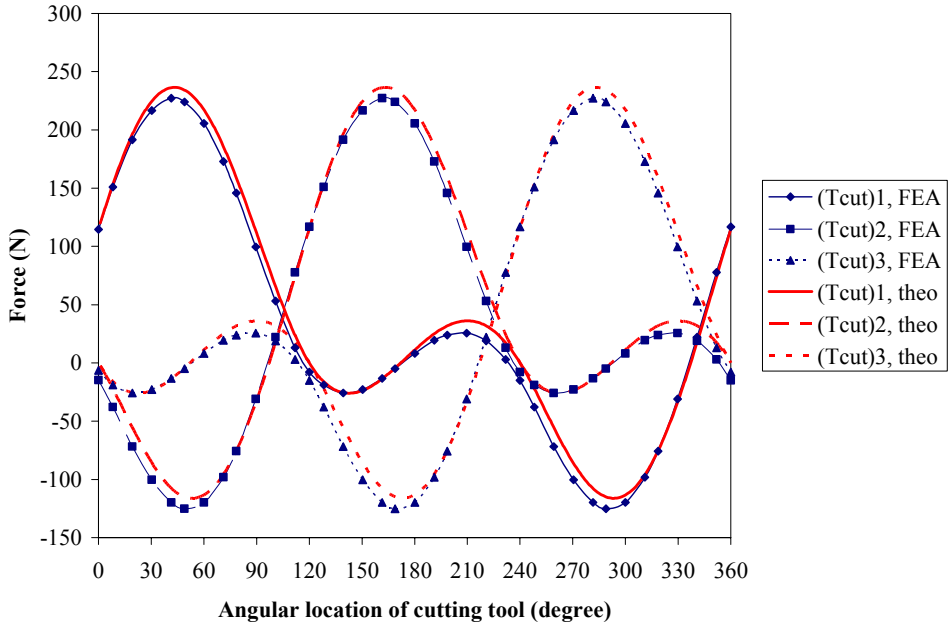

Figure 3.26 Tangential reaction forces obtained from the FEA and theoretical model

3.3 Summary

In this chapter, a theoretical model was developed to predict the finished cut profile of the ring and the reaction forces induced at the jaws during the application of the cutting force. The model was illustrated with an example of a ring held in a three jaw chuck.

In addition, a Finite Element Model was developed to predict the finished cut profile of the ring and the reaction forces induced at the jaws, similar to machining a thin ring clamped in a three jaw chuck. A mesh convergence study was conducted to determine the optimum resolution of elements for the problem. As with the theoretical model, the Finite Element Model was demonstrated for a ring with the same dimensions, properties and applied forces.

In general, the finite element and the theoretical model prediction of the deformation are reasonably close. The finite element model predicts the overall peak-to-valley roundness error to be 27.7 μm while the theoretical model predicts the overall preak-to-valley roundness error of 27.4 μm. Similarly, the shape of the reaction force plots predicted by finite element model is consistent with the results predicted by the theoretical model. Discrepancies between the two models are due to the inability of the theoretical model to include the stiffness of the jaws and also the contact compliances of the workpiece and the jaws around the contact area.

CHAPTER 4

FINISHED CUT PREDICTION VERIFICATION

In an effort to validate the finished cut profile predicted by the theoretical model, this chapter presents the results of an experimental study. Here, the rings were clamped in the chuck and cut using a cutting insert. Three different cutting conditions were selected in this experiment. Finally, the rings were released from the chuck and the profile of the inner diameter of the rings was measured on a roundness machine. The primary goal of this chapter is to show how well the theoretical model is able to predict the finished cut profile of the ring in the turning process.

4.1 Preparation of the Chuck

Throughout the experimental work presented in this thesis, a Hardinge 15.24 cm draw bar power chuck (SCA 2000 306-825H) with medium height soft jaws (SC 2000023-S) was used. This chuck actuates by means of a draw bar, which is moved along the spindle axis to cause the chuck jaws to move inward. When the power chuck is

mounted on the spindle of the Hardinge CNC machine, the draw bar is pulled by hydraulic actuator whose pressure can be adjusted at the back of the CNC machine.

For this study, the soft jaw served to clamp on the ring shaped workpiece and also on a Pratt Burnerd grip force meter (1009-06490), which was needed to measure the clamping force during spin test. To accurately measure the clamping force exerted by the chuck jaws on the ring, a three axis load cell (Kistler 9251AQ) was constrained between a steel flat and the flat surface of the soft jaw. The soft jaws were machined identically using a milling machine to a dimension specified in the appendix. The jaws were machined such that they are half-way through their travel when clamping the workpiece. This ensured adequate closing travel to fully deform the workpiece. This feature size was necessary to allow clamping of a workpiece with an outer diameter of 2.90 mm using stainless steel contacts of thickness 10 mm in between the load cell and the ring. However, since there was only one sensor available, the clamping force measurement was limited to one jaw at a time. While one sensor with stainless steel contacts of thickness 10 mm was placed in one jaw, at the other two jaws a thicker stainless steel contact of thickness 12.7 mm was used in between the soft jaws and the ring. Figure 4.1 shows this arrangement.

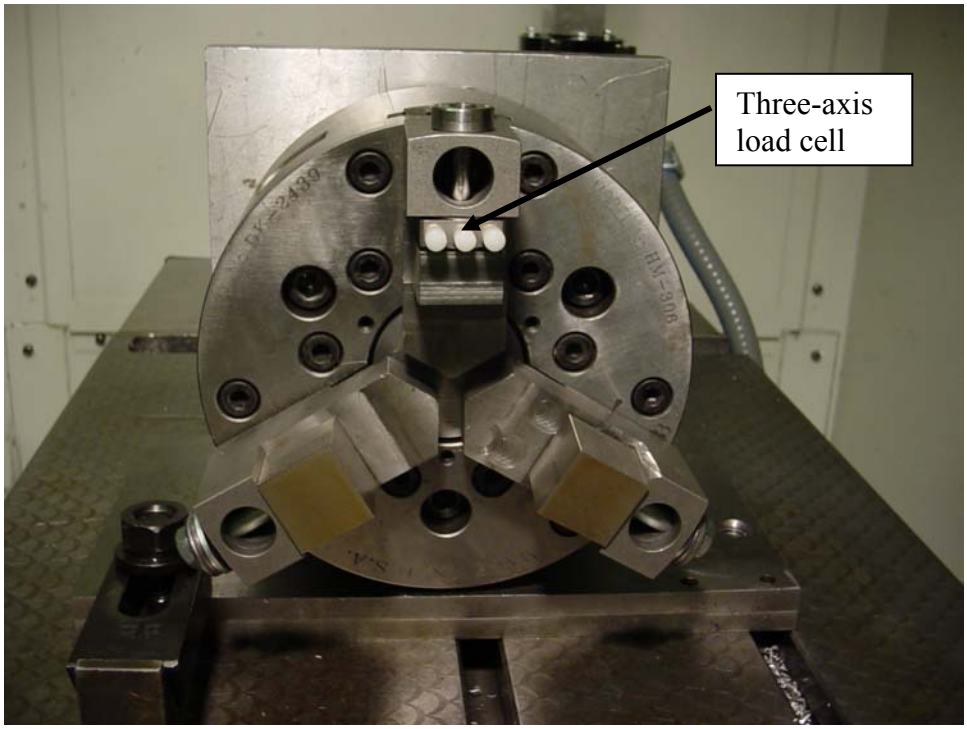

Figure 4.1 Picture of chuck with soft jaws and a three-axis load cell

An extra feature of a circular clamping surface was machined into the soft jaws. while gripping a ring. The ring allowed it to be clamped perfectly to maintain the jaws half way through their travel. Figure 4.2 shows a setup to cut the extra feature of the soft jaw.

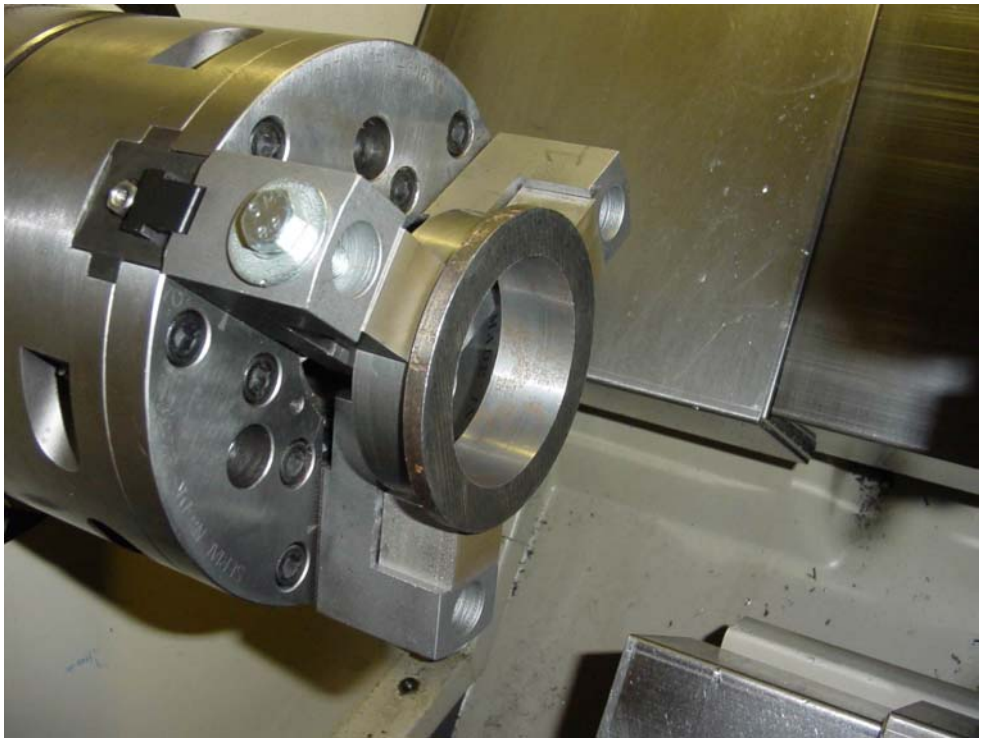

Figure 4.2 Preparation to cut the extra feature

The soft jaws were machined to a diameter of 60 mm bored all the way through the jaws. This feature was used to grip the Pratt Burnerd grip force meter, which is a cylinder 60 mm in diameter. A picture of the cut extra feature is shown in Figure 4.3. The form of the jaws was complete after this final machining.

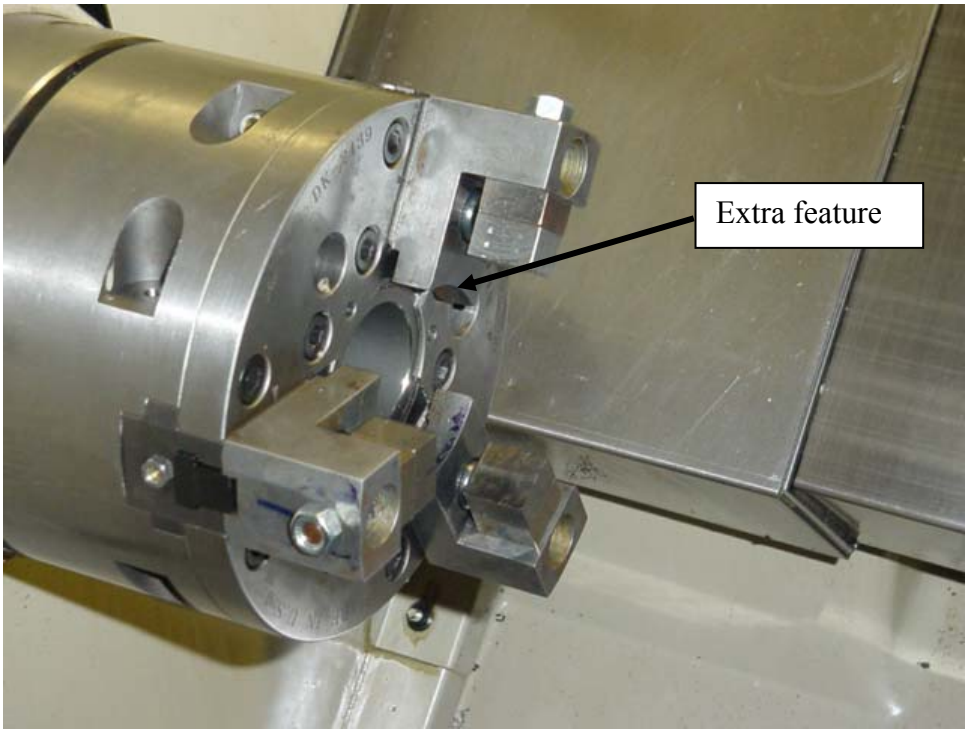

Figure 4.3 Picture of the extra feature cut

4.2 Static Measurement of Clamping Force

A data acquisition system (National Instruments) was used to obtain the signals from the piezoelectric load cell. However, first the clamping force at each jaw was measured one at a time. Before measuring the gripping force, the magnitude of the force applied by the chuck's draw bar, the pressure was adjusted to ensure the gripping force was in a suitable range. Since the models in Chapter 3 were verified with loads ranging from 2000 to 3000 N, the draw bar pressure was adjusted to allow the gripping force to be in this range. The draw bar pressure was kept constant at 75 psi to serve this purpose.

A picture of the piezoelectric load cell measuring the clamping force at jaw 1 is shown in Figure 4.4.

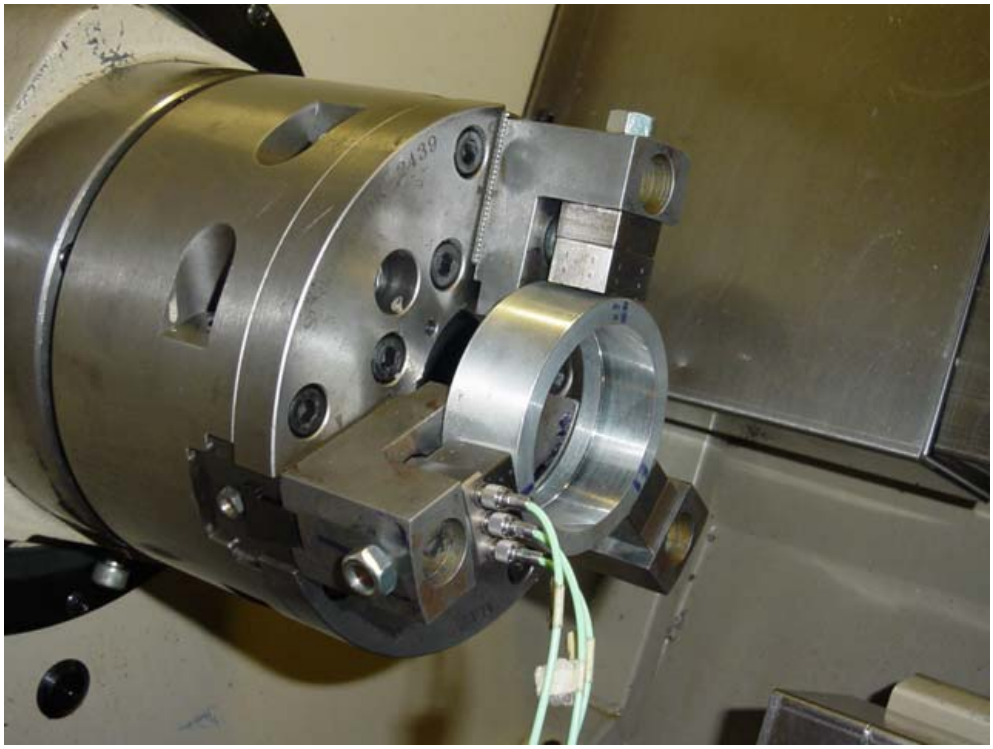

Figure 4.4 Picture of the piezoelectric load cell measuring clamping force at jaw 1

The gripping force of each jaw was measured several times to determine the uncertainty associated with the measurement. In this study, the clamping force was measured for jaws 1, 2, 3, and then back to jaw 1 and this was repeated five times. Using this method, the variation due to moving the force sensor from one jaw to the next jaw could be observed. The measured clamping force results at each jaw are shown in Table 4-1.

Table 4-1 Measured gripping force

Jaw	Clamping Force (N)						
	Rep1	Rep 2	Rep 3	Rep 4	Rep 5	Avg	Std Dev
1	2503	2520	2490	2525	2506	2509	12.5
2	2645	2608	2601	2640	2627	2624	17.5
3	2304	2322	2300	2275	2286	2297	17.9

It may be observed from the last column in Table 4-1 that the variation of the clamping force at each jaw is small compared to its magnitude. Consequently, it may be concluded that moving the force sensor from one jaw to another jaw does not significantly influence the measured force value at a particular jaw.

4.3 Spin Test

A dynamic test was conducted to measure the impact of centrifugal force on the measured gripping force. The piezoelectric load cell could not be used during the dynamic test due to a limitation that the electrical signals from the load cell are transmitted via cables. Therefore, a Part Burnerd grip force meter was used for the dynamic test.

The meter is composed of two units. One unit has a cylindrical end and is gripped in the chuck jaws. The second unit is stationary and reports the grip force reading on an LCD readout. The grip meter is only capable of measuring the clamping force to 0.1 kN accuracy. A picture of the cylindrical unit in the chuck and the stationary unit mounted on the tailstock of the chuck is shown in Figure 4.5. In this arrangement, the gripping unit

sends an optical signal to the stationary unit so that the gripping force is measurable while the chuck is rotating.

Figure 4.5 Spin test using the Pratt Burnerd grip force meter

The cylindrical section of the grip meter has a sensitive region denoted by an indented mark for measuring the grip force. By orienting the grip meter with this sensitive area pointed directly into the jaws, the force exerted by each jaw was measured uniquely. For each jaw, the grip force meter was clamped as shown in Figure 4.5 and the spindle was driven to a speed of 1000 rpm because in the finished cut experimental validation study, the cutting conditions required the chuck to rotate at 1000 rpm.

The force exerted by jaw 1 was measured first. The rotational speed of the chuck was increased by adjusting the speed knob on the CNC panel. At approximately 550 rpm,

the display on the LCD readout started flickering to a value of 0.1 kN less than the reading taken when the chuck was at a complete stop.

Since the grip meter only displays force to the closest 0.1 kN, the actual clamping loss was not necessarily 100 N. However, since there was no grip meter with better resolution available, for the sake of this experiment, it is assumed that the loss of clamping force was 100 N at 550 rpm. The rotational speed was increased further to find the rotational speed of the chuck when the loss in clamping force reached 200 N and 300 N. The loss of clamping force at each jaw was measured several times to determine the uncertainty associated with the measurement. Figure 4.6 depicts the rotational speed for each jaw with varying clamping loss.

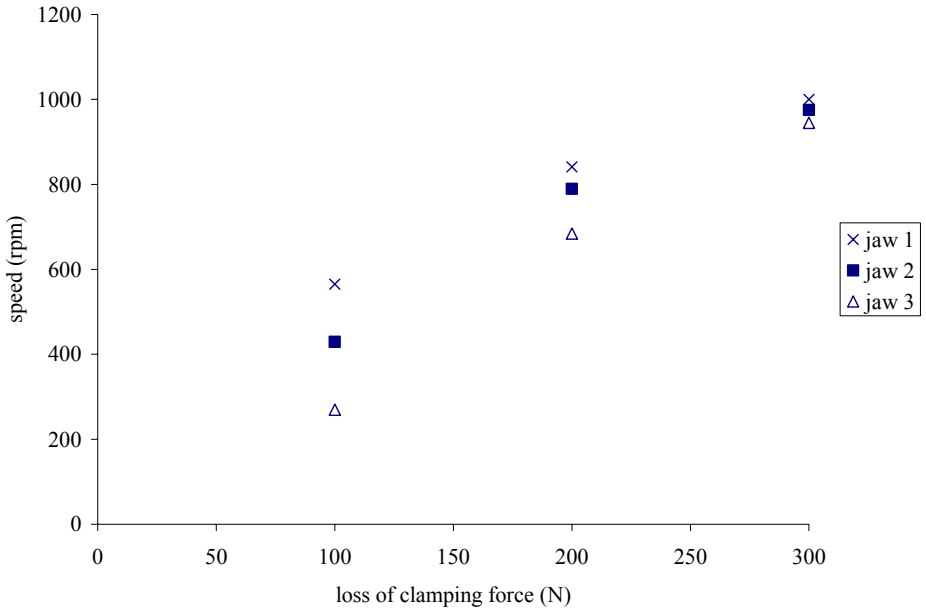

Figure 4.6 Results from spin test

In Figure 4.6, it can be seen that at a higher clamping loss, the spread of the rotational speed for jaws 1, 2, and 3 is small compared to the spread at a lower value of clamping loss. In the experimental validation study in this thesis, the averaged value of rotational speed at jaws 1, 2, and 3 (973 rpm) is used and the clamping loss at this rotational speed is assumed to be 300 N.

4.4 Measurement of Cutting Force

To include the effect of cutting force in the finished cut profile of the ring, the cutting forces for selected cutting conditions were measured. Because the measurement of the cutting forces using a cutting force dynamometer in conjunction with the boring bar is very difficult, the cutting forces were measured separately from the cutting of the workpieces by performing an external cut using a conventional external tool holder.

When measuring the cutting forces for an internal cut with an external cut, the tool geometries of the two cuts should be kept the same so that similar cutting forces are produced. A tool holder (DCLNR-124-B) was selected to match the tool geometry of the boring bar (A16-DCLNR). Both the boring bar and the external tool holder use the same insert (CNMA-432) and hence the cutting geometry was identical for both cutting configurations.

A Kistler cutting force dynamometer (9257B) was used to measure the cutting forces. The tool holder was mounted on the outer face of the dynamometer using a steel bracket with six hexagonal head screws that screw into the top plate of the dynamometer. This dynamometer was mounted on the turret of the CNC lathe. A data acquisition

system (National Instruments) was used to obtain the three signals via a 3 channel Kistler charge amplifier.

The same ring material (Aluminum alloy 6061) used in the internal cut was used for the measurement of the cutting forces. This ring was held by clamping the inner diameter of the workpiece using a Bison scroll chuck (3215-10-5), as shown in Figure 4.7. For the experimental validation study, three different sets of cutting parameters were selected.

Table 4-2 Cutting conditions for model validation

Set #	**Cutting condition**		
	Speed (m/min)	**Depth of cut (mm)**	**Feed (mm/rev)**
1	700	0.005	0.005
2	700	0.01	0.0075
3	700	0.02	0.01

The three cutting parameters were selected to provide various values of cutting forces, especially in the radial direction. A cut length of 19.05 mm was used, which provided sufficient clearance to prevent contact with the jaws and was long enough for the cutting force to stabilize.

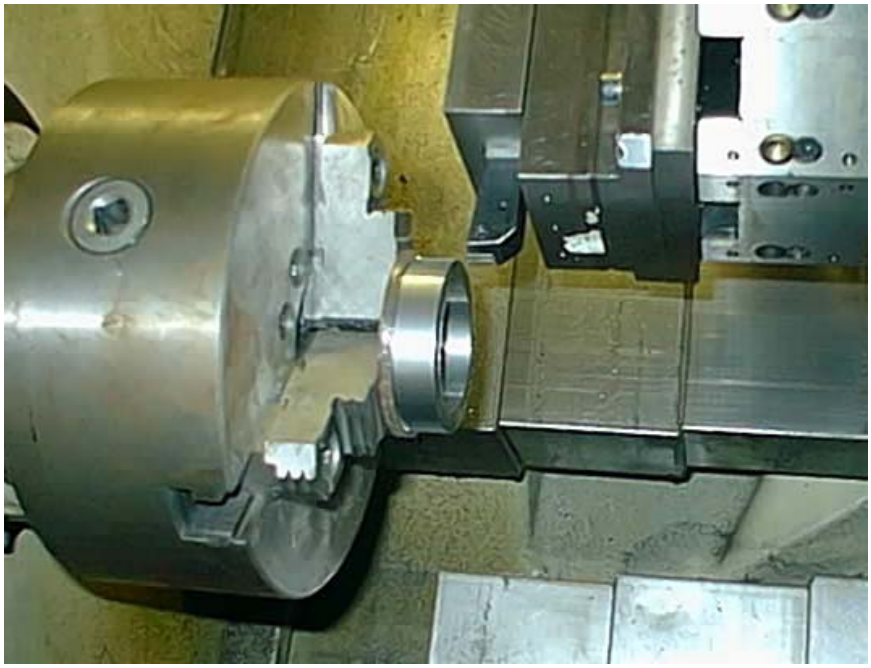

Figure 4.7 Measuring cutting forces by OD turning

Three replications for each set of cutting parameters were performed. Tables 4-3 – 4-5 show the measured cutting forces in the external cuts for the three sets of cutting parameters. The average values were used in determining the impact of cutting force on the deformation of the ring.

Table 4-3 Measured cutting force for cutting condition #1

Trial	F_t (N)	F_r (N)	F_a (N)
1	31	33	10
2	30	31	10
3	33	34	11
Average	31	33	10

Table 4-4 Measured cutting force for cutting condition #2

Trial	F_t (N)	F_r (N)	F_a (N)
1	68	57	25
2	67	56	25
3	68	56	25
Average	67	56	25

Table 4-5 Measured cutting force for cutting condition #3

Trial	F_t (N)	F_r (N)	F_a (N)
1	143	87	63
2	143	86	57
3	144	86	63
Average	143	86	61

Before the rings were cut with depth of cuts specified in Table 4-2, the rings were first "cleaned" until the entire surfaces were clean. These cleaning passes helped to remove the initial out-of-roundness that was present in the rings due to clamping force induced deformation. These passes assured that during the real cuts, the cutting tool was fully engaged with the ring and consequently, the assumption of constant cutting force was valid.

4.4.1 Machining of Rings

Nine aluminum (alloy 6061) rings were prepared for experimental validation of the finished cut profile of the ring internal diameter. To distinguish between the different rings, they were labeled 1 through 9. In addition to these labels, the rings were also marked radially on their bore in 120 degree increments. One index was selected as the

zero degree reference. For each trial, the rings were placed with the 0, 120, 240 degree indices aligned with the contact at jaws 1, 2, and 3, respectively.

First, a cleaning cut of the inner diameter was performed to remove initial out-of-roundness that was present in the rings due to clamping force. Next, the rings were clamped in the chuck and machined using the cutting parameters described in Table 4-2 (three rings for each set). Using the parameters described in Table 4-2, the second cut produced the previously measured cutting forces. Approximately 6.35 mm of the bore width was uncut to prevent the cutting tool from contacting the jaw.

A hand caliper of 0.0254 mm resolution was used to inspect the dimensions of the ring before and after cutting. The dimensions are shown in Table 4-6 - Table 4-8.

Table 4-6 Dimension of rings cut using cutting condition #1

Trial	**Ring 1**	**Ring 2**	**Ring 3**	**Average**
Outer diameter (mm)	36.77	36.79	36.78	36.78
Inner diameter before second cut (mm)	29.41	29.41	29.41	29.41
Inner diameter after second cut (mm)	29.54	29.54	29.54	29.54
Entire width (mm)	12.75	12.73	12.74	12.74

Table 4-7 Dimension of rings cut using cutting condition #2

Trial	**Ring 4**	**Ring 5**	**Ring 6**	**Average**
Outer diameter (mm)	36.83	36.80	36.78	36.80
Inner diameter before second cut (mm)	29.41	29.41	29.41	29.41
Inner diameter after second cut (mm)	29.67	29.67	29.67	29.67
Entire width (mm)	12.75	12.70	12.73	12.73

Table 4-8 Dimension of rings cut using cutting condition #3

Trial	Ring 7	Ring 8	Ring 9	Average
Outer diameter (mm)	36.79	36.78	36.79	36.79
Inner diameter before second cut (mm)	29.41	29.41	29.41	29.41
Inner diameter after second cut (mm)	29.92	29.92	29.92	29.92
Entire width (mm)	12.50	12.51	12.70	12.57

4.4.2 Cut Profile Measurement

After cutting, the finished cut profile of the ring internal diameter was inspected using a roundness machine. Figure 4.8 shows a cut ring sitting on a roundness machine (Taylor-Hobson Talyrond 200). First, the probe was placed such that it barely touched the bore of the ring. Next, the bore of the ring was centered so that the whole profile was within the measurement range of the probe. This was performed by adjusting the knob for each axis in order to minimize the difference in radial measurement taken 180 degrees apart along each axis.

After centering, measurements were performed by selecting the desired analysis items. Note that, while the turntable rotates automatically (counterclockwise), the probe takes measurements of the specimen. The total number of radial inspections per revolution (3750 inspections/rev) and selection of the filter (50 UPR) have to be predetermined before pressing the start key. The purpose of having a filter is to remove noise. The noise may come from vibration in the cutting process and or from the roundness machine. Measurements were taken at half of the width of the ring starting at the zero degree angular mark; the inspections were made in a counter clockwise direction.

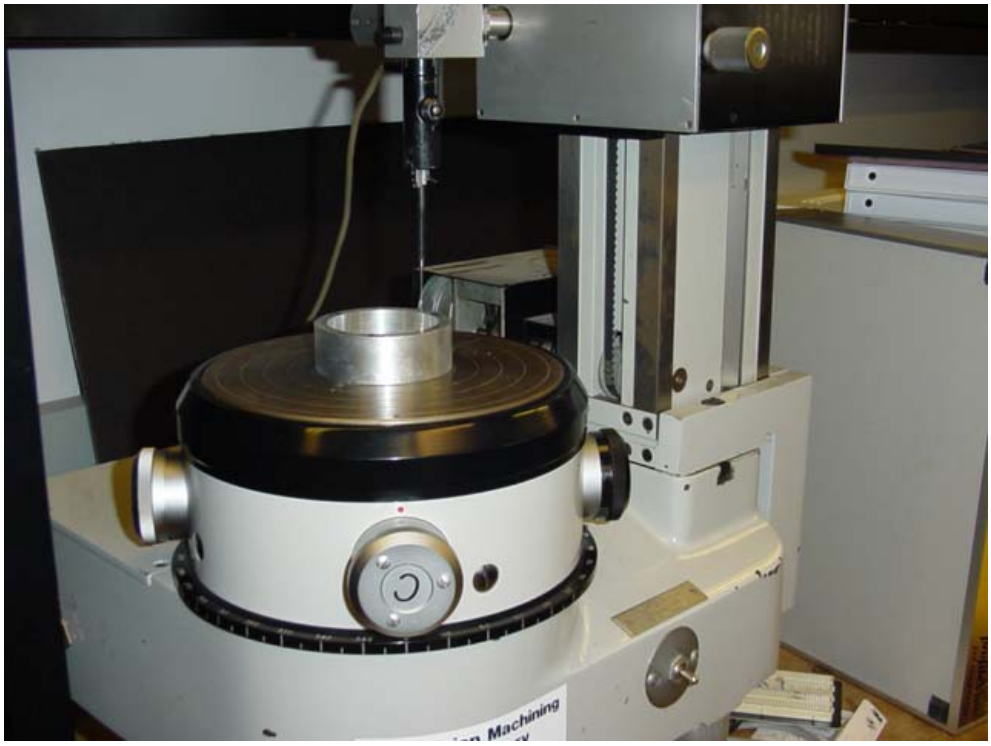

Figure 4.8 Measurement of cut ring bore using a roundness machine

Figure 4.9 shows the average measured profile of the cut ring for three different cutting conditions. Referring to Figure 4.9, although the rings were clamped with the same amount of clamping force, the averaged measured profiles of the rings are different for each cutting condition. At angular locations of 0°, 120°, and 240°, the largest average measured profile deviation belongs to the ring cut at cutting condition #3, followed by the ring cut at cutting condition #2 and cutting condition #1, respectively. On the other hand, at 60°, 180°, 300°, the average measured profile of the rings cut at cutting condition #3 seems to be the smallest and then the average measured profile of the rings gets larger for cutting conditions #2 and #1, respectively. These behaviors are consistent with the fact that cutting condition #3 has the largest depth of cut, which consequently decreases the

compliance of the workpiece so that it is easier to deform. In addition, cutting condition #3 also produces the largest cutting forces, which causes the roundness error of the ring to increase.

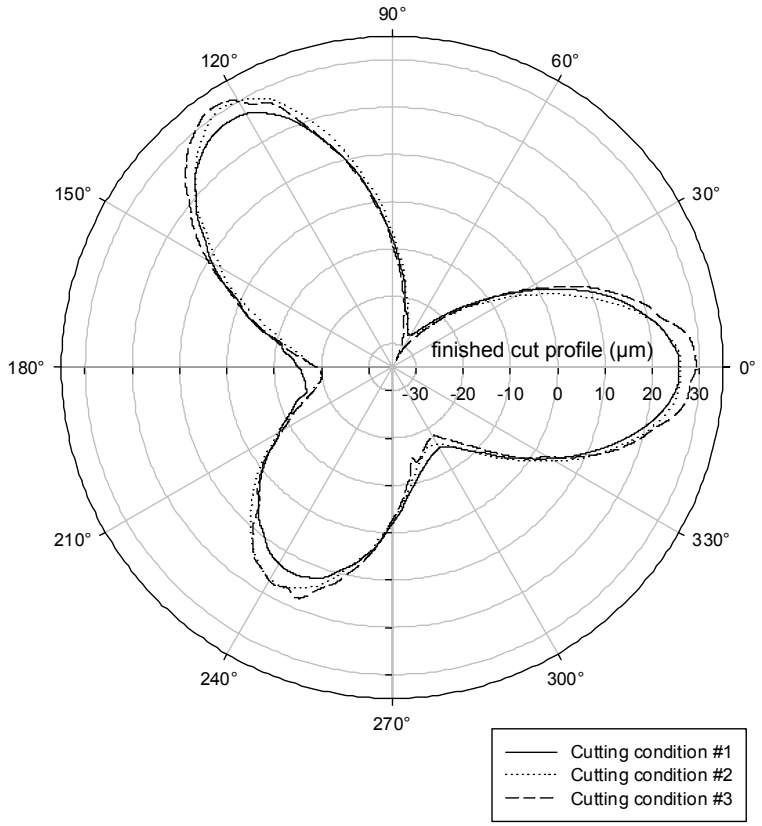

Figure 4.9 Plot of average profile of cut rings using different cutting conditions

4.5 Comparison of Finished Cut Profile with Theoretical Model

As described in the previous chapter, the theoretical model can be used to predict the finished cut profile. The ring material is 6061 aluminum alloy with a Young's Modulus of 69 GPa and a Shear Modulus of 26 GPa. The measured clamping and cutting

forces are used to predict the finished cut profile. A plot of the resulting theoretical prediction and the average measured profile of rings cut using cutting condition #1 are shown in Figure 4.10 along with a numerical comparison in Table 4-9.

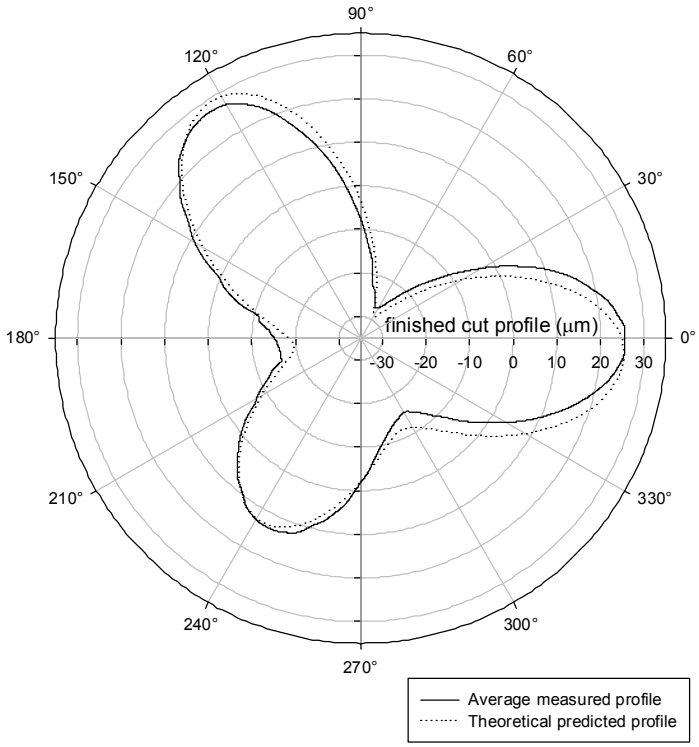

Figure 4.10 Measured and predicted profile of rings cut using cutting condition #1

Table 4-9 Measured and predicted profile of rings cut using cutting condition #1

Angle (degrees)	**Measured average profile (μm)**	**Predicted profile (μm)**	**Percentage difference**
0	24.7	25.2	2.0
60	-26.6	-29.9	12.4
120	27.0	29.7	10.0
180	-16.2	-19.2	18.5
240	12.9	13.2	2.3
300	-14.7	-11.6	-21.1
360	24.7	25.9	4.9
Average absolute percentage error			**10.2**

A plot of the resulting theoretical prediction and the average measured profile for rings cut using cutting condition #2 are shown in Figure 4.11 along with a numerical comparison in Table 4-10.

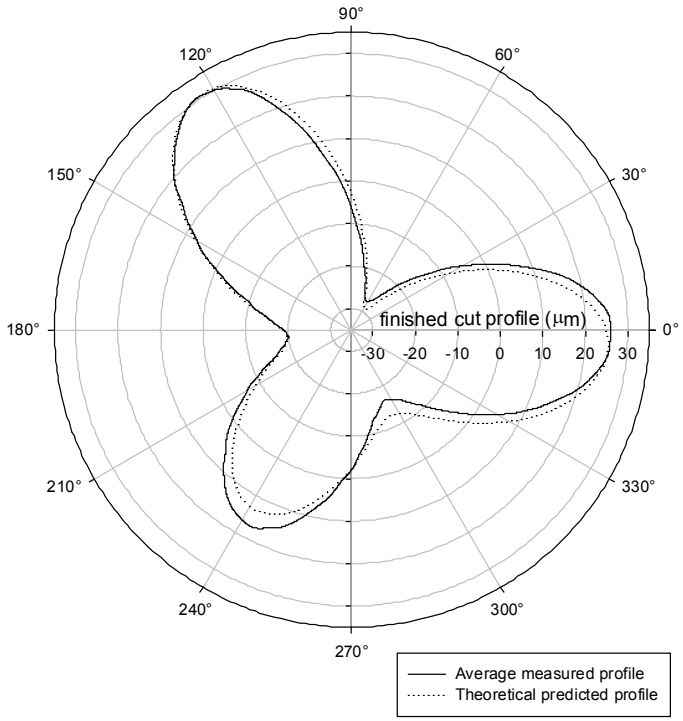

Figure 4.11 Measured and predicted profile of rings cut using cutting condition #2

Table 4-10 Measured and predicted profile of rings cut using cutting condition #2

Angle (degrees)	Measured average profile (µm)	Predicted profile (µm)	Percentage difference
0	23.1	24.4	5.6
60	-27.8	-29.4	5.8
120	28.8	30.5	5.9
180	-17.5	-18.6	6.3
240	12.3	13	5.7
300	-11.6	-12.3	6.0
360	23.7	25.1	5.9
Average absolute percentage error			**5.9**

A plot of the resulting theoretical prediction and average measured profile for rings cut using cutting condition #3 are shown in Figure 4.12 along with a numerical comparison in Table 4-11.

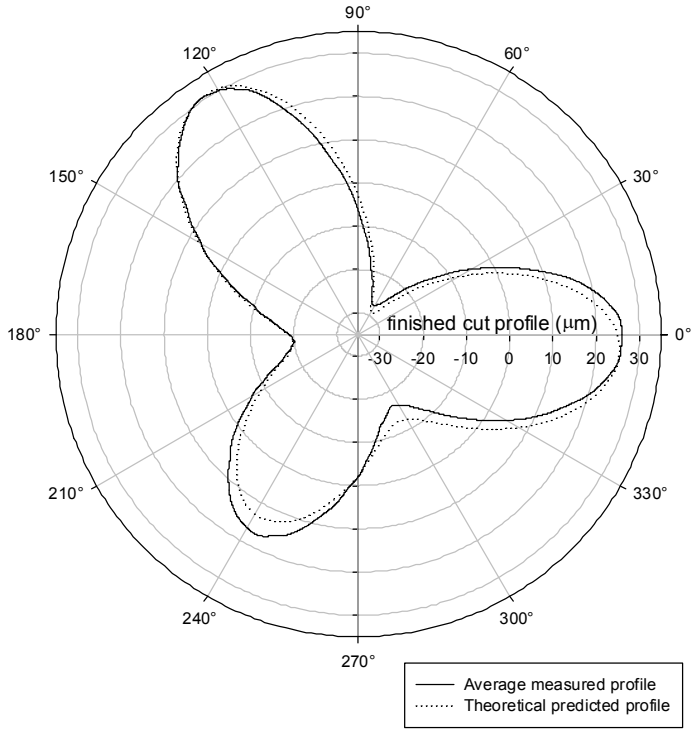

Figure 4.12 Measured and predicted profile of rings cut using cutting condition #3

Table 4-11 Measured and predicted profile of rings cut using cutting condition #3

Angle (degrees)	Measured average profile (µm)	Predicted Profile (µm)	Percentage difference
0	29.2	27.4	-6.2
60	-31.3	-32	2.2
120	30.6	31.7	3.6
180	-19.9	-20.6	3.5
240	17.1	14.5	-15.2
300	-17.9	-12.1	-32.4
360	29.2	28.2	-3.4
Average absolute percentage error			**9.5**

Referring to Tables 4-9 – 4-11, the average absolute percentage error for cutting conditions #1, #2, and #3 are 10.2 %, 5.9 %, and 9.5 %, respectively. The overall mean absolute percentage error for all conditions is 8.5%. To obtain the predicted profiles shown in Tables 4-9 – 4-11, the average of the inner diameters of the uncut and cut ring were assumed to be the inner diameter in the theoretical model.

For comparison, Table 4-12 shows the predicted ring roundness profiles at the extreme points by assuming the inner diameter of the cut ring as the inner diameter in the theoretical model. The table also shows the percentage error of the predicted profile when compared with the average measured profile.

Table 4-12 Predicted profile of rings cut using finished dimensions.

	Cutting condition #1		**Cutting condition #2**		**Cutting condition #3**	
Angle (degrees)	**Predicted profile (µm)**	**Percentage difference**	**Predicted profile (µm)**	**Percentage difference**	**Predicted profile (µm)**	**Percentage difference**
0	24.4	-1.2	25.9	12.1	31.8	8.9
60	-29	9.0	-31.2	12.2	-36.1	15.3
120	29	7.4	32.3	12.2	34.1	11.4
180	-18.6	14.8	-19.7	12.6	-23.8	19.6
240	12.8	-0.8	13.8	12.2	16.8	-1.8
300	-11.4	-22.4	-13	12.1	-12.3	-31.3
360	25.1	1.6	26.7	12.7	32.7	12.0
Average absolute percentage error		**8.2**		**12.3**		**14.3**

Referring to Table 4-12, it appears that the prediction using the finished ring dimensions deviate more from the measured profile than the predictions in Tables 4-9 – 4-11. Since errors in Table 4-12 are larger in magnitude, it is concluded that more

accurate predictions can be arrived upon with the theoretical model using the average of the inner diameters of uncut ring and the cut ring as the inner diameter.

4.6 Summary

In this chapter, nine rings were turned using three different cutting conditions in a three jaw chuck. The jaws of the chuck were specially modified to allow accurate measurement of the clamping force. After turning, the profile of the cut surface was inspected to determine the finished cut profile of the rings. The profile from three workpieces for each cutting condition were averaged and compared with predictions based on the theoretical model in Chapter 3.

A prediction incorporating the chucking and cutting forces predicts the turned surface of the ring cut using cutting condition #1 within 21.1 % at the extreme points for a ring clamped in the three-jaw chuck. The model predicts the turned surface of the ring cut using cutting condition #2 and cutting condition #3 within 6.3 % and 32.4 %, respectively. The average absolute percentage errors for cutting condition #1, #2, and #3 at the extreme points are 10.2 %, 5.9 %, and 9.5 %. The overall mean absolute percentage error for all conditions is 8.5%. For comparison, the theoretical model prediction using the inner diameter of the cut ring as the inner diameter yielded a mean absolute percentage error of 22.1% over all three cutting conditions.

CHAPTER 5

OPTIMIZATION MODEL

From the previous two chapters, it is obvious that the workholding parameters such as the number of jaws and chucking force are known to influence the roundness of ring shaped parts. Experimental trial and error methods are often used in practice to optimize the workholding parameters to achieve the desired part quality. This chapter presents a systematic mathematical approach for optimizing these parameters using the theoretical model of ring deformation and a model for predicting the reaction force.

The optimization approach takes as input the required roundness tolerance, geometry and mechanical properties of the ring, cutting forces, and the coefficient of friction between the jaws and the ring. The output consists of the minimum number of jaws and the range of acceptable chucking forces that ensures the required tolerance while preventing slip of the ring. Simulation examples illustrate the use of the proposed workholding optimization approach for a turning application. In addition, based on the optimization model, this chapter proposes a novel concept of dynamic chucking that promises to yield part roundness that is superior to that obtained via conventional constant force chucking.

5.1 Conventional Chucking Optimization

In order to achieve the required roundness tolerance, operators typically use a conventional chuck with a large number of jaws, which provides increased rigidity. However, the cost and complexity of the chuck increases with the number of jaws. Another parameter that can be manipulated to reduce part distortion is the clamping force. However, there is a trade-off between the optimal chucking force and part stability in the chuck. A large chucking force results in excessive elastic deformation of the ring leading to large roundness errors whereas a small chucking force cannot adequately restrain the workpiece during machining. Therefore, this requires the determination of the optimal combination of the number of jaws and clamping force at each jaw location that keeps the part from slipping and at the same time produces roundness error that is within the allowable limit.

5.1.1 Model Development

In Chapter 3, for a specific number of jaws, it was shown that the radius of the finished inner surface of the ring, r_{in}^{fin}, as a function of the tool tip location γ after clamping, cutting, and unclamping is given by Equation 3.31:

$$r_{in}^{fin}(\gamma) = r_{in}^{init} + d_{nom} + \delta_{total}(\gamma)$$

$$\delta_{total}(\gamma) = -y_{cut}(\gamma) - y_{cl}(\gamma)$$

Solving the second equation for angular positions from 1° to 360°, the overall peak-to-valley roundness error of the ring, Δ_n, is given by Eq 3.32.

$$\Delta_n = \delta_{total}(\gamma)_{\max} - \delta_{total}(\gamma)_{\min}$$

Therefore, the constraint that the roundness error of the cut ring should not exceed the desired geometric tolerance, δ_d, may be stated mathematically as follows:

$$\Delta_n(C_{cl}, F_r, F_t) \leq \delta_d \tag{5.1}$$

The clamping force at each jaw is assumed to be the same and can be represented by C_{cl}. Chapter 3 also presented calculations of the reaction forces (radial and tangential direction) induced at the jaws during cutting. To ensure that the ring does not slip in the chuck during cutting, the following constraint derived from the Coulomb friction law is applied:

$$|(T_{cut})_i| \leq \mu_s (C_{net})_i \tag{5.2}$$

$$(C_{net})_i = C_{cl} + (R_{cut})_i \tag{5.3}$$

where, T_{cut} and R_{cut} are the tangential and reaction forces exerted on the ring due to cutting; μ_s is the coefficient of static friction for the jaw and ring material pair; $(C_{net})_i$ is the net radial clamping force exerted on the ring at angular location of the jaw Φ_i . The index i refers to the i^{th} jaw of the chuck. When the cutting tool is located at angular positions ranging from 0° to 360°, the tangential reaction forces at all jaws are monitored to ensure that they do not violate Coulomb's law of friction.

Each jaw is only capable of exerting a normal force that is directed into the workpiece. Because the force and moment equilibrium equations in Chapter 3 are derived by assuming that the normal clamping forces are positive in the direction shown in Figure

3.2 and 3.3, the clamping forces exerted by the jaws on the workpiece should be greater than zero. A lower bound of 1 N is chosen for the normal force exerted by jaws.

$$1 \le C_{cl}, \quad i = 1...n \tag{5.4}$$

5.1.2 Plastic Deformation

To prevent plastic deformation of the workpiece, the normal forces acting on the ring at the jaw locations have to satisfy the following condition:

$$Q(C_{cl}, F_r, F_t) \le \frac{Sy}{SF} \tag{5.5}$$

where Q is a function that predicts the maximum stress in the workpiece, SF is the design safety factor and Sy is the yield strength of the ring material.

According to Boresi, the effect of the radial stress on a curved beam may be assumed to be small [Boresi 2003]. This assumption is quite accurate for curved beams whose cross sections do not possess thin webs. Therefore, it is necessary to keep only the stress in the circumferential direction below the required limit, as stated in Eq.(5.5). The function Q that predicts the maximum circumferential stress in the workpiece may be obtained from the theory of elasticity for curved beams of rectangular cross section as follows:

$$Q(C_{cl}, F_r, F_t) = |(\sigma_{\theta\theta})_{\max}| \tag{5.6}$$

The mathematical expression of the circumferential stress distribution may be expressed as follows:

$$\sigma_{\theta\theta} = \frac{N_\theta}{A} + \frac{M_\theta \left[A - \tilde{r}(w \ln \frac{r_{out}}{r_{in}}) \right]}{A\tilde{r}(r(w \ln \frac{r_{out}}{r_{in}}) - A)} \tag{5.7}$$

where N_θ is the internal in-plane normal force, M_θ is the internal bending moment at any cross section θ, w is the width of the ring, $\tilde{r}$ is the location at the ring ranging from r_{in} to r_{out}, and A is the cross sectional area of the ring.

5.1.3 Objective Function

For a given number of jaws, two objective functions can be formulated and will be used later in this chapter to find the minimum required clamping force and the maximum allowable clamping force.

1. $Min\ C_{cl}$ (5.8)

   This form of the objective function can be used to obtain the minimum required clamping force that prevents the ring from slipping while satisfying the required roundness tolerance.

2. $Min\ |\Delta_n(C_{cl}, F_r, F_t) - \delta_d|$ (5.9)

   This form of the objective function can be used to determine the clamping forces that result in the closest possible roundness error to the desired roundness tolerance, δ_d.

Figure 5.1 shows an algorithm that predicts the minimum and maximum clamping forces, and the minimum number of jaws for a given ring geometry, material, cutting forces, and desired roundness tolerance. The following section describes the algorithm in detail.

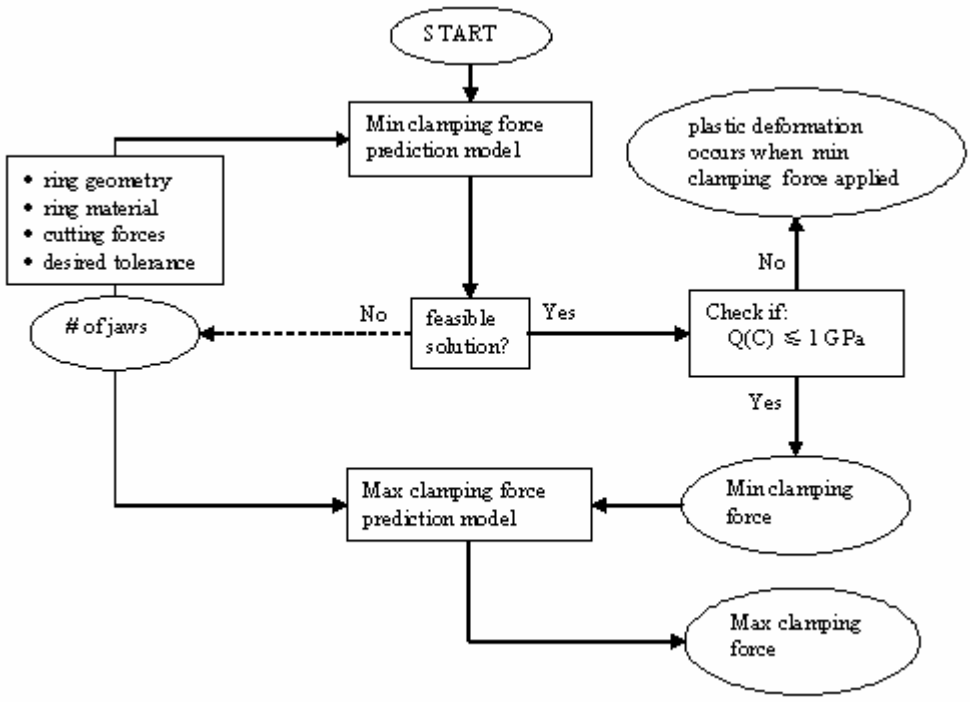

Figure 5.1 Algorithm to find optimal clamping force and number of jaws.

5.1.4 Minimum clamping force prediction model

Using the first objective function from the previous section and constraints (5.1), (5.2) and (5.4), the optimization model to determine the minimum required clamping force may be formulated as follows:

Objective function: $Min\ \ C_{cl}$

Subject to: $\Delta_n(C_{cl}, F_r, F_t) \le \delta_d$

$$|(T_{cut})_i| \leq \mu_s (C_{net})_i, \; i = 1...n$$

$$1 \leq C_{cl}$$

The calculation starts with the number of jaws, n = 3. When it is impossible to obtain a roundness error that is less than the desired tolerance, an infeasible solution for the minimum required clamping force prediction model will result. If this occurs, the optimization model must be solved again for a higher number of jaws, indicated by the dotted line in Figure 5.1. The iterative procedure is continued until the optimization model yields a feasible solution, which corresponds to the minimum required clamping force using the lowest number of jaws n.

After the minimum required clamping force is obtained, the clamping force is substituted into Eq. (5.5) to check if the maximum circumferential stress in the workpiece exceeds the elastic deformation limit. If the maximum stress is less than the elastic deformation limit, the result is valid and the maximum clamping force prediction can proceed.

5.1.5 Maximum clamping force prediction model

The minimum required clamping force from the previous optimization model can be used as the lower bound of the decision variable to guarantee that the workpiece is held without slipping in the chuck. This is expressed mathematically as:

$$C_{\min} \leq C_{cl} \tag{5.10}$$

In addition, to ensure that the maximum clamping force does not cause plastic deformation of the ring, Eq. (5.5) is included as a constraint in the optimization formulation. The optimization model to determine the maximum allowable clamping force is formulated as follows:

Objective function: $Min \ |\Delta_n(C_{cl}, F_r, F_t) - \delta_d|$

Subject to: $C_{\min} \le C_{cl}$

$$Q(C_{cl}, F_r, F_t) \le \frac{Sy}{SF}$$

5.1.6 Example

The following ring properties and cutting forces were used to find the minimum required number of jaws and the range of clamping force that satisfies the desired tolerance and keeps the ring from slipping. The ring material was assumed to AISI 52100 steel.

Table 5-1 Ring properties, cutting forces, and coefficient of friction

Outer Diameter	52.8 mm
Inner Diameter	46.2 mm
Width	25.4 mm
Young Modulus	201.33 GPa
Yield Strength	2 GPa
Shear Modulus	79.2 GPa
Radial Cutting Force	280 N
Tangential Cutting Force	347 N
Coefficient of Friction	0.2

The radial and tangential cutting forces shown in Table 5-1 were measured specifically for cutting speed of 42.6 m/min, feed of 0.076 mm/rev and the depth of cut of 0.406 mm [Malluck 2003]. The values in Table 5-1 are held constant while the desired tolerance of the inner diameter is varied to observe changes in the number of jaws, minimum required and maximum allowable clamping forces, as shown in Table 5-2.

Table 5-2 Optimization results

Run	Smallest Achievable Tolerance (μm)	Desired Tolerance (μm)	Number of jaw	Minimum Required Clamping Force (N)	Maximum Allowable Clamping Force (N)
1	71.9	80	3	2372	2644
2	71.9	75	3	2372	2476
3	71.9	72	3	2372	2374
4		70	Need to use 4 jaw chuck		

For n = 3, the minimum required clamping force is C = 2372 N. For n = 3 the smallest roundness error that can be achieved for the given ring geometry, material and cutting forces is approximately 71.9 μm. Figure 5.2 shows the finished cut profile of the ring obtained using the minimum required clamping force. For a desired tolerance that is less than 71.9 μm, the number of jaws required is greater than three.

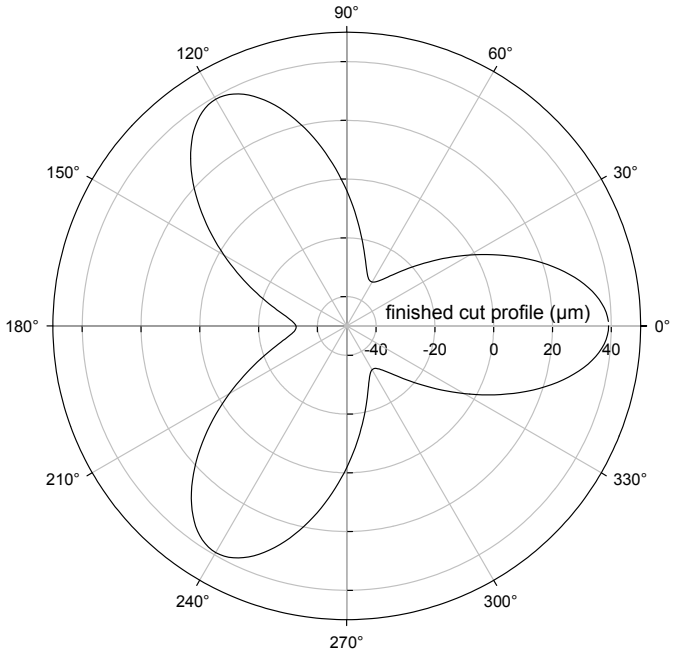

Figure 5.2 Finished cut profile obtained using minimum clamping force

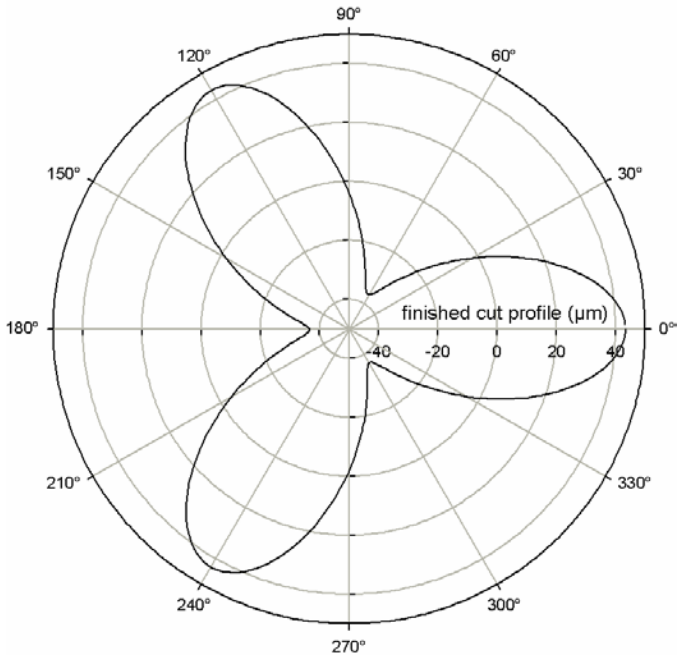

Figure 5.3 Finished cut profile obtained using clamping force when δ_{des} = 80 μm

5.2 Dynamic Chucking Optimization

Results from the previous section show that the number of jaws becomes the main limitation to obtaining the desired roundness tolerance. A more flexible fixturing concept is required to improve the capability of the chuck and thus the accuracy of the machined ring. In present day chucks, clamping forces are generally kept constant during cutting in order to simplify the ease of operation. As described in the previous section, the constant clamping magnitudes are typically derived from the cutting force whose angular location results in the largest reaction force at the jaws. Consequently, there are times during the cut when overclamping is exercised which causes the ring to distort more than necessary. This motivates a novel concept of adaptive chucking where the clamping force at each jaw is allowed to vary provided that the Coulomb friction law is satisfied at all contacts.

Wang et al presented a concept of an intelligent fixturing system for the milling process that allows adaptive adjustment of the clamping forces to achieve minimum deformation of the workpiece according to the cutter position and the cutting forces [Wang 1999]. Based on this concept, Nee et al built a prototype intelligent fixture with dynamic clamps capable of delivering accurate but varying clamping intensity [Nee 2000]. The experiment using the prototype intelligent fixture shows workpiece quality improvement when milling a thin walled workpiece. However, this concept uses rigid body analysis to find the minimum clamping forces required for kinematic restraint of the workpiece. The primary limitation of the rigid body analysis is that it is statically indeterminate when more than three reaction forces are unknown. In addition, the deformation information of the workpiece is analyzed by means of finite element analysis.

A major limitation of this approach is the large model size and computational cost. In this section, a novel concept of adaptive chucking is applied to turning of ring shaped workpieces.

5.2.1 Equal clamping force but varying in magnitude

Based on the above discussion, a concept of adaptive chucking is proposed where the chucking force applied by each jaw is the same but the magnitude is allowed to vary with respect to the angular location of the cutting tool. The magnitude of the chucking force is determined by computing the minimum required clamping force for each angular location of the cutting tool, denoted by j. Thus, the objective function for this concept of chucking can be stated as follows:

$$Min\ (C_{cl})_j,\ j = 1...360 \tag{5.11}$$

Similar to the constant chucking force optimization problem, at an instantaneous angular location of the cutting tool, the magnitude of the net clamping force at jaw 1, jaw 2 and jaw 3 $(C_{net})_{i,j}$ are not equal. These net clamping forces and tangential reactions between each jaw and the ring should be monitored and to ensure that they do not violate Coulomb's friction law for a given angular position of the cutting tool:

$$|(T_{cut})_{i,j}| \leq \mu_s (C_{net})_{i,j}, i = 1...3,\ \ j = 1...360 \tag{5.12}$$

$$(C_{net})_{i,j} = (C_{cl})_j + (R_{cut})_{i,j} \tag{5.13}$$

To ensure that the clamping forces exerted by the jaws are greater than zero, the following constraints are included in the model:

$$1 \le (C_{cl})_j, \; j = 1...360 \tag{5.14}$$

Using the same ring material properties, geometry, friction coefficient, and cutting forces as in the previous example, the optimization is performed for n = 3. Figure 5.4 shows the resulting minimum clamping force. Using this clamping force, Figure 5.5 shows the resulting finished cut profile. The overall peak-to-valley roundness error of the cut ring is found to be 55.4 μm, which is a great improvement over the results obtained in Table 5-1 (71.9 μm) when applying a constant chucking force.

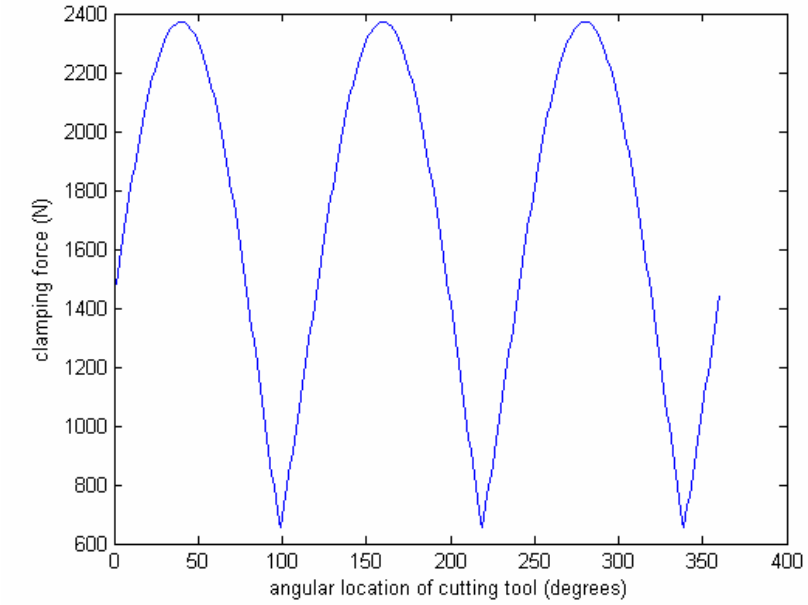

Figure 5.4 Minimum clamping force prediction

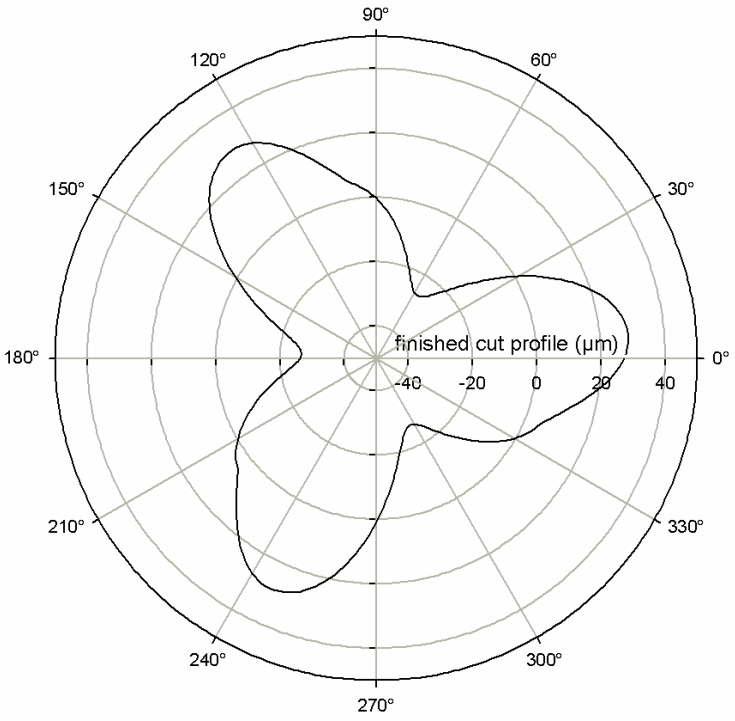

Figure 5.5 Finished cut profile obtained using minimum clamping force

5.2.2 Independently controlled jaw force

In the two previous models, the chucking force at each jaw was constrained to be equal in magnitude. Another dynamic chucking strategy consists of varying the individual jaw forces independently so as to obtain a desired roundness error in the cut ring.

Different from the two chucking strategies previously discussed (assumes a displacement-controlled chuck), this model assumes a force-controlled chuck. Due to the nature of displacement-controlled chuck, it is not possible to control force at each jaw independently by displacing the jaws differently. Displacing the jaws by different amount

only shifts the center of the workpiece but the clamping forces at each jaw tend to be equal and balanced.

In the force-controlled chuck, a closed loop control system is necessary to monitor and control the forces exerted by the jaw at any instantaneous location of the cutting tool. The following figure is the free body diagram of the individually controlled jaw force chuck.

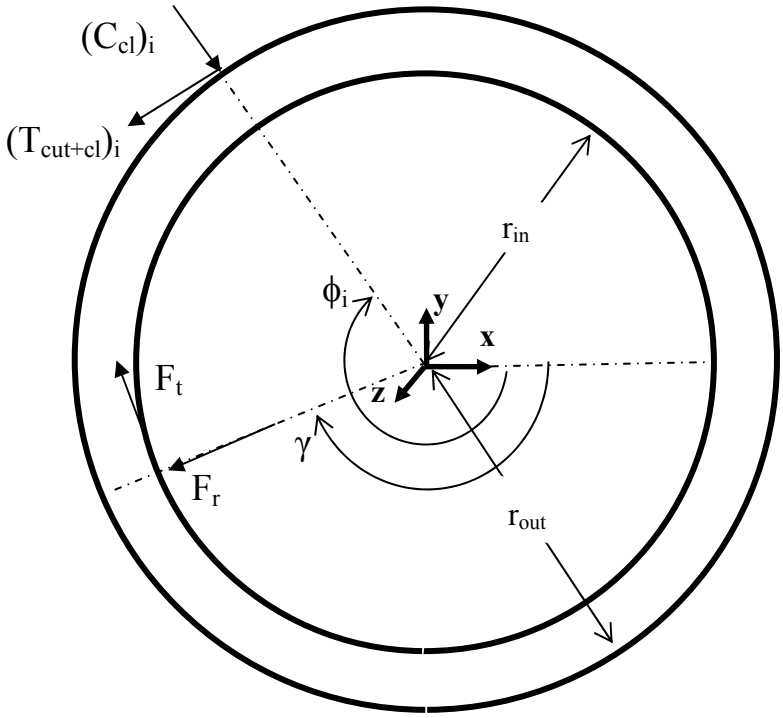

Figure 5.6 Free Body Diagram of the individually controlled jaw force chuck

Note that the clamping forces are controllable and radial reaction forces no longer exist in its free body diagram. When the number of jaws is equal to three, three tangential

reaction forces can be calculated in terms of the applied clamping force and the in-plane cutting forces using force and moment equilibrium equations as follows:

$$\sum F_x = \sum_{i=1}^{n} (C_{cl})_i \sin\phi_i + \sum_{i=1}^{n} (T_{cut+cl})_i \cos\phi_i - F_r \sin\gamma - F_t \cos\gamma = 0 \tag{5.15}$$

$$\sum F_y = \sum_{i=1}^{n} (C_{cl})_i \cos\phi_i - \sum_{i=1}^{n} (T_{cut+cl})_i \sin\phi_i - F_r \cos\gamma + F_t \sin\gamma = 0 \tag{5.16}$$

$$\sum M_z = F_t r_{in} - \sum_{i=1}^{n} (T_{cut+cl})_i r_{out} = 0 \tag{5.17}$$

However, when the number of jaws is greater than three, the reaction forces cannot be obtained using Eqs. (5.15) – (5.17) alone because the problem is statically indeterminate. The additional equations (in addition to the equations of static equilibrium) required to determine the additional unknowns (the redundant reactions) in the statically indeterminate problem may be obtained by applying Castigliano's theorem for deflections. This theorem states that:

$$\frac{\partial U}{\partial (T_{cut+cl})_i} = 0 \tag{5.18}$$

where the denominator $(T_{cut+cl})_i$ refers to the redundant force whose index $i = 4 \ldots n$ and U refers to the strain energy of the deformed ring.

Due to the complicated nature of this problem, both in theory and in practical implementation, the dynamic clamping model has been developed and solved only for the $n = 3$ (three jaws) case assuming that the clamps are placed symmetrically around the ring.

In this third optimization model, there is more than one decision variable to be optimized. They are $(C_{cl})_1$, $(C_{cl})_2$, and $(C_{cl})_3$. As a result, the equation that describes the relationship between the clamping force and the deformation of the ring is non-linear. In this case, a set of the smallest magnitude of clamping forces, $(C_{cl})_1$, $(C_{cl})_2$, and $(C_{cl})_3$ does not necessarily imply smaller deformation at the point of cutting. Ideally, the objective function should be to minimize the deformation at each machining point, which consequently gives zero roundness error. Although mathematically achievable, it is not possible to have zero roundness error in real manufacturing situations. Typically, some desired roundness tolerance is assigned to the workpiece.

A proposed solution for this problem is to limit the minimum and maximum error contributed by the cutting force and clamping force at each machining point by introducing an inequality constraint in the optimization model as follows:

$$\delta_{lower} < \delta(\gamma) < \delta_{upper}$$

$$\delta_{lower} < \left(- y_{cut}(F_r, F_t, \gamma) - y_{cl}(C_{1,j}, C_{2,j}, C_{3,j}, F_r, F_t, \gamma)\right) < \delta_{upper} \tag{5.19}$$

where δ_{lower} and δ_{upper} are the lower and upper bounds of the allowable range of the error due to the cutting force and unclamping effect at each machining point. This constraint is chosen because the overall roundness error of the cut ring is derived from the middle term in Eq. (5.19), as shown in Chapter 3. In addition, to ensure that the ring does not slip in the chuck during cutting and the clamping forces exerted by the jaws are greater than zero, the following constraints are included in the model:

$$|(T_{cut+cl})_{i,j}| \le \mu_s C_{i,j}, \; i = 1...3, \; j = 1...360 \tag{5.20}$$

$$1 \le C_{i,j}\,,\ i = 1...3,\ \ j = 1...360 \tag{5.21}$$

where the index i refers to the i^{th} jaw, while the index j refers to the angular of the tool increment as the workpiece rotates from 1° to 360° during one complete revolution.

Given the practical problem in implementing a continually varying chucking force system, the objective function needs to be framed in such a way as to simplify the control system that will physically vary the chucking forces. The control system can be simplified if the variation in chucking force from one step to the next is minimized. Accordingly, the objective function is framed as follows:

$$Min\ \sqrt{\sum_{i=1}^{3}(C_{i,j} - C_{i,j-1})^2} \tag{5.22}$$

Thus, the objective function minimizes the squared sum of the difference between the current chucking force applied by the i^{th} jaw $C_{i,j}$ and the chucking force applied by the same jaw at the previous time instant $C_{i,j-1}$. Due to non-linearity introduced by the first constraint, the outputs of the model are highly influenced by the initial guess. Therefore, the starting solutions, $C_{1,0}$, $C_{2,0}$, and $C_{3,0}$ need to be determined prior to solving the model.

For consistency, ring material properties, geometry, friction coefficient, and cutting forces in the previous example are used again in this section. In addition, the upper and lower bounds of the allowable range are set to -25 μm and 25 μm, respectively. An initial run of the model showed that the variation of clamping forces $C_{i,j}$ was not periodic with a period of 2π. This means that value of clamping force, say, at tool location of 0°, $C_{1,0}$ is not the same as that at 360°, $C_{1,360}$. This can be seen in Figure 5.7

and Figure 5.8 which shows the chucking force variation of the three jaws with angular position of the cutting tool for two different sets of initial guesses. This can introduce a problem for the control system, which now suddenly has to jump from one value to another at the end of one complete revolution. This non-periodicity is due to the dependence of the optimization on the initial starting solution. To avoid this dependence on the initial point and to get a consistent solution an iterative solution methodology was adopted.

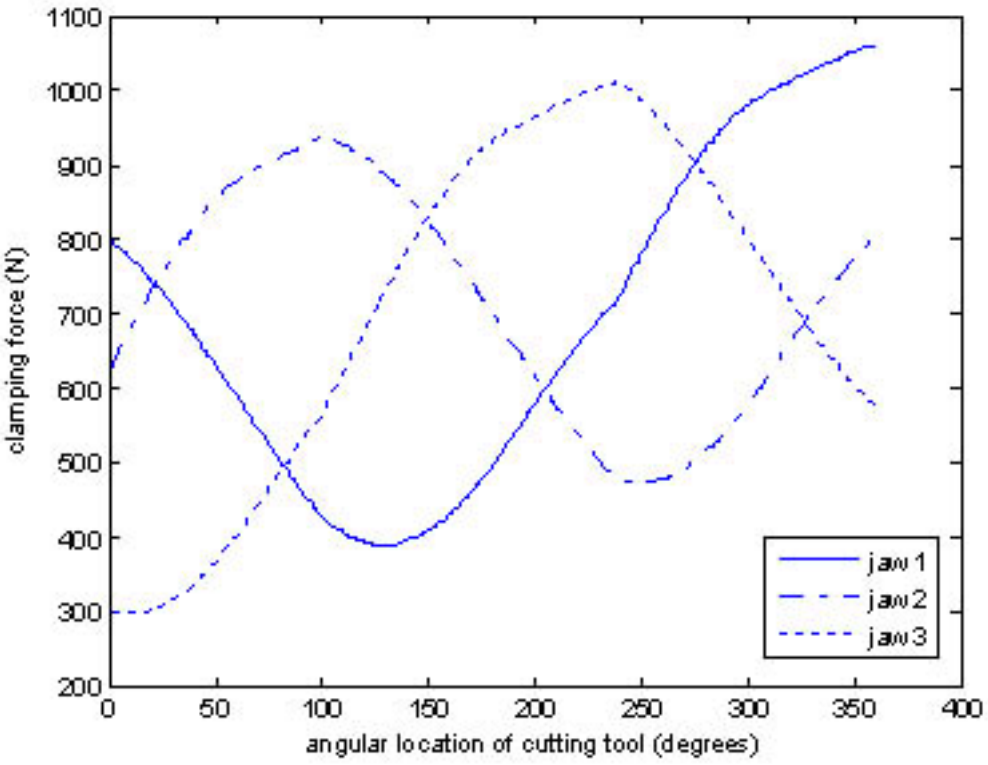

Figure 5.7 Solutions with initial starting point of [500,500,500] N

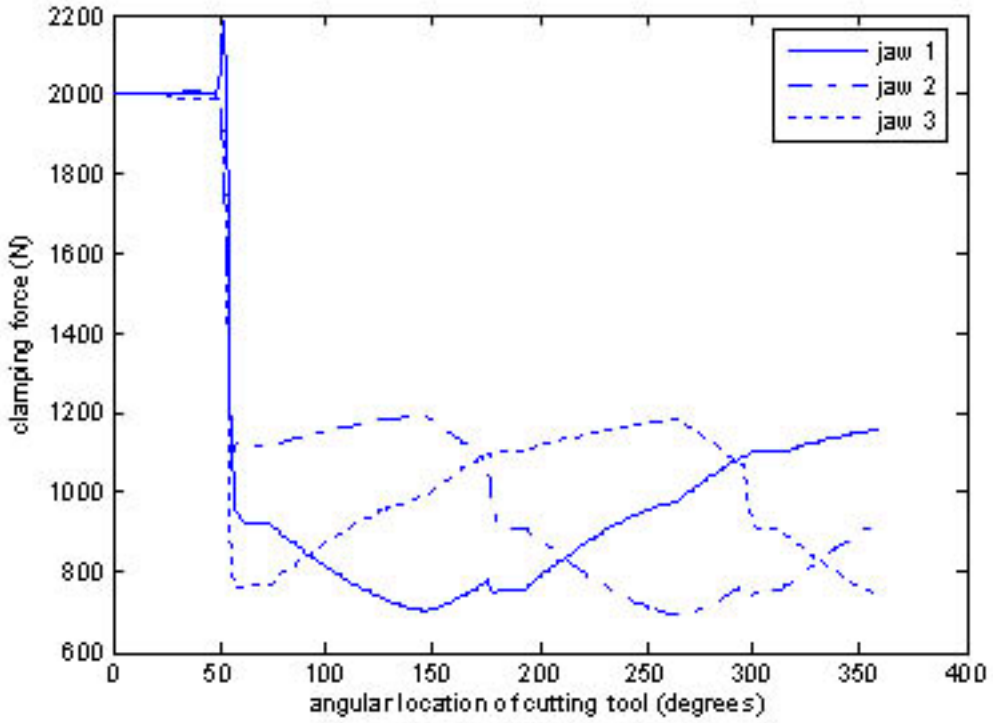

Figure 5.8 Solutions with initial starting point of [2000, 2000, 2000] N

In the iterative method, the chucking solution at $\gamma = 360^{o}$ is stored and is used as the starting solution for one more run of the optimization model. In other words, the optimization is performed again with the optimized solution of the previous run of the model as the initial guess. The first optimization is executed with an arbitrarily chosen starting solution of [500, 500, 500] N. The convergence of the iterations is shown in Figure 5.9.

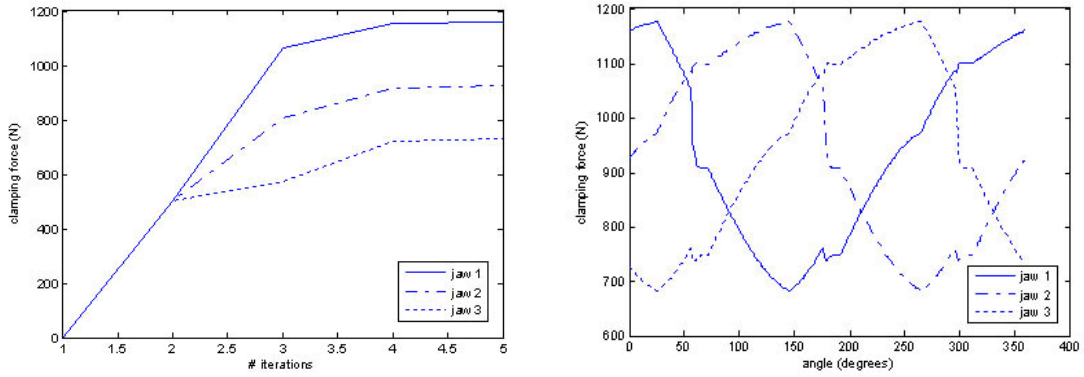

(a) Convergence of clamping force **(b) Final converged clamping force variation**

Figure 5.9 Iterative methodology with starting point [500, 500, 500] N

Figure 5.9(a) shows the convergence of the clamping force for all three clamps at the starting position of 0°. This converged value is C_0 = [1160, 925, 729] N. Notice in Figure 5.9(b) that the chucking force variations with angle are now periodic. Hence, the dependence on the initial guess has been reduced. It remains to be seen if the arbitrary starting solution for the first run of the optimizer has any effect on the converged value. To check this, the iterative method was again executed with an arbitrary starting guess of [2000, 2000, 2000] N. The results of this run are given in Figure 5.10. The converged starting position chucking force value is C_0 = [1161, 926, 730] N. It is clear that the arbitrary starting solution of the iterative method does not seem to affect the final solution.

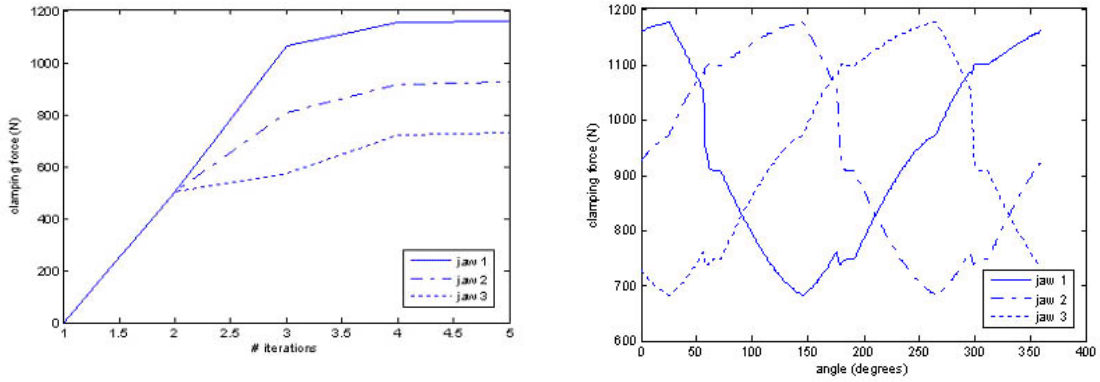

(a) Convergence of clamping force **(b) Final converged clamping force variation**

Figure 5.10 Iterative methodology with starting point [2000, 2000, 2000] N

When the upper and lower limit of the allowable range of the error contributed by the cutting force and unclamping effect at each machining point δ_{lower} and δ_{upper} are set to a value that is large (for example -50 and 50 μm), the optimization models yields clamping forces that are equal at jaw 1, 2, and 3 and constant for the entire angular location of the cutting force. The following figures shows the final converged clamping force variation and the resulting finished cut profile when δ_{lower} and δ_{upp} are set to -50 μm and 50 μm, respectively, and $\mu_s = 0.2$.

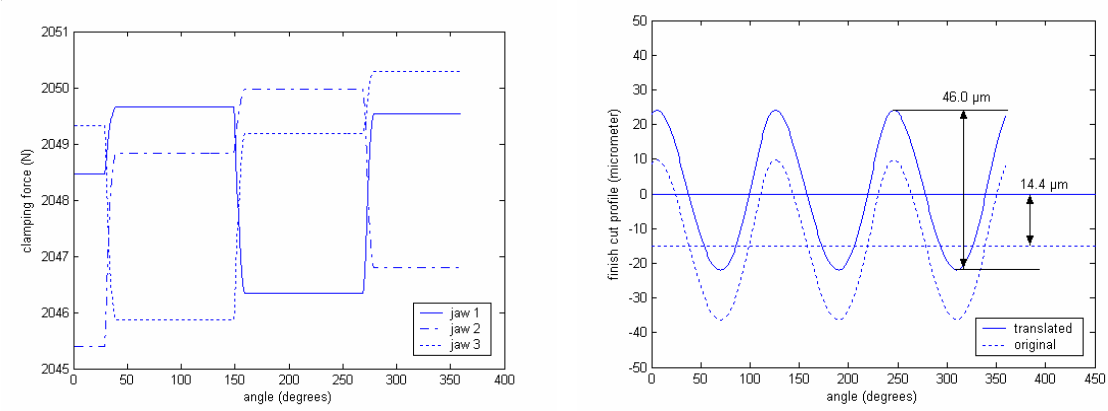

(a) Final converged clamping force variation **(b) Finished cut profile**

Figure 5.11 Results with -50 µm< δ <50 µm and μ_s = 0.2

As can be seen from Figure 5.11(a), the clamping force at jaw 1, 2, and 3 is approximately at 2047 N. The calculated peak-to-valley roundness error is 46 µm.

Figure 5.11(b) shows the overall deflection finished ring inner profile (indicated by dashed line). Computing the least square deviation of this dashed line (given by Eq. (3.31) for $0 \leq \gamma \leq 360°$, the profile of the finished cut ring after unclamping is obtained (indicated by solid line).

5.2.2.1 Sensitivity Analysis of Friction Coefficient

Friction is an important factor in workholding. All of the above analyses have been performed with a static friction coefficient μ_s = 0.2. The friction coefficient can be easily affected by surface finish and texture and also with wear of the clamps during prolonged use on the shop floor. In order to understand the impact of the friction coefficient on the optimization solution, the iterative optimization methodology was

executed with a friction coefficient μ_s = 0.15 and 0.3. The upper and lower limit of the allowable range of the error contributed by the cutting force and unclamping effect at each machining point δ_{lower} and δ_{upper} are imposed at -50 and 50 µm, respectively. The results of this run are shown in Figure 5.11 and Figure 5.12. As can be seen, for μ_s = 0.15 the resulting clamping force is approximately 2727 N, a solution different from that for μ_s = 0.2. As expected, lowering the friction coefficient has increased the clamping force to provide a better grip. As a result of higher clamping force, the peak-to-valley roundness error of the cut ring increases to 66.1 µm.

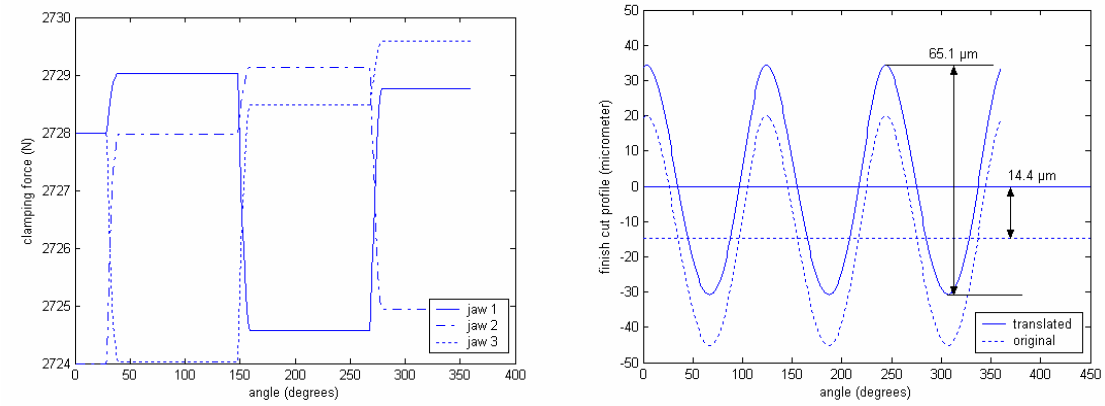

(a) Final converged clamping force variation **(b) Finished cut profile**

Figure 5.12 Results with -50 µm< δ <50 µm and μ_s = 0.15

A consistent results may also be observed when running the optimization model at a higher coefficient of friction μ_s = 0.3. The resulting clamping force (approximately 1367 N) is lower than at μ_s = 0.2 and the peak-to-valley roundness error (29 µm) is lower than at μ_s = 0.2. Figure 5.13 shows the observation when running the optimization using μ_s = 0.3.

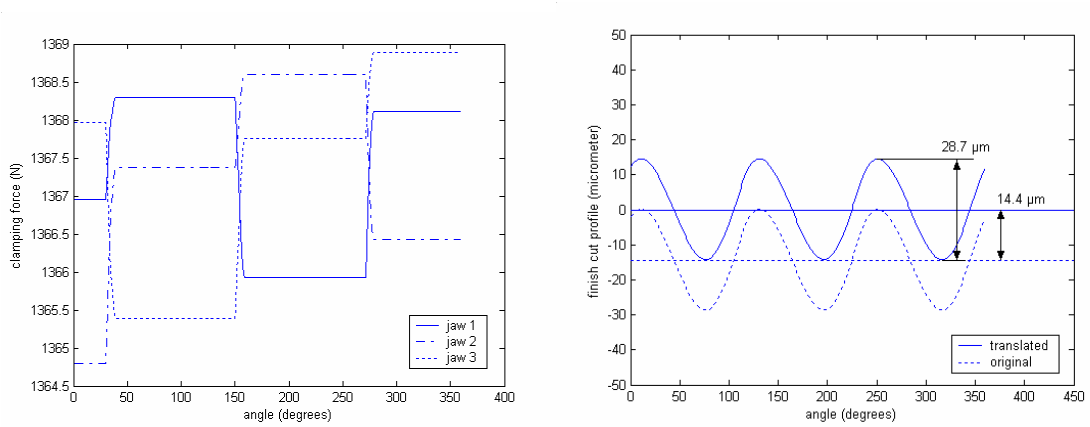

(a) Final converged clamping force variation **(b) Finished cut profile**

Figure 5.13 Results with -50 µm< δ <50 µm and μ_s = 0.30

5.2.2.2 Sensitivity Analysis of δ_{lower} and δ_{upper}

In the first two strategies discussed in this chapter, the optimization models were run to find the minimum clamping force that automatically yields the smallest possible roundness error. However, in the independently controlled chucking force optimization model, minimum clamping forces do not necessarily imply smallest possible peak-to-valley roundness error. As an alternative solution, the resulting roundness error is described by the lower and upper limit variables such as δ_{lower} and δ_{upper}. In this section, these two variables are studied to find the smallest peak-to-valley roundness error achievable in the independently controlled chucking force strategy.

Besides the peak-to-valley roundness error, the average of the total ring deflection due to cutting and unclamping effect $\overline{\delta_{total}(\gamma)}$ also needs to be considered. The following mathematical equations, derived from Eq. 3.31, depict the physical meaning of $\overline{\delta_{total}(\gamma)}$:

$$\delta_{total}(\gamma) = r_{in}^{fin}(\gamma) - r_{in}^{init} - d_{nom}$$

$$\overline{\delta_{total}(\gamma)} = \overline{r_{in}^{fin}(\gamma)} - \left[r_{in}^{init} + d_{nom}\right] \tag{5.23}$$

In other words, $\overline{\delta_{total}(\gamma)}$ is the difference between the average radius of the finished inner surface of the ring and the desired radius of the finished inner surface of the ring. The term inside the square brackets is the desired radius of the finished inner surface of the ring. Ideally, the actual and the desired radii of the finished inner surface are expected to be equal. However, due to cutting and unclamping of the ring, some discrepancy may occur and the amount of error may be obtained by calculating $\overline{\delta_{total}(\gamma)}$. Derived from Eq 3.31 $\overline{\delta_{total}(\gamma)}$ may be obtained from the following mathematical expression:

$$\overline{\delta_{total}(\gamma)} = \frac{1}{360}\sum_{\gamma=1^o}^{360^o}\left(-y_{cut}(\gamma) - y_{cl}(\gamma)\right) \tag{5.24}$$

For consistency, ring material properties, geometry, friction coefficient (μ_s = 0.2), and cutting forces in Table 5-1 are assumed in this section. The discussion starts by setting δ_{lower} and δ_{upper} to large values. In Figure 5.10, it was found that when the δ_{lower} and δ_{upper} are set to -50 and 50 μm respectively, the optimization models yields a clamping force which are equal at jaw 1, 2, and 3 and constant for all angular locations

of the cutting force. This suggests that a single constant value of clamping force at jaw 1, 2 , and 3 satisfies the constraint in Eq. (5.19) whose δ_{lower} and δ_{upper} equals -50 and 50 μm, respectively. The resulting peak-to-valley roundness error is 46 μm while the minimum profile is at -36.3 μm and maximum profile is at 9.7 μm measured from the initial inner radius, as shown in Figure 5.11. In addition, $\overline{\delta_{total}(\gamma)}$ is found to be -14.4 μm.

To improve the peak-to-valley roundness error of the ring, realistically δ_{lower} needs to be increased and δ_{upper} needs to be decreased. However, to study the effect of δ_{lower} and δ_{upper} independently on the peak-to-valley roundness error and $\overline{\delta_{total}(\gamma)}$, first δ_{lower} is increased while δ_{upper} is set at a constant value of 50 μm. The following table shows the result.

Table 5-3 Results from increasing δ_{lower} and δ_{upper} = 50 μm

No	δ_{upper} (μm)	δ_{lower} (μm)	$\delta_{total}(\gamma)_{\max}$ (μm)	$\delta_{total}(\gamma)_{\min}$ (μm)	$\overline{\delta_{total}(\gamma)}$ (μm)	Δ_3 (μm)
1	50	-50	9.7	-36.3	-14.4	46.0
2	50	-40	9.7	-36.3	-14.4	46.0
3	50	-35	9.2	-35	-14.1	44.2
4	50	-30	10.9	-30	-11.2	40.9
5	50	-28	13.3	-28	-8.5	41.3
6	50	-25	18.4	-25	-8.3	43.4
7	50	-20	NO SOLUTION			

where Δ_3 is the peak-to-valley roundness error using three jaw chuck. On the second set of trials, the δ_{upper} is decreased and δ_{lower} is set at a constant value of -50 μm. The results are shown in Table 5-4.

Table 5-4 Results from decreasing δ_{upper} and δ_{lower} = 50 μm

No	δ_{upper} (μm)	δ_{lower} (μm)	$\delta_{total}(\gamma)_{\max}$ (μm)	$\delta_{total}(\gamma)_{\min}$ (μm)	$\overline{\delta_{total}(\gamma)}$ (μm)	Δ_3 (μm)
1	50	-50	9.7	-36.3	-14.4	46.0
2	40	-50	9.7	-36.3	-14.4	46.0
3	30	-50	9.7	-36.3	-14.4	46.0
5	20	-50	9.7	-36.3	-14.4	46.0
6	10	-50	9.7	-36.3	-14.4	46.0
7	5	-50	5	-34.4	-14.5	39.4
8	0	-50	0	-32.4	-15.2	32.4
9	-10	-50	-10	-29.7	-18.0	19.7
10	-15	-50	-15	-29.7	-20.4	14.7
11	-20	-50	-20	-31.7	-23.8	11.7
12	-30	-50	-30	-50	-37.4	20

In both tables, it is found that the independently controlled jaw force optimization strategy whose δ_{lower} < -36.3 μm and δ_{upper} > 9.7 μm yields the same solution as when the optimization is run at δ_{lower} = -50 μm and δ_{upper} = 50 μm. To observe the peak-to-valley roundness error and $\overline{\delta_{total}(\gamma)}$ at different range of δ_{lower} and δ_{upper} , data from Table 5-3 are plotted in Figure 5.14.

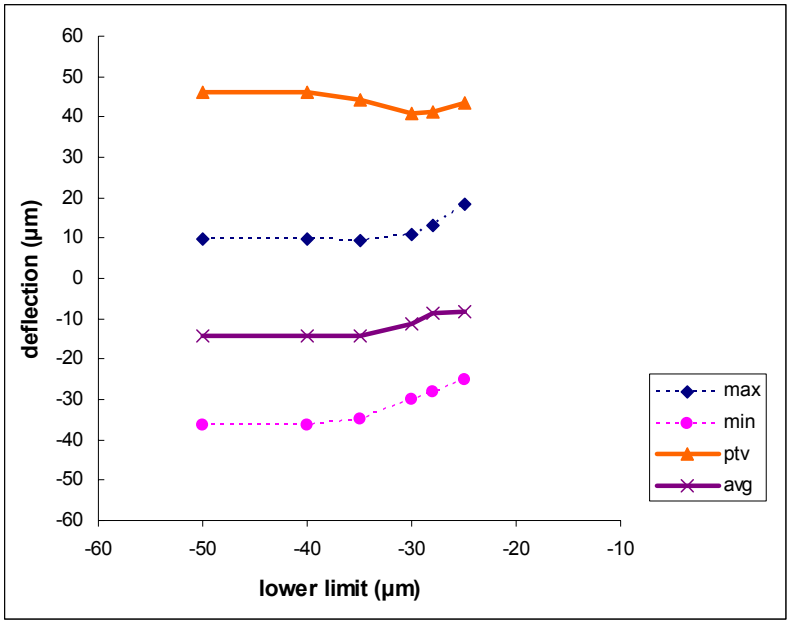

Figure 5.14 Results from increasing $\delta_{lower}$and δ_{upper} = 50 µm

The maximum and minimum of the profiles are represented by lines with diamond and circle marks, respectively. A line with triangle marks is the peak-to-valley roundness error and a line with cross marks is the average profile.

For δ_{lower}>-23 µm, the optimization model does not yield a feasible solution because no set of clamping force can satisfy the constraints in the optimization model particularly when the angular location of the cutting tool is located between the jaws. However, when δ_{lower}<-23 µm, it may be observed in Figure 5.14 that the peak-to-valley roundness error does not improve much as δ_{lower} is increased. The largest improvement is at δ_{lower} = -30 µm whose Δ_3 = 40.9 µm. It is also noticed that when δ_{lower} > -36.3, the value of $\delta_{total}(\gamma)_{\min}$ is increasing and equal to δ_{lower} while the value $\delta_{total}(\gamma)_{\max}$ is also increasing. This explains why the improvement of the roundness error is small even

though the magnitude of δ_{lower} is increased. It is also observed that the average of the total ring deflection due to cutting and unclamping effect in Figure 5.14 is increasing a little bit as the δ_{lower} is increased.

Similarly, to observe the peak-to-valley roundness error and $\overline{\delta_{total}(\gamma)}$ over a different range of δ_{lower} and δ_{upper} , data from Table 5-4are plotted in Figure 5.15.

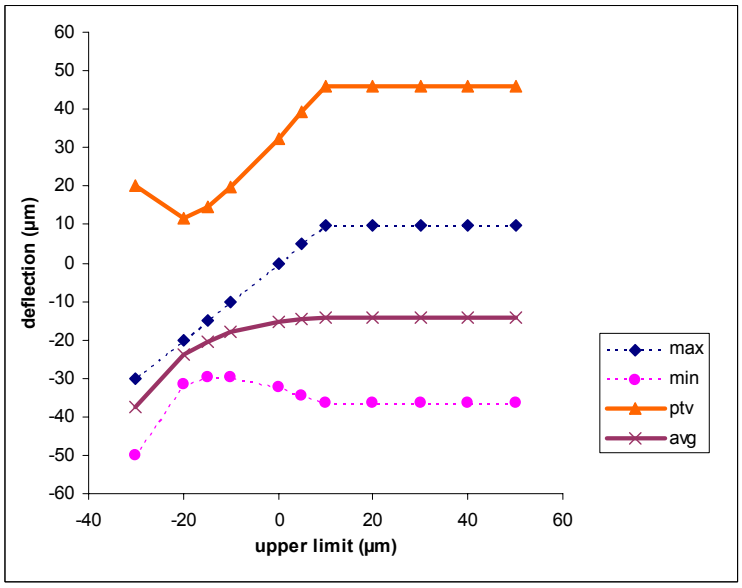

Figure 5.15 Results from decreasing δ_{upper} and δ_{lower} = 50 µm

It can be observed that for δ_{upper} < 9.7 µm, the $\delta_{total}(\gamma)_{\max}$ is decreasing and its value is equal to the set value of δ_{upper} , while $\delta_{total}(\gamma)_{\min}$ is increasing. As a result, the peak-to-valley roundness error improves a lot compared to that obtained by increasing δ_{lower} and setting δ_{upper} constant at 50 µm. However, when δ_{upper} < -10 µm, $\delta_{total}(\gamma)_{\min}$ starts decreasing. The value of $\delta_{total}(\gamma)_{\min}$ reaches its maximum at -30 µm. It is not

accidental that this value is close to the δ_{lower} in Table 5-3, when the optimization does not give a feasible solution.

From the above observation, in order to reach the smallest possible peak-to-valley roundness error and a reasonably small average of the total ring deflection due to cutting and unclamping effect, δ_{lower} needs to be set at its maximum allowable value of -23 µm and δ_{upper} needs to be set at a value larger but close to -23 µm. For example, the finished cut profile in Figure 5.17 is obtained when δ_{lower} is set at -23 µm and δ_{upper} is set at -18 µm. The overall peak-to-valley roundness error is 5 µm and the average of the total ring deflection due to cutting and unclamping effect is -20.5 µm. Figure 5.16 shows the clamping force variations required to accomplish the finished cut profile in Figure 5.17.

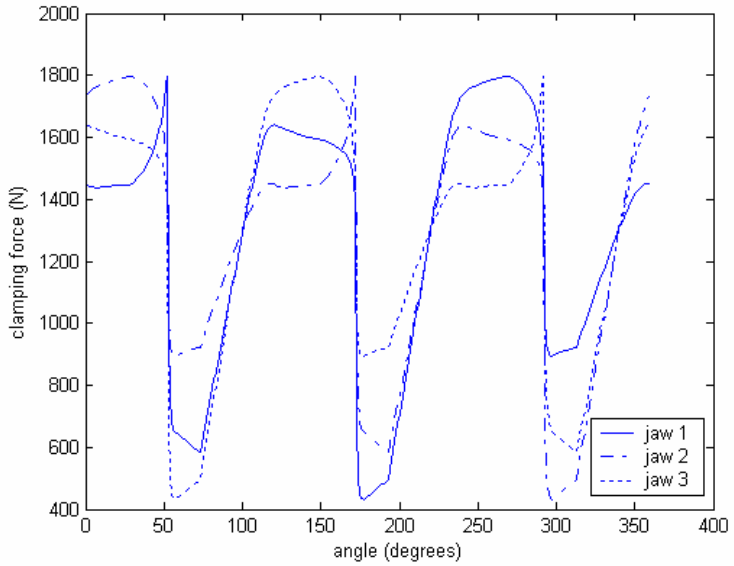

Figure 5.16 Clamping forces with δ_{lower} = -23 µm and δ_{upper} = -18 µm

In Figure 5.16, few sudden jumps in the clamping force from higher to lower values take place at approximately 50°, 180°, and 300°. The source of this phenomenon

comes from efforts of the optimization model to satisfy the upper and lower bounds specified in Eq. (5.19).

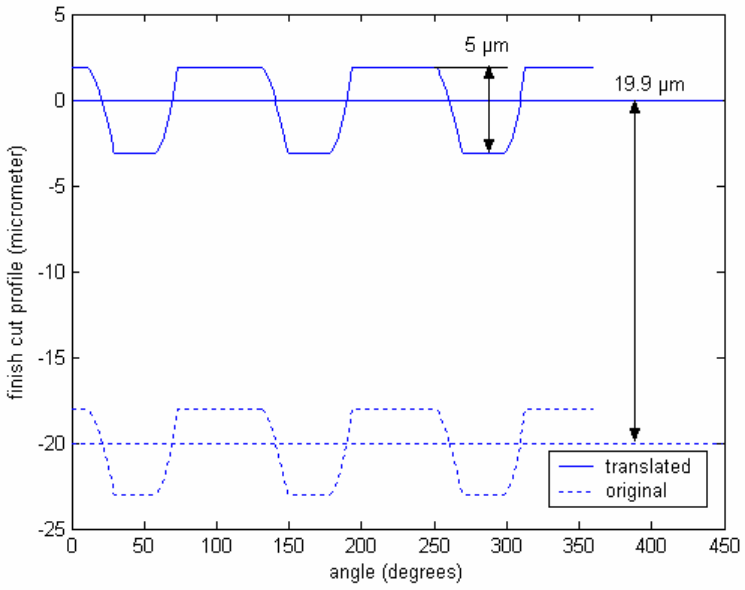

Figure 5.17 Finished cut profile with δ_{lower} = -23 µm and δ_{upper} = -18 µm

Between the peak-to-valley roundness error and the average of the total ring deflection due to cutting and unclamping effect $\overline{\delta_{total}(\gamma)}$, typically the peak-to-valley roundness error is more important because the error introduced by $\overline{\delta_{total}(\gamma)}$ can be compensated by increasing or decreasing d_{nom} to achieve the desired radius of the finished inner surface of the ring.

Additional constraints may also be included in this independently controlled chucking force optimization model depending on the physical limitation of the control system of the chuck.

5.3 Comparison of all models

In order to show the merits of the dynamic chucking force model over the conventional constant chucking force model, the resulting finished cut profiles of the three previously discussed examples are presented in Figure 5.18. First, the finished cut profiles derived from the conventional constant chucking model (Model #1) is indicated by the solid line whose peak-to-valley roundness error is 71.9 μm.

The second model (Model #2) whose chucking force at each jaw is the same but the magnitude is allowed to vary with respect to machining point gives a roundness error of 55.4 μm. The dotted line in Figure 5.18 shows the finished cut profile predicted by Model 2. Finally, the finished cut profile obtained from the independently controlled jaw force model (Model #3) is shown by a dashed line in Figure 5.18. This model gives the smallest roundness error which is 5 μm. In this model, the peak-to-valley roundness error is adjustable by changing the lower and upper bounds of the allowable range δ_{lower} and δ_{upper} in Eq. (5.19).

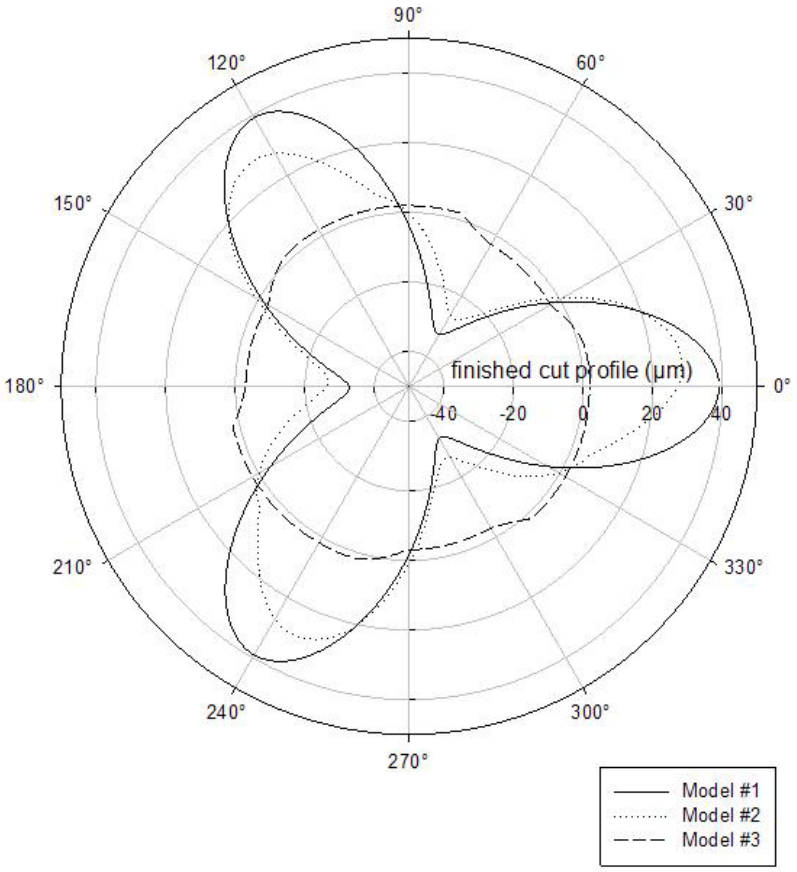

Figure 5.18 Finished cut profile comparisons

5.4 Summary

A systematic mathematical approach to find the minimum number of jaws and the range of acceptable chucking forces that ensures the required roundness tolerance while avoiding slip of the ring using a conventional constant chucking method has been presented. An example shows that this conventional way of chucking limits the

roundness capability of the three jaw chuck to 71.9 μm for the assumed ring material, geometry, and cutting conditions.

Two new flexible fixturing concepts are proposed to improve the roundness capability of the three jaw chuck and thus the accuracy of the machined ring. The first concept is has equal chucking force at each jaw but the magnitude is allowed to vary with respect to the angular location of the cutting tool. However, this model only shows a slight improvement in roundness capability of the chuck. The peak-to-valley roundness error of the cut ring produced by this model is 55.4 μm for the same conditions considered in the constant chucking force example.

The second concept consists of varying the individual jaw forces independently in such a way as to obtain a desired roundness error in the cut ring. This last model shows a significant improvement in peak-to-valley roundness error of the cut ring compared to the previous two models. Using the same ring material properties, geometry, friction coefficient, and cutting forces as in previous two examples, the last model results in peak-to-valley roundness error of the cut ring of 5 μm. This means that the novel concept of dynamic chucking force control promises to yield part roundness that is superior to that obtained in conventional chucking. Future research efforts will focus on developing a prototype adaptive chuck for use in turning application.

CHAPTER 6

CONCLUSIONS AND RECOMMENDATIONS

6.1 Conclusions

The primary objective of this thesis was to develop a systematic and model-based methodology for determining the optimum chucking conditions for turning of ring-shaped parts. In an effort to enhance the development of an optimization model, the following aspects were addressed:

- A theoretical and a finite element model of ring deformation were developed. The development of the theoretical model consists of two parts: i) a model that predicts the finished cut profile of a thin-walled ring held in a chuck with any number of jaws and ii) a model that predicts reaction forces at the interface between the workpiece and jaw surfaces.
- The validity of the finished cut prediction model was verified in a turning experiment using three different cutting conditions.

- A systematic mathematical approach for optimizing workholding parameters in a conventional chucking using the finished cut and reaction force prediction was developed.
- Two novel concepts of dynamic chucking force control that promise to yield part roundness that is superior to conventional chucking were presented.

6.1.1 Validation of Finished Cut Profile Prediction Model

The following conclusions pertain to rings turned in a conventional three-jaw chuck with point contact between the chuck jaws and the ring:

- The theoretical model prediction of the finished cut profile incorporating the chucking and cutting forces in turning of a ring yielded an average error of 19.9 % at the extreme points of the deformed ring. In addition, the mean absolute percentage error over all conditions was 8.5%. Those predictions were made by assuming the average of the inner diameters of the uncut and cut ring as the inner diameter in the theoretical model.
- The theoretical model prediction using the inner diameter of the cut ring as the inner diameter yielded a mean absolute percentage error of 22.1% over all conditions.

6.1.2 Conventional Chucking Optimization

For given ring material properties, geometry, friction coefficient, and cutting conditions, simulation shows that the conventional way of chucking limits the roundness

capability of the three jaw chuck to 71.9 μm with a constant value of minimum clamping force of 2372 N throughout the entire cut. For a desired tolerance that is less than 71.9 μm, the number of jaws required is greater than three.

6.1.3 Dynamic Chucking Optimization

- Ring material properties, geometry, friction coefficient, and cutting forces assumed in conventional chucking optimization are also assumed in dynamic chucking optimization. The second model whose chucking force at each jaw is the same but the magnitude is allowed to vary with respect to machining point gives a roundness error of 55.4 μm, which is an improvement of 23% over the results when applying a constant chucking force.
- Another dynamic chucking strategy is to vary the individual jaw forces independently so as to obtain a desired roundness error in the cut ring. In this model, the peak-to-valley roundness error is adjustable by changing the lower and upper bounds of the allowable range δ_{lower} and δ_{upper}.

6.2 Recommendations

In this thesis, the interaction between ring shaped part and workholding elements in turning operation has been investigated in detail. The investigation leads to an opportunity for introducing the concept of dynamic chucking force control. This novel

idea may relieve the limitations in turning of machining thin-walled ring shaped parts to roundness tolerances comparable to the grinding process.

However, the experimental validation presented in this thesis only involved finished cut prediction. More studies could be conducted to examine the validity of the reaction force prediction model under static and dynamic loading conditions. In addition, when optimizing the workholding parameters, the out-of-plane forces were not considered. The current optimization model in this thesis can then be extended to include the reaction forces in the out-of-plane direction.

In the case of chucking a very low compliance workpiece, the contact and fixture compliances do not have significant effect on the machined surface error. However, when predicting fixture-workpiece reaction forces as a result of clamping and cutting, the effects of the contact and fixture compliances are not well-understood. A study can be conducted to examine and include the contact and fixture compliances when predicting the fixture-workpiece reaction forces.

In a turning application, there is a limited amount of knowledge concerning the effect of vibration and oscillatory loads on the static coefficient of friction. A study of the static friction coefficient at workpiece-fixture contact during turning will be very beneficial in optimizing the workholding parameters. More work is also needed to understand how the independently control chuck will affect the static friction coefficient and the surface roughness of the workpiece. To study these effects and validate the improvement in workpiece quality using the concept of dynamic chucking, one needs to

build a prototype intelligent chuck with dynamic jaws capable of delivering accurate but varying clamping intensity.

APPENDIX A

ANSYS APDL File

```
! APDL file for the Finite Element Project
! Simulation is configured to run using metric units

finish                  ! exit from a processor
/clear, nostart         ! clears the database

!--------------------------------------------------------------------------
! define constants
!--------------------------------------------------------------------------

outer_radius            = 71e-3/2
inner_radius            = 58e-3/2
ring_depth              = 18.5e-3
jaw_width               = 20e-3
jaw_height              = 25e-3
jaw_depth               = ring_depth
extra                   = 0
jaw_number              = 3
jaw_force               = 2500
jaw_pressure            = jaw_force/(jaw_width*jaw_depth)
cuttingforce_tan        = 115
cuttingforce_rad        = 215
cuttingforce_ax         = 0
cuttingforce_angle1     = 0
cuttingforce_angle2      = 10
cuttingforce_angle3      = 20
cuttingforce_angle4      = 30
cuttingforce_angle5      = 40
cuttingforce_angle6      = 50
cuttingforce_angle7      = 60
cuttingforce_angle8      = 70
cuttingforce_angle9      = 80
```

```
cuttingforce_angle10   = 90
workpiece_material    = 1
workpiece_element     = 1
workpiece_E_modulus          = 201.33e9
workpiece_poisson     = 0.299
workpiece_friction    = 0.2
jaw_material          = 2
jaw_element           = 2
jaw_E_modulus         = 201.33e9
jaw_poisson           = 0.299
var                   = 8
division_ring_perimeters       = var*4
division_ring_contperi         = 12
division_ring_thickness        = var
division_ring_depth            = var*2
division_jaw_width_mid         = division_ring_contperi
division_jaw_width_sides       = var/2
division_jaw_depth    = var*2
division_jaw_height   = var*2
param_FKN             = 0.1
param_ICONT           = -2.79E-08
seltol                = 1.0001

!------------------------------------------------------------------------------
! set title and jobname
!------------------------------------------------------------------------------

/TITLE,Mesh4
/FILNAME,Mesh4,0
/prep7                  ! enters the preprocessor

!------------------------------------------------------------------------------
! define material properties
!------------------------------------------------------------------------------

MP, EX, workpiece_material, workpiece_E_modulus
MP, PRXY, workpiece_material, workpiece_poisson
MP, EX, jaw_material, jaw_E_modulus
MP, PRXY, jaw_material, jaw_poisson

!------------------------------------------------------------------------------
! define element type
!------------------------------------------------------------------------------
```

```
ET, workpiece_element, solid45
ET, jaw_element, solid45

!------------------------------------------------------------------------
! build ring geometry
!------------------------------------------------------------------------

CYL4, 0, 0, inner_radius,   -0.75, outer_radius,  0.75, ring_depth
CYL4, 0, 0, inner_radius,    119.25, outer_radius,  120.75, ring_depth
CYL4, 0, 0, inner_radius,   239.25, outer_radius, 240.75, ring_depth
CYL4, 0, 0, inner_radius,    0.75, outer_radius,  119.25, ring_depth
CYL4, 0, 0, inner_radius,    120.75, outer_radius, 239.25, ring_depth
CYL4, 0, 0, inner_radius,   240.75, outer_radius, 359.25, ring_depth
VGLUE, ALL
LSEL, S, RADIUS,,inner_radius,outer_radius
CSYS,1
LSEL, U, LOC, Y, 0
LSEL, U, LOC, Y, 120
LSEL, U, LOC, Y, 240
CM, lines_perimeters, LINE
CSYS,0
LSEL, S, RADIUS,,inner_radius,outer_radius
CMSEL, U, lines_perimeters
CM, lines_contperimeters, LINE
LSEL, S, LENGTH,, ring_depth
LSEL, R, LOC, Z, ring_depth/2
CM, lines_depth, LINE
LSEL, S, LENGTH,, outer_radius-inner_radius
CM, lines_thickness, LINE
ALLSEL, ALL
CM, volumes_ring, VOLU
ALLSEL, ALL

!------------------------------------------------------------------------
! build jaw geometry
!------------------------------------------------------------------------

jaw_width_mid1=0.5e-3
K,1001,outer_radius,jaw_width/2,0
K,1002,outer_radius+jaw_height,jaw_width/2,0
K,1003,outer_radius+jaw_height,jaw_width/2,jaw_depth
K,1004,outer_radius+extra,jaw_width/2,jaw_depth
K,1005,outer_radius,jaw_width_mid1,0
K,1006,outer_radius+jaw_height,jaw_width_mid1,0
```

```
K,1007,outer_radius+jaw_height,jaw_width_mid1,jaw_depth
K,1008,outer_radius+extra,jaw_width_mid1,jaw_depth
K,1009,outer_radius,-jaw_width_mid1,0
K,1010,outer_radius+jaw_height,-jaw_width_mid1,0
K,1011,outer_radius+jaw_height,-jaw_width_mid1,jaw_depth
K,1012,outer_radius+extra,-jaw_width_mid1,jaw_depth
K,1013,outer_radius,-jaw_width/2,0
K,1014,outer_radius+jaw_height,-jaw_width/2,0
K,1015,outer_radius+jaw_height,-jaw_width/2,jaw_depth
K,1016,outer_radius+extra,-jaw_width/2,jaw_depth
V,1001,1002,1003,1004,1005,1006,1007,1008
V,1005,1006,1007,1008,1009,1010,1011,1012
V,1009,1010,1011,1012,1013,1014,1015,1016
VGLUE, 4,5,6
ALLSEL, ALL
VSEL, U, VOLU,, volumes_ring
CM, volumes_jaw, VOLU
CSYS, 1
VGEN, jaw_number, volumes_jaw,,, 0, 360/jaw_number, 0, 0, 0,0
CM, volumes_jaw, VOLU
CSYS, 0
LSEL, R, LENGTH,, jaw_depth
LSEL, R, LOC, Z, ring_depth/2
CM, lines_jaw_depth, LINE
LSEL, S, LENGTH,, 2*jaw_width_mid1
CM, lines_jaw_width_mid, LINE
LSEL, S, LENGTH,, jaw_width/2-jaw_width_mid1
CM, lines_jaw_width_sides, LINE
LSEL, S, LENGTH,, jaw_height
CM, lines_jaw_height, LINE
LSEL, S, LENGTH,, jaw_height-extra
CM, lines_jaw_height2, LINE
ALLSEL, ALL

!--------------------------------------------------------------------------
! name jaw areas
!--------------------------------------------------------------------------

CSYS, 1
ASEL,S,AREA,,20
ASEL,A,AREA,,25
ASEL,A,AREA,,30
CM, jaw_backarea1, AREA
ASEL,S,AREA,,36
```

```
ASEL,A,AREA,,53
ASEL,A,AREA,,58
CM, jaw_backarea2, AREA
ASEL,S,AREA,,64
ASEL,A,AREA,,69
ASEL,A,AREA,,74
CM, jaw_backarea3, AREA
CSYS, 0
ALLSEL, ALL

!-------------------------------------------------------------------------
! asign material attributes to volumes
!-------------------------------------------------------------------------

CMSEL, S, volumes_ring
VATT, workpiece_material,, workpiece_element
CMSEL, S, volumes_jaw
VATT, jaw_material,, jaw_element
ALLSEL, ALL

!-------------------------------------------------------------------------
! define mesh
!-------------------------------------------------------------------------

LESIZE, lines_contperimeters,,, division_ring_contperi
LESIZE, lines_perimeters,,, division_ring_perimeters
LESIZE, lines_depth,,, division_ring_depth
LESIZE, lines_thickness,,, division_ring_thickness
VSWEEP, volumes_ring
LESIZE, lines_jaw_width_mid,,, division_jaw_width_mid
LESIZE, lines_jaw_width_sides,,, division_jaw_width_sides
LESIZE, lines_jaw_height,,, division_jaw_height
LESIZE, lines_jaw_depth,,, division_jaw_depth
VSWEEP, volumes_jaw

!-------------------------------------------------------------------------
! select and name nodes
!-------------------------------------------------------------------------

CSYS,1
NSEL, ALL
cuttingforce_node1=NODE(inner_radius, cuttingforce_angle1, ring_depth/2)
cuttingforce_node2=NODE(inner_radius, cuttingforce_angle2, ring_depth/2)
cuttingforce_node3=NODE(inner_radius, cuttingforce_angle3, ring_depth/2)
```

```
cuttingforce_node4=NODE(inner_radius, cuttingforce_angle4, ring_depth/2)
cuttingforce_node5=NODE(inner_radius, cuttingforce_angle5, ring_depth/2)
cuttingforce_node6=NODE(inner_radius, cuttingforce_angle6, ring_depth/2)
cuttingforce_node7=NODE(inner_radius, cuttingforce_angle7, ring_depth/2)
cuttingforce_node8=NODE(inner_radius, cuttingforce_angle8, ring_depth/2)
cuttingforce_node9=NODE(inner_radius, cuttingforce_angle9, ring_depth/2)
cuttingforce_node10=NODE(inner_radius, cuttingforce_angle10, ring_depth/2)
CSYS,0
ALLSEL, ALL

!------------------------------------------------------------------------------
! create contact pair 1
!------------------------------------------------------------------------------

CM,_NODECM,NODE
CM,_ELEMCM,ELEM
CM,_LINECM,LINE
CM,_AREACM,AREA
/GSAV,cwz,gsav,,temp
MP,MU,1,workpiece_friction
MAT,1
R,3,0,0,param_FKN,param_FTOLN,param_ICONT,0,
REAL,3
ET,3,170
ET,4,174
!effect of init penet and gap
KEYOPT,4,9,0
! Generate the target surface   - modified before was 9
ASEL,S,,,28
CM,_TARGET,AREA
TYPE,3
NSLA,S,1
ESLN,S,0
ESURF,ALL
CMSEL,S,_ELEMCM
! Generate the contact surface
ASEL,S,,,3
CM,_CONTACT,AREA
TYPE,4
NSLA,S,1
ESLN,S,0
ESURF,ALL
ALLSEL
ESEL,ALL
```

```
ESEL,S,TYPE,,3
ESEL,A,TYPE,,4
ESEL,R,REAL,,3
/PSYMB,ESYS,1
/PNUM,TYPE,1
/NUM,1
EPLOT
ESEL,ALL
ESEL,S,TYPE,,3
ESEL,A,TYPE,,4
ESEL,R,REAL,,3
CMSEL,A,_NODECM
CMDEL,_NODECM
CMSEL,A,_ELEMCM
CMDEL,_ELEMCM
CMSEL,S,_LINECM
CMDEL,_LINECM
CMSEL,S,_AREACM
CMDEL,_AREACM
/GRES,cwz,gsav
CMDEL,_TARGET
CMDEL,_CONTACT

!-----------------------------------------------------------------------------
! create contact pair 2
!-----------------------------------------------------------------------------

CM,_NODECM,NODE
CM,_ELEMCM,ELEM
CM,_LINECM,LINE
CM,_AREACM,AREA
/GSAV,cwz,gsav,,temp
MP,MU,1,workpiece_friction
MAT,1
R,4,0,0,param_FKN,param_FTOLN,param_ICONT,0,
REAL,4
ET,5,170
ET,6,174
KEYOPT,6,9,0
! Generate the target surface    - modified before was 16
ASEL,S,,,56
CM,_TARGET,AREA
TYPE,5
NSLA,S,1
```

```
ESLN,S,0
ESURF,ALL
CMSEL,S,_ELEMCM
! Generate the contact surface
ASEL,S,,,9
CM,_CONTACT,AREA
TYPE,6
NSLA,S,1
ESLN,S,0
ESURF,ALL
ALLSEL
ESEL,ALL
ESEL,S,TYPE,,5
ESEL,A,TYPE,,6
ESEL,R,REAL,,4
/PSYMB,ESYS,1
/PNUM,TYPE,1
/NUM,1
EPLOT
ESEL,ALL
ESEL,S,TYPE,,5
ESEL,A,TYPE,,6
ESEL,R,REAL,,4
CMSEL,A,_NODECM
CMDEL,_NODECM
CMSEL,A,_ELEMCM
CMDEL,_ELEMCM
CMSEL,S,_LINECM
CMDEL,_LINECM
CMSEL,S,_AREACM
CMDEL,_AREACM
/GRES,cwz,gsav
CMDEL,_TARGET
CMDEL,_CONTACT

!*****************************************************************************
! create contact pair 3
!*****************************************************************************

/COM, CONTACT PAIR CREATION - START
CM,_NODECM,NODE
CM,_ELEMCM,ELEM
CM,_LINECM,LINE
CM,_AREACM,AREA
```

```
/GSAV,cwz,gsav,,temp
MP,MU,1,workpiece_friction
MAT,1
R,5,0,0,param_FKN,param_FTOLN,param_ICONT,0,
REAL,5
ET,7,170
ET,8,174
KEYOPT,8,9,0
! Generate the target surface    - modified before was 23
ASEL,S,,,72
CM,_TARGET,AREA
TYPE,7
NSLA,S,1
ESLN,S,0
ESURF,ALL
CMSEL,S,_ELEMCM
! Generate the contact surface
ASEL,S,,,15
CM,_CONTACT,AREA
TYPE,8
NSLA,S,1
ESLN,S,0
ESURF,ALL
ALLSEL
ESEL,ALL
ESEL,S,TYPE,,7
ESEL,A,TYPE,,8
ESEL,R,REAL,,5
/PSYMB,ESYS,1
/PNUM,TYPE,1
/NUM,1
EPLOT
ESEL,ALL
ESEL,S,TYPE,,7
ESEL,A,TYPE,,8
ESEL,R,REAL,,5
CMSEL,A,_NODECM
CMDEL,_NODECM
CMSEL,A,_ELEMCM
CMDEL,_ELEMCM
CMSEL,S,_LINECM
CMDEL,_LINECM
CMSEL,S,_AREACM
CMDEL,_AREACM
```

```
/GRES,cwz,gsav
CMDEL,_TARGET
CMDEL,_CONTACT
/COM, CONTACT PAIR CREATION - END

!--------------------------------------------------------------------------
! apply cutting force
!--------------------------------------------------------------------------

CSYS, 1
ASEL, S, LOC, X, inner_radius
NORA, all, 1
CSYS, 0
ALLSEL, ALL

!--------------------------------------------------------------------------
! displacement constraints on jaws
!--------------------------------------------------------------------------
CMSEL, S, jaw_backarea1
NSLA,S,1
NMODIF, ALL,,,,0
D, ALL, , 0, , , ,UY,UZ, , , ,
D, ALL,UX,-2e-5  , , , ,  ,  , , , ,
CMSEL, S, jaw_backarea2
NSLA,S,1
NMODIF, ALL,,,,120
D, ALL, , 0, , , ,UY,UZ, , , ,
D, ALL,UX,-2e-5  , , , ,  ,  , , , ,
CMSEL, S, jaw_backarea3
NSLA,S,1
NMODIF, ALL,,,,240
D, ALL, , 0, , , ,UY,UZ, , , ,
D, ALL,UX,-2e-5  , , , ,  ,  , , , ,
ALLSEL, ALL

!--------------------------------------------------------------------------
! set solution options
!--------------------------------------------------------------------------

ANTYPE,0
NLGEOM,0                    ! choose small displacement analysis
NSUBST,4,100,1

!--------------------------------------------------------------------------
```

```
! solve the system
!------------------------------------------------------------------------------
/SOLU
! Load Step 1:
CSYS, 1
F, cuttingforce_node1, FX, cuttingforce_rad
F, cuttingforce_node1, FY, cuttingforce_tan
F, cuttingforce_node1, FZ, cuttingforce_ax
CSYS, 0
ALLSEL, ALL
LSWRITE

! Load Step 2:
CSYS, 1
F, cuttingforce_node1, FX, 0
F, cuttingforce_node1, FY, 0
F, cuttingforce_node1, FZ, 0
F, cuttingforce_node2, FX, cuttingforce_rad
F, cuttingforce_node2, FY, cuttingforce_tan
F, cuttingforce_node2, FZ, cuttingforce_ax
CSYS, 0
ALLSEL, ALL
LSWRITE

! Load Step 3:
CSYS, 1
F, cuttingforce_node2, FX, 0
F, cuttingforce_node2, FY, 0
F, cuttingforce_node2, FZ, 0
F, cuttingforce_node3, FX, cuttingforce_rad
F, cuttingforce_node3, FY, cuttingforce_tan
F, cuttingforce_node3, FZ, cuttingforce_ax
CSYS, 0
ALLSEL, ALL
LSWRITE

! Load Step 4:
CSYS, 1
F, cuttingforce_node3, FX, 0
F, cuttingforce_node3, FY, 0
F, cuttingforce_node3, FZ, 0
F, cuttingforce_node4, FX, cuttingforce_rad
F, cuttingforce_node4, FY, cuttingforce_tan
F, cuttingforce_node4, FZ, cuttingforce_ax
```

```
CSYS, 0
ALLSEL, ALL
LSWRITE

! Load Step 5:
CSYS, 1
F, cuttingforce_node4, FX, 0
F, cuttingforce_node4, FY, 0
F, cuttingforce_node4, FZ, 0
F, cuttingforce_node5, FX, cuttingforce_rad
F, cuttingforce_node5, FY, cuttingforce_tan
F, cuttingforce_node5, FZ, cuttingforce_ax
CSYS, 0
ALLSEL, ALL
LSWRITE

! Load Step 6:
CSYS, 1
F, cuttingforce_node5, FX, 0
F, cuttingforce_node5, FY, 0
F, cuttingforce_node5, FZ, 0
F, cuttingforce_node6, FX, cuttingforce_rad
F, cuttingforce_node6, FY, cuttingforce_tan
F, cuttingforce_node6, FZ, cuttingforce_ax
CSYS, 0
ALLSEL, ALL
LSWRITE

! Load Step 7:
CSYS, 1
F, cuttingforce_node6, FX, 0
F, cuttingforce_node6, FY, 0
F, cuttingforce_node6, FZ, 0
F, cuttingforce_node7, FX, cuttingforce_rad
F, cuttingforce_node7, FY, cuttingforce_tan
F, cuttingforce_node7, FZ, cuttingforce_ax
CSYS, 0
ALLSEL, ALL
LSWRITE

! Load Step 8:
CSYS, 1
F, cuttingforce_node7, FX, 0
F, cuttingforce_node7, FY, 0
```

```
F, cuttingforce_node7, FZ, 0
F, cuttingforce_node8, FX, cuttingforce_rad
F, cuttingforce_node8, FY, cuttingforce_tan
F, cuttingforce_node8, FZ, cuttingforce_ax
CSYS, 0
ALLSEL, ALL
LSWRITE

! Load Step 9:
CSYS, 1
F, cuttingforce_node8, FX, 0
F, cuttingforce_node8, FY, 0
F, cuttingforce_node8, FZ, 0
F, cuttingforce_node9, FX, cuttingforce_rad
F, cuttingforce_node9, FY, cuttingforce_tan
F, cuttingforce_node9, FZ, cuttingforce_ax
CSYS, 0
ALLSEL, ALL
LSWRITE

! Load Step 10:
CSYS, 1
F, cuttingforce_node9, FX, 0
F, cuttingforce_node9, FY, 0
F, cuttingforce_node9, FZ, 0
F, cuttingforce_node10, FX, cuttingforce_rad
F, cuttingforce_node10, FY, cuttingforce_tan
F, cuttingforce_node10, FZ, cuttingforce_ax
CSYS, 0
ALLSEL, ALL
LSWRITE

LSSOLVE,1,5
```

APPENDIX B

Maple Code

To obtain deflection formula for θ = 0° to 120°

```
> E:=202016380100:
> G:=79289705500:
> k1:=1.2:
> A:=thickness*width:
> I1:=width*(thickness^3)/12:
> alpha_prime:=(1/(E*I1)):
> beta_prime:=1/(E*A):
> beta_2_prime:=1/(G*A):
> mu:=((-beta_prime + k1*beta_2_prime + alpha_prime*r^2)/(beta_prime +
k1*beta_2_prime + alpha_prime*r^2)):
> phi1:=0:
> phi2:=120*Pi/180:
> phi3:=240*Pi/180:
>N_0:=(phi1/(2*Pi))*P1*sin(phi1)+(phi2/(2*Pi))*P2*sin(phi2)+(phi3/(2*Pi))*P3*sin(ph
i3)-
(gamma1/(2*Pi))*F_R*sin(gamma1)+(phi1/(2*Pi))*T1*cos(phi1)+(phi2/(2*Pi))*T2*cos
(phi2) +(phi3/(2*Pi))*T3*cos(phi3)-(gamma1/(2*Pi))*F_T*cos(gamma1)-
(mu/(2*Pi))*T1*sin(phi1)-(mu/(2*Pi))*T2*sin(phi2)-
(mu/(2*Pi))*T3*sin(phi3)+(mu/(2*Pi))*F_T*sin(gamma1):
>Q_0:=(phi1/(2*Pi))*P1*cos(phi1)+(phi2/(2*Pi))*P2*cos(phi2)+(phi3/(2*Pi))*P3*cos(p
hi3) -(gamma1/(2*Pi))*F_R*cos(gamma1)-(phi1/(2*Pi))*T1*sin(phi1)-
(phi2/(2*Pi))*T2*sin(phi2) -
(phi3/(2*Pi))*T3*sin(phi3)+(gamma1/(2*Pi))*F_T*sin(gamma1)-
(mu/(2*Pi))*T1*cos(phi1) -(mu/(2*Pi))*T2*cos(phi2)-
(mu/(2*Pi))*T3*cos(phi3)+(mu/(2*Pi))*F_T*cos(gamma1):
> M_0:=-r*N_0-(r/(2*Pi))*(P1+P2+P3-F_R)+(r/(2*Pi))*(phi1*T1+phi2*T2+phi3*T3-
gamma1*F_T):
> M_phi1:=M_0 + Q_0*r*sin(phi) + N_0*r*(1-cos(phi)) + P1*r*sin(phi-phi1) +
T1*r*(1-cos(phi-phi1)):
> M_phi2:=M_0 + Q_0*r*sin(phi) + N_0*r*(1-cos(phi)) + P1*r*sin(phi-phi1) -
F_R*r*sin(phi-gamma1) + T1*r*(1-cos(phi-phi1)) - F_T*r*(1-cos(phi-gamma1)):
```

```
> M_phi3:=M_0 + Q_0*r*sin(phi) + N_0*r*(1-cos(phi)) + P1*r*sin(phi-phi1) +
P2*r*sin(phi-phi2)   - F_R*r*sin(phi-gamma1) + T1*r*(1-cos(phi-phi1)) + T2*r*(1-
cos(phi-phi2)) - F_T*r*(1-cos(phi-gamma1)):
> M_phi4:=M_0 + Q_0*r*sin(phi) + N_0*r*(1-cos(phi)) + P1*r*sin(phi-phi1) +
P2*r*sin(phi-phi2) + P3*r*sin(phi-phi3) - F_R*r*sin(phi-gamma1) + T1*r*(1-cos(phi-
phi1)) + T2*r*(1-cos(phi-phi2)) + T3*r*(1-cos(phi-phi3)) - F_T*r*(1-cos(phi-gamma1)):
>Ubeam:=(int((M_phi1^2*r)/(2*E*I1),phi=phi1..gamma1)+int((M_phi2^2*r)/(2*E*I1),p
hi=gamma1..phi2)+int((M_phi3^2*r)/(2*E*I1),phi=phi2..phi3)+int((M_phi4^2*r)/(2*E*I
1),phi=phi3..(2*Pi))):
> Eq1:=-F_R*cos(gamma1)+F_T*sin(gamma1)+P1*cos(phi1)-
T1*sin(phi1)+P2*cos(phi2)-T2*sin(phi2)+P3*cos(phi3)-T3*sin(phi3):
> Eq2:=-F_R*sin(gamma1)-
F_T*cos(gamma1)+P1*sin(phi1)+T1*cos(phi1)+P2*sin(phi2)+T2*cos(phi2)+P3*sin(phi
3)+T3*cos(phi3):
> Eq3:=-r*F_T+r*(T1+T2+T3):
> s:=solve({Eq1,Eq2,Eq3},{T1,T2,T3}):
> assign(s):
> Deflect:=diff(Ubeam,F_R):
> simplify(Deflect);
```

To obtain deflection formula for θ = 120° to 240°

```
> E:=202016380100:
> G:=79289705500:
> k1:=1.2:
> A:=thickness*width:
> I1:=width*(thickness^3)/12:
> alpha_prime:=(1/(E*I1)):
> beta_prime:=1/(E*A):
> beta_2_prime:=1/(G*A):
> mu:=((-beta_prime + k1*beta_2_prime + alpha_prime*r^2)/(beta_prime +
k1*beta_2_prime + alpha_prime*r^2)):
> phi1:=0:
> phi2:=120*Pi/180:
> phi3:=240*Pi/180:
> alpha:=1.2:
>N_0:=(phi1/(2*Pi))*P1*sin(phi1)+(phi2/(2*Pi))*P2*sin(phi2)+(phi3/(2*Pi))*P3*sin(ph
i3) -
(gamma1/(2*Pi))*F_R*sin(gamma1)+(phi1/(2*Pi))*T1*cos(phi1)+(phi2/(2*Pi))*T2*cos
(phi2) +(phi3/(2*Pi))*T3*cos(phi3)-(gamma1/(2*Pi))*F_T*cos(gamma1)-
(mu/(2*Pi))*T1*sin(phi1)-(mu/(2*Pi))*T2*sin(phi2)-
(mu/(2*Pi))*T3*sin(phi3)+(mu/(2*Pi))*F_T*sin(gamma1):
>Q_0:=(phi1/(2*Pi))*P1*cos(phi1)+(phi2/(2*Pi))*P2*cos(phi2)+(phi3/(2*Pi))*P3*cos(p
hi3) -(gamma1/(2*Pi))*F_R*cos(gamma1)-(phi1/(2*Pi))*T1*sin(phi1)-
(phi2/(2*Pi))*T2*sin(phi2) -
```

```
(phi3/(2*Pi))*T3*sin(phi3)+(gamma1/(2*Pi))*F_T*sin(gamma1)-
(mu/(2*Pi))*T1*cos(phi1) -(mu/(2*Pi))*T2*cos(phi2)-
(mu/(2*Pi))*T3*cos(phi3)+(mu/(2*Pi))*F_T*cos(gamma1):
> M_0:=-r*N_0-(r/(2*Pi))*(P1+P2+P3-F_R)+(r/(2*Pi))*(phi1*T1+phi2*T2+phi3*T3-
gamma1*F_T):
> M_phi1:=M_0 + Q_0*r*sin(phi) + N_0*r*(1-cos(phi)) + P1*r*sin(phi-phi1) +
T1*r*(1-cos(phi-phi1)):
> M_phi2:=M_0 + Q_0*r*sin(phi) + N_0*r*(1-cos(phi)) + P1*r*sin(phi-phi1) +
P2*r*sin(phi-phi2)+ T1*r*(1-cos(phi-phi1))+T2*r*(1-cos(phi-phi2)):
> M_phi3:=M_0 + Q_0*r*sin(phi) + N_0*r*(1-cos(phi)) + P1*r*sin(phi-phi1) +
P2*r*sin(phi-phi2)   - F_R*r*sin(phi-gamma1) + T1*r*(1-cos(phi-phi1)) + T2*r*(1-
cos(phi-phi2)) - F_T*r*(1-cos(phi-gamma1)):
> M_phi4:=M_0 + Q_0*r*sin(phi) + N_0*r*(1-cos(phi)) + P1*r*sin(phi-phi1) +
P2*r*sin(phi-phi2) + P3*r*sin(phi-phi3) - F_R*r*sin(phi-gamma1) + T1*r*(1-cos(phi-
phi1)) + T2*r*(1-cos(phi-phi2)) + T3*r*(1-cos(phi-phi3)) - F_T*r*(1-cos(phi-gamma1)):
>Ubeam:=(int((M_phi1^2*r)/(2*E*I1),phi=phi1..phi2)+int((M_phi2^2*r)/(2*E*I1),phi=
phi2..gamma1)+int((M_phi3^2*r)/(2*E*I1),phi=gamma1..phi3)+int((M_phi4^2*r)/(2*E*
I1),phi=phi3..(2*Pi))):
> Eq1:=-F_R*cos(gamma1)+F_T*sin(gamma1)+P1*cos(phi1)-
T1*sin(phi1)+P2*cos(phi2)-T2*sin(phi2)+P3*cos(phi3)-T3*sin(phi3):
> Eq2:=-F_R*sin(gamma1)-
F_T*cos(gamma1)+P1*sin(phi1)+T1*cos(phi1)+P2*sin(phi2)+T2*cos(phi2)+P3*sin(phi
3)+T3*cos(phi3):
> Eq3:=-r*F_T+r*(T1+T2+T3):
> s:=solve({Eq1,Eq2,Eq3},{T1,T2,T3}):
> assign(s):
> Deflect:=diff(Ubeam,F_R):
> simplify(Deflect);
```

To obtain deflection formula for θ = 240° to 360°

```
> E:=202016380100:
> G:=79289705500:
> k1:=1.2:
> A:=thickness*width:
> I1:=width*(thickness^3)/12:
> alpha_prime:=(1/(E*I1)):
> beta_prime:=1/(E*A):
> beta_2_prime:=1/(G*A):
> mu:=((-beta_prime + k1*beta_2_prime + alpha_prime*r^2)/(beta_prime +
k1*beta_2_prime + alpha_prime*r^2)):
> phi1:=0:
> phi2:=120*Pi/180:
> phi3:=240*Pi/180:
> alpha:=1.2:
```

```
>N_0:=(phi1/(2*Pi))*P1*sin(phi1)+(phi2/(2*Pi))*P2*sin(phi2)+(phi3/(2*Pi))*P3*sin(ph
i3) -
(gamma1/(2*Pi))*F_R*sin(gamma1)+(phi1/(2*Pi))*T1*cos(phi1)+(phi2/(2*Pi))*T2*cos
(phi2) +(phi3/(2*Pi))*T3*cos(phi3)-(gamma1/(2*Pi))*F_T*cos(gamma1)-
(mu/(2*Pi))*T1*sin(phi1)-(mu/(2*Pi))*T2*sin(phi2)-
(mu/(2*Pi))*T3*sin(phi3)+(mu/(2*Pi))*F_T*sin(gamma1):
>Q_0:=(phi1/(2*Pi))*P1*cos(phi1)+(phi2/(2*Pi))*P2*cos(phi2)+(phi3/(2*Pi))*P3*cos(p
hi3) -(gamma1/(2*Pi))*F_R*cos(gamma1)-(phi1/(2*Pi))*T1*sin(phi1)-
(phi2/(2*Pi))*T2*sin(phi2) -
(phi3/(2*Pi))*T3*sin(phi3)+(gamma1/(2*Pi))*F_T*sin(gamma1)-
(mu/(2*Pi))*T1*cos(phi1) -(mu/(2*Pi))*T2*cos(phi2)-
(mu/(2*Pi))*T3*cos(phi3)+(mu/(2*Pi))*F_T*cos(gamma1):
> M_0:=-r*N_0-(r/(2*Pi))*(P1+P2+P3-F_R)+(r/(2*Pi))*(phi1*T1+phi2*T2+phi3*T3-
gamma1*F_T):
> M_phi1:=M_0 + Q_0*r*sin(phi) + N_0*r*(1-cos(phi)) + P1*r*sin(phi-phi1) +
T1*r*(1-cos(phi-phi1)):
> M_phi2:=M_0 + Q_0*r*sin(phi) + N_0*r*(1-cos(phi)) + P1*r*sin(phi-phi1) +
P2*r*sin(phi-phi2)+ T1*r*(1-cos(phi-phi1))+T2*r*(1-cos(phi-phi2)):
> M_phi3:=M_0 + Q_0*r*sin(phi) + N_0*r*(1-cos(phi)) + P1*r*sin(phi-phi1) +
P2*r*sin(phi-phi2) + P3*r*sin(phi-phi3) + T1*r*(1-cos(phi-phi1)) + T2*r*(1-cos(phi-
phi2)) + T3*r*(1-cos(phi-phi3)):
> M_phi4:=M_0 + Q_0*r*sin(phi) + N_0*r*(1-cos(phi)) + P1*r*sin(phi-phi1) +
P2*r*sin(phi-phi2) + P3*r*sin(phi-phi3) - F_R*r*sin(phi-gamma1) + T1*r*(1-cos(phi-
phi1)) + T2*r*(1-cos(phi-phi2)) + T3*r*(1-cos(phi-phi3)) - F_T*r*(1-cos(phi-gamma1)):
>Ubeam:=(int((M_phi1^2*r)/(2*E*I1),phi=phi1..phi2)+int((M_phi2^2*r)/(2*E*I1),phi=
phi2..phi3)+int((M_phi3^2*r)/(2*E*I1),phi=phi3..gamma1)+int((M_phi4^2*r)/(2*E*I1),
phi=gamma1..(2*Pi))):
> Eq1:=-F_R*cos(gamma1)+F_T*sin(gamma1)+P1*cos(phi1)-
T1*sin(phi1)+P2*cos(phi2)-T2*sin(phi2)+P3*cos(phi3)-T3*sin(phi3):
> Eq2:=-F_R*sin(gamma1)-
F_T*cos(gamma1)+P1*sin(phi1)+T1*cos(phi1)+P2*sin(phi2)+T2*cos(phi2)+P3*sin(phi
3)+T3*cos(phi3):
> Eq3:=-r*F_T+r*(T1+T2+T3):
> s:=solve({Eq1,Eq2,Eq3},{T1,T2,T3}):
> assign(s):
> Deflect:=diff(Ubeam,F_R):
> evalf(simplify(Deflect));
```

To obtain reaction force formula for θ = 0° to 120°

```
> E:=202016380100:
> G:=79289705500:
> rout:=0.0528/2:
> rin:=0.0462/2:
> r:=(rout+rin)/2:
```

```
> thickness:=rout-rin:
> width:=0.0254:
> k1:=1.2:
> A:=thickness*width:
> I1:=width*(thickness^3)/12:
> alpha_prime:=(1/(E*I1)):
> beta_prime:=1/(E*A):
> beta_2_prime:=1/(G*A):
> mu:=((-beta_prime + k1*beta_2_prime + alpha_prime*r^2)/(beta_prime +
k1*beta_2_prime + alpha_prime*r^2)):
> phi1:=0:
> phi2:=120*Pi/180:
> phi3:=240*Pi/180:
>N_0:=(phi1/(2*Pi))*R1*sin(phi1)+(phi2/(2*Pi))*R2*sin(phi2)+(phi3/(2*Pi))*R3*sin(p
hi3) -
(gamma1/(2*Pi))*F_R*sin(gamma1)+(phi1/(2*Pi))*T1*cos(phi1)+(phi2/(2*Pi))*T2*cos
(phi2) +(phi3/(2*Pi))*T3*cos(phi3)-(gamma1/(2*Pi))*F_T*cos(gamma1)-
(mu/(2*Pi))*T1*sin(phi1)-(mu/(2*Pi))*T2*sin(phi2)-
(mu/(2*Pi))*T3*sin(phi3)+(mu/(2*Pi))*F_T*sin(gamma1):
>Q_0:=(phi1/(2*Pi))*R1*cos(phi1)+(phi2/(2*Pi))*R2*cos(phi2)+(phi3/(2*Pi))*R3*cos(
phi3) -(gamma1/(2*Pi))*F_R*cos(gamma1)-(phi1/(2*Pi))*T1*sin(phi1)-
(phi2/(2*Pi))*T2*sin(phi2) -
(phi3/(2*Pi))*T3*sin(phi3)+(gamma1/(2*Pi))*F_T*sin(gamma1)-
(mu/(2*Pi))*T1*cos(phi1) -(mu/(2*Pi))*T2*cos(phi2)-
(mu/(2*Pi))*T3*cos(phi3)+(mu/(2*Pi))*F_T*cos(gamma1):
> M_0:=-r*N_0-(r/(2*Pi))*(R1+R2+R3-F_R)+(r/(2*Pi))*(phi1*T1+phi2*T2+phi3*T3-
gamma1*F_T):
> M_phi1:=M_0 + Q_0*r*sin(phi) + N_0*r*(1-cos(phi)) + R1*r*sin(phi-phi1) +
T1*r*(1-cos(phi-phi1)):
> M_phi2:=M_0 + Q_0*r*sin(phi) + N_0*r*(1-cos(phi)) + R1*r*sin(phi-phi1) -
F_R*r*sin(phi-gamma1) + T1*r*(1-cos(phi-phi1)) - F_T*r*(1-cos(phi-gamma1)):
> M_phi3:=M_0 + Q_0*r*sin(phi) + N_0*r*(1-cos(phi)) + R1*r*sin(phi-phi1) +
R2*r*sin(phi-phi2)   - F_R*r*sin(phi-gamma1) + T1*r*(1-cos(phi-phi1)) + T2*r*(1-
cos(phi-phi2)) - F_T*r*(1-cos(phi-gamma1)):
> M_phi4:=M_0 + Q_0*r*sin(phi) + N_0*r*(1-cos(phi)) + R1*r*sin(phi-phi1) +
R2*r*sin(phi-phi2) + R3*r*sin(phi-phi3) - F_R*r*sin(phi-gamma1) + T1*r*(1-cos(phi-
phi1)) + T2*r*(1-cos(phi-phi2)) + T3*r*(1-cos(phi-phi3)) - F_T*r*(1-cos(phi-gamma1)):
>Ubeam:=(int((M_phi1^2*r)/(2*E*I1),phi=phi1..gamma1)+int((M_phi2^2*r)/(2*E*I1),p
hi=gamma1..phi2)+int((M_phi3^2*r)/(2*E*I1),phi=phi2..phi3)+int((M_phi4^2*r)/(2*E*I
1),phi=phi3..(2*Pi))):
> Eq1:=-F_R*cos(gamma1)+F_T*sin(gamma1)+R1*cos(phi1)-
T1*sin(phi1)+R2*cos(phi2)-T2*sin(phi2)+R3*cos(phi3)-T3*sin(phi3):
```

```
> Eq2:=-F_R*sin(gamma1)-
F_T*cos(gamma1)+R1*sin(phi1)+T1*cos(phi1)+R2*sin(phi2)+T2*cos(phi2)+R3*sin(ph
i3)+T3*cos(phi3):
> Eq3:=-r*F_T+r*(T1+T2+T3):
> s:=solve({Eq1,Eq2,Eq3},{T1,T2,T3}):
> assign(s):
> first:=diff(Ubeam,R1):
> second:=diff(Ubeam,R2):
> third:=diff(Ubeam,R3):
> final:=solve({first,second,third},{R1,R2,R3}):
> assign(final):
```

To obtain reaction force formula for θ = 120° to 240°

```
> E:=202016380100:
> G:=79289705500:
> rout:=0.0528/2:
> rin:=0.0462/2:
> r:=(rout+rin)/2:
> thickness:=rout-rin:
> width:=0.0254:
> k1:=1.2:
> A:=thickness*width:
> I1:=width*(thickness^3)/12:
> alpha_prime:=(1/(E*I1)):
> beta_prime:=1/(E*A):
> beta_2_prime:=1/(G*A):
> mu:=((-beta_prime + k1*beta_2_prime + alpha_prime*r^2)/(beta_prime +
k1*beta_2_prime + alpha_prime*r^2)):
> phi1:=0:
> phi2:=120*Pi/180:
> phi3:=240*Pi/180:
> alpha:=1.2:
>N_0:=(phi1/(2*Pi))*R1*sin(phi1)+(phi2/(2*Pi))*R2*sin(phi2)+(phi3/(2*Pi))*R3*sin(p
hi3) -
(gamma1/(2*Pi))*F_R*sin(gamma1)+(phi1/(2*Pi))*T1*cos(phi1)+(phi2/(2*Pi))*T2*cos
(phi2) +(phi3/(2*Pi))*T3*cos(phi3)-(gamma1/(2*Pi))*F_T*cos(gamma1)-
(mu/(2*Pi))*T1*sin(phi1)-(mu/(2*Pi))*T2*sin(phi2)-
(mu/(2*Pi))*T3*sin(phi3)+(mu/(2*Pi))*F_T*sin(gamma1):
>Q_0:=(phi1/(2*Pi))*R1*cos(phi1)+(phi2/(2*Pi))*R2*cos(phi2)+(phi3/(2*Pi))*R3*cos(
phi3) -(gamma1/(2*Pi))*F_R*cos(gamma1)-(phi1/(2*Pi))*T1*sin(phi1)-
(phi2/(2*Pi))*T2*sin(phi2) -
(phi3/(2*Pi))*T3*sin(phi3)+(gamma1/(2*Pi))*F_T*sin(gamma1)-
(mu/(2*Pi))*T1*cos(phi1) -(mu/(2*Pi))*T2*cos(phi2)-
(mu/(2*Pi))*T3*cos(phi3)+(mu/(2*Pi))*F_T*cos(gamma1):
```

```
> M_0:=-r*N_0-(r/(2*Pi))*(R1+R2+R3-F_R)+(r/(2*Pi))*(phi1*T1+phi2*T2+phi3*T3-
gamma1*F_T):
> M_phi1:=M_0 + Q_0*r*sin(phi) + N_0*r*(1-cos(phi)) + R1*r*sin(phi-phi1) +
T1*r*(1-cos(phi-phi1)):
> M_phi2:=M_0 + Q_0*r*sin(phi) + N_0*r*(1-cos(phi)) + R1*r*sin(phi-phi1) +
R2*r*sin(phi-phi2)+ T1*r*(1-cos(phi-phi1))+T2*r*(1-cos(phi-phi2)):
> M_phi3:=M_0 + Q_0*r*sin(phi) + N_0*r*(1-cos(phi)) + R1*r*sin(phi-phi1) +
R2*r*sin(phi-phi2)   - F_R*r*sin(phi-gamma1) + T1*r*(1-cos(phi-phi1)) + T2*r*(1-
cos(phi-phi2)) - F_T*r*(1-cos(phi-gamma1)):
> M_phi4:=M_0 + Q_0*r*sin(phi) + N_0*r*(1-cos(phi)) + R1*r*sin(phi-phi1) +
R2*r*sin(phi-phi2) + R3*r*sin(phi-phi3) - F_R*r*sin(phi-gamma1) + T1*r*(1-cos(phi-
phi1)) + T2*r*(1-cos(phi-phi2)) + T3*r*(1-cos(phi-phi3)) - F_T*r*(1-cos(phi-gamma1)):
>Ubeam:=(int((M_phi1^2*r)/(2*E*I1),phi=phi1..phi2)+int((M_phi2^2*r)/(2*E*I1),phi=
phi2..gamma1)+int((M_phi3^2*r)/(2*E*I1),phi=gamma1..phi3)+int((M_phi4^2*r)/(2*E*
I1),phi=phi3..(2*Pi))):
> Eq1:=-F_R*cos(gamma1)+F_T*sin(gamma1)+R1*cos(phi1)-
T1*sin(phi1)+R2*cos(phi2)-T2*sin(phi2)+R3*cos(phi3)-T3*sin(phi3):
> Eq2:=-F_R*sin(gamma1)-
F_T*cos(gamma1)+R1*sin(phi1)+T1*cos(phi1)+R2*sin(phi2)+T2*cos(phi2)+R3*sin(ph
i3)+T3*cos(phi3):
> Eq3:=-r*F_T+r*(T1+T2+T3):
> s:=solve({Eq1,Eq2,Eq3},{T1,T2,T3}):
> assign(s):
> first:=diff(Ubeam,R1):
> second:=diff(Ubeam,R2):
> third:=diff(Ubeam,R3):
> final:=solve({first,second,third},{R1,R2,R3}):
> assign(final):
```

To obtain reaction force formula for θ = 240° to 360°

```
> E:=202016380100:
> G:=79289705500:
> rout:=0.0528/2:
> rin:=0.0462/2:
> r:=(rout+rin)/2:
> thickness:=rout-rin:
> width:=0.0254:
> k1:=1.2:
> A:=thickness*width:
> I1:=width*(thickness^3)/12:
> alpha_prime:=(1/(E*I1)):
> beta_prime:=1/(E*A):
> beta_2_prime:=1/(G*A):
```

```
> mu:=((-beta_prime + k1*beta_2_prime + alpha_prime*r^2)/(beta_prime +
k1*beta_2_prime + alpha_prime*r^2)):
> phi1:=0:
> phi2:=120*Pi/180:
> phi3:=240*Pi/180:
> alpha:=1.2:
>N_0:=(phi1/(2*Pi))*R1*sin(phi1)+(phi2/(2*Pi))*R2*sin(phi2)+(phi3/(2*Pi))*R3*sin(p
hi3) -
(gamma1/(2*Pi))*F_R*sin(gamma1)+(phi1/(2*Pi))*T1*cos(phi1)+(phi2/(2*Pi))*T2*cos
(phi2) +(phi3/(2*Pi))*T3*cos(phi3)-(gamma1/(2*Pi))*F_T*cos(gamma1)-
(mu/(2*Pi))*T1*sin(phi1)-(mu/(2*Pi))*T2*sin(phi2)-
(mu/(2*Pi))*T3*sin(phi3)+(mu/(2*Pi))*F_T*sin(gamma1):
>Q_0:=(phi1/(2*Pi))*R1*cos(phi1)+(phi2/(2*Pi))*R2*cos(phi2)+(phi3/(2*Pi))*R3*cos(
phi3) -(gamma1/(2*Pi))*F_R*cos(gamma1)-(phi1/(2*Pi))*T1*sin(phi1)-
(phi2/(2*Pi))*T2*sin(phi2) -
(phi3/(2*Pi))*T3*sin(phi3)+(gamma1/(2*Pi))*F_T*sin(gamma1)-
(mu/(2*Pi))*T1*cos(phi1) -(mu/(2*Pi))*T2*cos(phi2)-
(mu/(2*Pi))*T3*cos(phi3)+(mu/(2*Pi))*F_T*cos(gamma1):
> M_0:=-r*N_0-(r/(2*Pi))*(R1+R2+R3-F_R)+(r/(2*Pi))*(phi1*T1+phi2*T2+phi3*T3-
gamma1*F_T):
> M_phi1:=M_0 + Q_0*r*sin(phi) + N_0*r*(1-cos(phi)) + R1*r*sin(phi-phi1) +
T1*r*(1-cos(phi-phi1)):
> M_phi2:=M_0 + Q_0*r*sin(phi) + N_0*r*(1-cos(phi)) + R1*r*sin(phi-phi1) +
R2*r*sin(phi-phi2)+ T1*r*(1-cos(phi-phi1))+T2*r*(1-cos(phi-phi2)):
> M_phi3:=M_0 + Q_0*r*sin(phi) + N_0*r*(1-cos(phi)) + R1*r*sin(phi-phi1) +
R2*r*sin(phi-phi2) + R3*r*sin(phi-phi3) + T1*r*(1-cos(phi-phi1)) + T2*r*(1-cos(phi-
phi2)) + T3*r*(1-cos(phi-phi3)):
> M_phi4:=M_0 + Q_0*r*sin(phi) + N_0*r*(1-cos(phi)) + R1*r*sin(phi-phi1) +
R2*r*sin(phi-phi2) + R3*r*sin(phi-phi3) - F_R*r*sin(phi-gamma1) + T1*r*(1-cos(phi-
phi1)) + T2*r*(1-cos(phi-phi2)) + T3*r*(1-cos(phi-phi3)) - F_T*r*(1-cos(phi-gamma1)):
>
Ubeam:=(int((M_phi1^2*r)/(2*E*I1),phi=phi1..phi2)+int((M_phi2^2*r)/(2*E*I1),phi=p
hi2..phi3)+int((M_phi3^2*r)/(2*E*I1),phi=phi3..gamma1)+int((M_phi4^2*r)/(2*E*I1),p
hi=gamma1..(2*Pi))):
> Eq1:=-F_R*cos(gamma1)+F_T*sin(gamma1)+R1*cos(phi1)-
T1*sin(phi1)+R2*cos(phi2)-T2*sin(phi2)+R3*cos(phi3)-T3*sin(phi3):
> Eq2:=-F_R*sin(gamma1)-
F_T*cos(gamma1)+R1*sin(phi1)+T1*cos(phi1)+R2*sin(phi2)+T2*cos(phi2)+R3*sin(ph
i3)+T3*cos(phi3):
> Eq3:=-r*F_T+r*(T1+T2+T3):
> s:=solve({Eq1,Eq2,Eq3},{T1,T2,T3}):
> assign(s):
> first:=diff(Ubeam,R1):
> second:=diff(Ubeam,R2):
```

```
> third:=diff(Ubeam,R3):
> final:=solve({first,second,third},{R1,R2,R3}):
> assign(final):
```

APPENDIX C

Equipment Listing

6” Draw Bar Chuck
Manufacturer: Hardinge
Model Number: SCA 2000 306 –825H

Boring Bar
Manufacturer: Kennametal
Model Number: A16-DCLNR

Cutting Tool
Manufacturer: Kennametal
Model Number: CNMA-432 KC730

Grip force meter
Manufacturer: Pratt Burnerd
Model Number: 1009-06490

Machining Force Dynamometer
Manufacturer: Kistler
Model Number: 9257B

Medium Height Soft Jaws
Manufacturer: Hardinge
Model Number: SC 2000023-S

Precision CNC lathe
Manufacturer: Hardinge
Model Number: T-42 SP

Roundness Machine
Manufacturer: Taylor Hobson
Model Number: Talyrond 200

Roundness Software
Manufacturer: Metrex
Model Number: Profile View V 2.1.9

Scroll type chuck
Manufacturer: Bison
Model Number: 3215-10”-5

Tri-axial Load Cell
Manufacturer: Kistler
Model Number: 9251AQ

Three channel load cell signal conditioner
Manufacturer: Kistler
Model Number: 5010

Tool Holder
Manufacturer: Kennametal
Model Number: DCLNR-124-B

REFERENCES

1. Biezeno, C. B. and Grammel, R., Engineering Dynamics. Vol. II. Blackie and Son limited. London, 1956, pp. 105-222

2. Boresi, A. P. and Schmidt, R. J., Advanced Mechanics of Materials. 6th edition, John Wiley & Sons, New York, 2003, pp. 319-352.

3. Davis, T. L., Kahg, C. H., and Lord, H. W., "The Effect of Chucking Methods on Roundness Error in the Boring Process," *Journal of Engineering for Industry*, February 1976, pp. 233 – 238.

4. Fuh, J.Y.H., and Nee, A.Y.C., "Verification and Optimization of Workholding Schemes for Fixture Design", *Journal of Design and Manufacturing*, Vol.4, 1994, pp. 307-318.

5. Hurtado, J. F. and Melkote, S. N., "A Model for the Prediction of Reaction Forces in a 3-2-1 Machining Fixture," *Transaction of NAMRI/SME*, Vol. 26, pp. 353-340.

6. Ito, Y. and Rahman, M., "Machining Accuracy of a Cylindrical Workpiece Held by a Three Jaw Chuck," *Bull. Japan Soc. of Prec. Engg.*, Vol. 13. No. 1, 1979, pp. 7-12.

7. Matin, M. A. and Rahman, M., "Analysis of the Cutting Process of a Cylindrical Workpiece Clamped by a Three Jaw Chuck," *Transactions of the ASME*, Vol. 110. No. 110, 1988, pp. 326-332.

8. Nee, A.Y.C., Kumar, A.S., and Tao, Z.J., "An Intelligent Fixture with a Dynamic Clamping Scheme," *Proc. Instn. Mech. Engrs.*, Vol. 214. Part. B, 2000, pp. 183-196.

9. Nymekye, K. and Mudiam, S. S., "A Model for Predicting the Initial Static Gripping Force in Lathe Chucks", *International Journal of Advanced Manufacturing Technology.* Springer-Verlag Ltd. London., 1992, pp. 285-291.

10. Reason, R. E., "Report on the Measurement of Roundness – 1966", The Bank Organization, Leicester, England, 1966.

11. Sathyanarayana, S and Melkote, S. N., “Determination of Clamping Force Based on Minimization of Workpiece Elastic Deformation,” *Transaction of NAMRI/SME,* Vol. 3, 2002, pp. 597-604.

12. Sathyanarayana, S and Melkote, S. N., “Finite Element Modeling for Fixture-Workpiece Contacts: Single Contact Modeling and Experimental Verification,” International Journal of Machine Tools and Manufacture, Vol. 44, 2004, pp. 903-913.

13. Timoshenko S. P., Strength of Materials, D van Nostrand Company Inc, Part I, 1955, pp. 378-385

14. Walter, M. F. and Stahl, J. E., "Theories for Adaptive Control of Chucking Devices in NC-Turning Centers," *Proc. of the Information Technology for Advanced Manufacturing Systems*, 1992, pp. 249-256.

15. Walter, M. F. and Stahl, J. E., "The Connection Between Cutting and Clamping Forces in Turning," *International Journal of Machine Tools & Manufacture*, Vol. 34. No. 7, 1994, pp. 991-1003.

16. Wang, Y.F., Wong, Y.S., and Fuh, J.Y.H., ”Off-line Modeling and Planning of Optimal Clamping Forces for an Intelligent Fixturing System,” *International Journal of Machine Tools & Manufacture*, Vol. 39, 1999, pp. 253-271.